DISSERTATION

ION PROPERTIES FROM HIGH-*L* RYDBERG ATOM SPECTROSCOPY: APPLICATIONS TO NICKEL

Submitted by

Shannon L. Woods

Department of Physics

In partial fulfillment of the requirements

For the Degree of Doctor of Philosophy

Colorado State University

Fort Collins, Colorado

Fall 2012

Doctoral Committee:

Advisor: Stephen R. Lundeen

David A. Krueger
Martin P. Gelfand
Amber T. Krummel

ABSTRACT

ION PROPERTIES FROM HIGH-*L* RYDBERG ATOM SPECTROSCOPY:

APPLICATIONS TO NICKEL

An effective potential model describing high-*L* Rydberg states was systematically derived. The model assumes that the response of the core ion to the electric field of the Rydberg electron is at least approximately adiabatic; in other words, the excitation energies of the core ion are large compared to the typical energies of the Rydberg levels. The resulting model should describe a wide variety of high-*L* Rydberg systems. It can be used, in combination with experimental measurements of fine structure patterns, to extract measurements of core ion properties that control long-range interactions between the core and the Rydberg electron. These include permanent electric and magnetic moments, and electric polarizabilities. As an example application of the model, the fine structure pattern in n = 9 Rydberg levels of nickel was measured using the Microwave Resonant Excitation Stark Ionization Spectroscopy (RESIS) method. Properties of the $^2D_{5/2}$ ground state of Ni^+ extracted from these measurements include quadrupole and hexadecapole moments $Q = -0.4705(2)$ a.u. and $\Pi = 0.27(9)$ a.u., scalar and tensor dipole polarizabilities $\alpha_{D,0} = 7.925(10)$ a.u. and $\alpha_{D,2} = 1.043(33)$ a.u., and scalar quadrupole polarizability $\alpha_{Q,0} = 71(9)$ a.u. In addition, evidence for a permanent magnetic octupole moment of Ni^+ was seen, parameterized by the coefficient $C_{M3} = -0.346(57)$ a.u.

TABLE OF CONTENTS

Chapter 1: Introduction 1
1.1 Motivation 1
1.2 Theoretical Model 3
1.3 RESIS Technique 6
1.4 Past and Present 8
Chapter 2: Theoretical Model of High-L Rydberg States 9
2.1 Introduction 9
2.2 Derivation 13
2.2A Zeroth- and First-order Energies 15
2.2B Second-order Energy (Core Excited Intermediate States) 16
2.2C Rydberg Intermediate States 31
2.2D Spin and Relativistic Terms 37
2.3 Discussion 39
Chapter 3: RESIS Experimental Apparatus 47
3.1 Introduction 47
3.2 Ion Beam Creation and Selection 48
3.3 Rydberg State Formation 53
3.4 Initial Stripper 55
3.5 Optical RESIS Technique 56
3.6 Detection 61
3.7 Microwave RESIS Technique 61
Chapter 4: Measurement of the Nickel Rydberg Fine Structure 69
4.1 Introduction 69
4.2 Fitting and Correcting the Observed Transition Frequencies 69
4.3 Energy Level Corrections and Structure Parameters 86
4.4 Core Properties 95
4.5 Conclusions and Future Work 106
Chapter 5: Summary 108
References 109

Appendix A: Derivation of First and Second Nonadiabatic Terms 112
A.1 First Nonadiabatic Term 113
A.2 Second Nonadiabatic Term 115
Appendix B: Calculation of "f functions" for Theoretical Model 120
Appendix C: Observed Microwave RESIS Transitions 123

LIST OF TABLES

Table 4.1: Calculated spin splittings for $n = 9$ 72
Table 4.2: Measured Ni transitions 74
Table 4.3: Ni $n = 9$ Rydberg fine structure energy levels and corrections 87
Table 4.4: Second-order energies in V_{eff} 89
Table 4.5: Compares measured core properties values to those calculated using Ref. [40] 91
Table 4.6: K-dependence of the effective potential 93
Table 4.7: Fitted structure parameter values 94
Table 4.8: A_0 plot values 96
Table 4.9: A_2 plot values 99
Table 4.10: A_1 plot values 101
Table 4.11: A_3 plot values 103
Table 4.12: A_4 plot values 105
Table 4.13: Current results compared to previous measurements and theory 106

LIST OF FIGURES

Figure 1.1: Diagram of a "hydrogen-like" nickel atom 1
Figure 1.2: Scalar and tensor structures 5
Figure 1.3: Illustration of the RESIS technique 6
Figure 3.1: Experimental apparatus schematic 47
Figure 3.2: Picture of the RF ion source 48
Figure 3.3: Electrical connections of the source and $\vec{v}\times\vec{B}$ filter. 49
Figure 3.4: Scan of the magnet voltage (V_{mag}) versus beam current 51
Figure 3.5: Rb excitation scheme 54
Figure 3.6: Rb excitation optics schematic 54
Figure 3.7: Initial stripper 55
Figure 3.8: Simulated Ni optical spectrum 57
Figure 3.9: LIR angle diagram 58
Figure 3.10: A typical Ni optical scan in LIR I 60
Figure 3.11: RF region diagram 62
Figure 3.12: Scans of the Ni $9K_{4.5}$ to $20L_{5.5}$ transition in LIR I and II 63
Figure 3.13: Dip scan for the Ni $9K_{4.5}$ to $20L_{5.5}$ transition 64
Figure 3.14: Saturation curve for the Ar $10H_{4.5}$ to $10I_{5.5}$ transition 65
Figure 3.15: RF population diagram 66
Figure 3.16: Ni co- and counter-propagating transition example 67
Figure 4.1: Flow chart describing the analysis procedure 70
Figure 4.2: Diagram showing spin splitting 71
Figure 4.3: Ni microwave transition showing resolved spin splitting 73
Figure 4.4: Ni $9I_{3.5}$ to $9L_{5.5}$ AC Stark shift plot 84
Figure 4.5: Ni $9I_{7.5}$ to $9L_{9.5}$ AC Stark shift plot 85
Figure 4.6: Energy level diagram 86
Figure 4.7: Scalar A_0 plot 96
Figure 4.8: Tensor A_2 plot 99
Figure 4.9: Vector A_1 plot 101
Figure 4.10: Third-rank tensor A_3 plot 103
Figure 4.11: Fourth-rank A_4 plot 105
Figure C.1: Ni $9I_{4.5}$ to $9K_{5.5}$ co-propagating 123
Figure C.2: Ni $9I_{5.5}$ to $9K_{6.5}$ co-propagating 123
Figure C.3: Ni $9I_{5.5}$ to $9K_{5.5}$ counter-propagating 124
Figure C.4: Ni $9I_{6.5}$ to $9K_{7.5}$ co-propagating 124
Figure C.5: Ni $9I_{7.5}$ to $9K_{8.5}$ co-propagating 125
Figure C.6: Ni $9I_{7.5}$ to $9K_{7.5}$ counter-propagating 125
Figure C.7: Ni $9K_{4.5}$ to $9L_{5.5}$ co-propagating 126
Figure C.8: Ni $9K_{5.5}$ to $9L_{6.5}$ co-propagating 126

Figure C.9: Ni $9K_{5.5}$ to $9L_{5.5}$ co-propagating 127
Figure C.10: Ni $9K_{6.5}$ to $9L_{7.5}$ counter-propagating 127
Figure C.11: Ni $9K_{7.5}$ to $9L_{8.5}$ co-propagating 128
Figure C.12: Ni $9K_{7.5}$ to $9L_{7.5}$ counter-propagating 128
Figure C.13: Ni $9I_{3.5}$ to $9L_{5.5}$ co-propagating 129
Figure C.14: Ni $9I_{7.5}$ to $9L_{9.5}$ co-propagating 130

Chapter 1: Introduction

1.1 Motivation

A Rydberg state is a state of *any* atom or positive ion with a highly excited electron weakly attached to the positive ion core. For the study presented here, measurement of the nickel n = 9 Rydberg fine structure, the nickel ion looks almost like a proton as seen by the Rydberg electron. This is especially true if the Rydberg electron is a nonpenetrating high-L state. The system, a cartoon of which is shown in Fig. 1.1, looks almost like hydrogen.

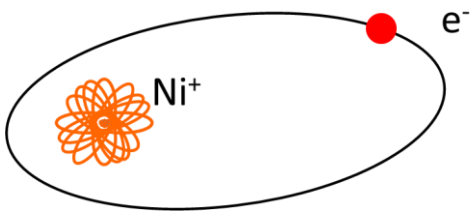

Figure 1.1: Diagram of a "hydrogen-like" nickel atom.

The energy levels of the Rydberg electron are in fact dominated by the Coulomb attraction between it and the ion core. However, since the nickel ion has properties that the proton does not, such as polarizabilities and permanent moments, there are long-range interactions between the Rydberg electron and core ion not present in hydrogen. Thus the energy levels are not exactly hydrogenic, so knowing their positions can lead to measurements of the ion core properties responsible for the additional long range interactions. Many of these properties are very difficult to measure for neutral atoms, and consequently the ion properties extracted from high-L Rydberg spectroscopy represent a unique probe of atomic structure theory. Such measurements provide valuable tests of calculations of positive ion wave functions, tests that can be difficult or impossible for neutral atoms.

In order to use the Rydberg electron as a probe of the core ion, it must have a high enough orbital angular momentum, L, that it can be distinguished from the core's electrons and does not penetrate the space of the core. The centrifugal barrier, $\frac{L(L+1)}{2r^2}$, stops the Rydberg electron from entering the space of the core electrons and determines the classical turning points of the Rydberg electron. The radial part of the Schrodinger equation for an electron orbiting a charge of $+Q$ is given by

$$\frac{d^2P_{nL}(r)}{dr^2}+\left[2E(n)+\frac{2Q}{r}-\frac{L(L+1)}{r^2}\right]P_{nL}(r)=0 \quad \text{(atomic units)}, \tag{1.1}$$

where $P_{nL}(r)=rR_{nL}(r)$ and $E(n)=-\frac{1}{2}\frac{Q^2}{n^2}$. Setting the bracketed portion, which represents the kinetic energy of the electron, equal to zero and solving for r gives the classical turning points

$$r=\frac{n^2}{Q}\left(1\pm\sqrt{1-\frac{L(L+1)}{n^2}}\right), \tag{1.2}$$

where the Bohr radius $a_0=0.0529\ \text{nm}$ is the unit length of atomic units (a.u.). The inner classical turning point is greater than

$$r_{ITP}\geq\frac{L(L+1)}{2Q} \tag{1.3}$$

and equal to this in the limit of $L^2<<n^2$. Thus a Rydberg electron is considered nonpenetrating if r_{ITP} is much larger than the core ion's radius. Typically this requires $L\geq 5$ for neutral Rydberg atoms.

This chapter introduces the basic idea behind the theory describing the interaction between a Rydberg electron and an ion core. It also gives a brief description of Resonant Excitation Stark Ionization Spectroscopy (RESIS), the technique used here to measure Rydberg

fine structure patterns. Chapter 2 derives the effective potential model for high-*L* Rydberg atoms, which provides a rigorous framework for extracting positive ion properties from high-*L* Rydberg fine structure measurements. Chapter 3 explains the experimental setup used for the RESIS technique, which makes precise measurements of high-*L* Rydberg fine structures possible. Chapter 4 presents RESIS measurements for the specific case of nickel and applies the effective potential to extract properties of Ni^+. Chapter 5 provides a summary.

In general, the motivation behind making these measurements of core properties is to provide a check on developing atomic theory [1]. Energy levels, unfortunately, are not very sensitive to theoretical wave functions. Lifetimes and transition strengths are useful for testing theoretical calculations, but are difficult to measure precisely. Thus the method presented here for measuring and modeling high-*L* Rydberg energy levels is incredibly useful because of the precise core properties that can be extracted.

1.2 Theoretical Model

The theory of high-*L* Rydberg systems begins with a Hamiltonian which consists of the zeroth-order Hamiltonian of a free ion, the zeroth-order Hamiltonian of the hydrogenic Rydberg electron orbiting a positive ion core, and the potential representing the interaction between them. The spin of the Rydberg electron plays a nearly negligible role in the binding energy of the Rydberg system. To a good approximation the energy eigenstates are characterized by the vector sum of J_c, the total angular momentum of the core ion, and *L*, the orbital angular momentum of the Rydberg electron. This implies that there are $2J_c + 1$ energies possible for each value of *L*.

The potential is written as a multipole expansion and perturbation theory is applied to calculate the energy of the core plus electron system. It is assumed that the core excitation energies are much larger than the Rydberg energy, thus allowing the energy denominators that

occur in second-order perturbation theory to be expanded as a series of terms. In the end the perturbation energy is written as the expectation value of an effective potential consisting of a sum of increasing negative powers of the Rydberg electron's radial coordinate whose coefficients depend on the matrix elements and energies of the free ion:

$$\begin{aligned} E &\cong \left\langle V_{eff} \right\rangle \\ &= A_0 + A_1\left(\vec{L}\cdot\vec{J}_c\right) + A_2\left(\frac{\left\langle X^{[2]}\left(J_c\right)\cdot C^{[2]}\left(\hat{r}_{Ryd}\right)\right\rangle}{\begin{pmatrix} J_c & 2 & J_c \\ -J_c & 0 & J_c \end{pmatrix}}\right) + A_3\left(\left\langle X^{[3]}\left(J_c\right)\cdot T^{[3]}\left(\hat{r}_{Ryd}\right)\right\rangle\right) + A_4\left(\frac{\left\langle X^{[4]}\left(J_c\right)\cdot C^{[4]}\left(\hat{r}_{Ryd}\right)\right\rangle}{\begin{pmatrix} J_c & 4 & J_c \\ -J_c & 0 & J_c \end{pmatrix}}\right), \end{aligned} \tag{1.4}$$

where the structure parameters are defined as

$$\begin{aligned} A_0 &= -\frac{1}{2}\alpha_{D,0}\left\langle r^{-4}\right\rangle_{nL} - \frac{1}{2}\left(\alpha_{Q,0} - 6\beta_{D,0}\right)\left\langle r^{-6}\right\rangle_{nL} \\ &\quad + \frac{8Q}{5}\gamma_{D,0}\left\langle r^{-7}\right\rangle_{nL} - \frac{1}{2}\left(\alpha_{O,0} - 6\beta_{Q,0} + 72\gamma_{D,0}\left(1 + \frac{L\left(L+1\right)}{10}\right)\right)\left\langle r^{-8}\right\rangle_{nL} + \cdots \\ A_1 &= -\frac{1}{2}g_J\alpha_{FS}^2\left\langle r^{-3}\right\rangle_{nL} + \beta_{D,1}\left\langle r^{-6}\right\rangle_{nL} + \left(\beta_{Q,1} + \gamma_{D,1}\right)\left\langle r^{-8}\right\rangle_{nL} + \cdots \\ A_2 &= -Q\left\langle r^{-3}\right\rangle_{nL} - \frac{1}{2}\alpha_{D,2}\left\langle r^{-4}\right\rangle_{nL} - \frac{1}{2}\left(\alpha_{Q,2} - 6\beta_{D,2} + \alpha_{DO,2}\right)\left\langle r^{-6}\right\rangle_{nL} \\ &\quad + \frac{8Q}{5}\gamma_{D,2}\left\langle r^{-7}\right\rangle_{nL} - \frac{1}{2}\left(\alpha_{O,2} - 6\beta_{Q,2} + \alpha_{QH,2} - 6\beta_{DO,2} + 72\left(\frac{1}{4} + \frac{L\left(L+1\right)}{10}\right)\gamma_{D,2}\right)\left\langle r^{-8}\right\rangle_{nL} + \cdots \\ A_3 &= C_{\mathrm{M3}}\left\langle r^{-5}\right\rangle_{nL} + \left(\beta_{Q,3} + \beta_{DO,3}\right)\left\langle r^{-8}\right\rangle_{nL} + \cdots \\ A_4 &= -\Pi\left\langle r^{-5}\right\rangle_{nL} - \frac{1}{2}\left(\alpha_{Q,4} + \alpha_{DO,4}\right)\left\langle r^{-6}\right\rangle_{nL} - \frac{1}{2}\left(\alpha_{O,4} - 6\beta_{Q,4} + \alpha_{QH,4} - 6\beta_{DO,4}\right)\left\langle r^{-8}\right\rangle_{nL} + \cdots \end{aligned} \tag{1.5}$$

Although there is a lot of information contained within this set of equations, overall there are only a few main points to get from it.

The first is that the energy has been broken into different tensor orders which consist of scalar products of tensor operators. Each of these products may be simply calculated using

known formulas, noting that the possible tensor orders are restricted by J_c and L. The usefulness of breaking the energy into tensor orders can be understood by looking at the dominant structure orders: scalar and tensor. The scalar structure, shown on the left of Fig. 1.2, simply shifts the energy down from the hydrogenic energy level. The tensor structure, however, splits the energies into multiple levels. Shown in Fig. 1.2, on the right, is the tensor structure for a core ion with J_c = 5/2 and thus six energy levels for a given n and L.

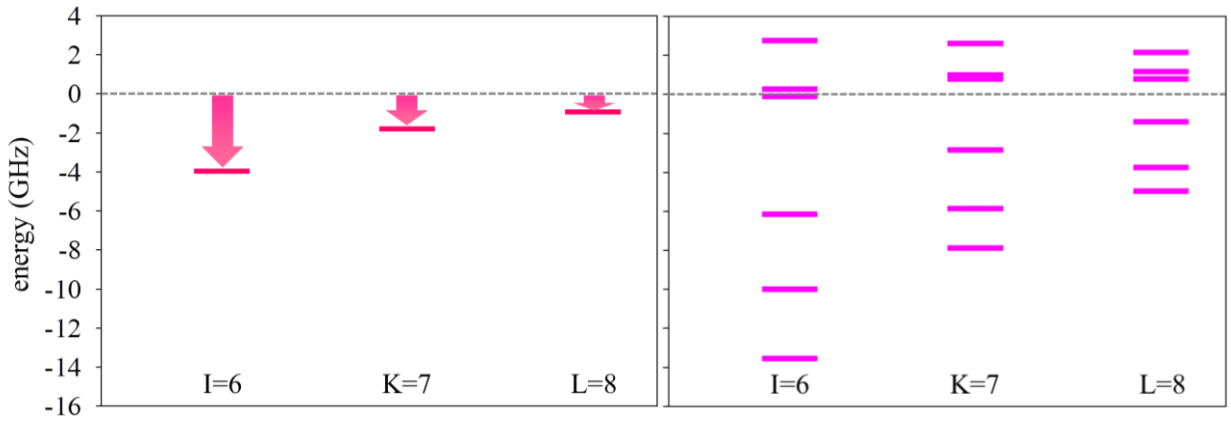

Figure 1.2: Scalar and tensor structures (left and right, respectively) where the n = 9 hydrogenic energy, shown by the dashed line, has been taken as the zero point. For comparison, the n = 10 hydrogenic energy level is nearly 8000 GHz away. Both plots show L = 6, 7, and 8 (also labeled using spectroscopic notation). The values used to produce these plots are for the particular case of nickel.

Another point is that the core and Rydberg electron dependence has been separated within the structure parameters. The Rydberg dependence has been written as the expectation value of the Rydberg radial coordinate. Since the Rydberg electron's zeroth-order wave functions are hydrogenic, these expressions have well-known formulas and are simple to calculate [2]. Additionally, it should be emphasized that the core properties contain all of the dependence of the potentially very complex core wave functions. Many of these coefficients can be identified with well-defined properties of the core. Thus the theory of high-L Rydberg

systems can be applied to measurements of Rydberg fine structure patterns in order to extract properties of the ion core.

1.3 RESIS Technique

The RESIS technique is a unique form of spectroscopy in which high-L Rydberg states in a fast Rydberg beam are resonantly excited by a Doppler-tuned CO_2 laser, resolving the fine structure pattern of the high-L levels. It is unique in that it allows access to high-L Rydberg states that are not otherwise visible using traditional spectroscopy techniques. Absorption spectroscopy from the ground state of atoms is limited by the selection rule $\Delta L = \pm 1$ (dipole excitation). Since atoms tend to have ground states with low orbital angular momentum, the excited states reached by absorption spectroscopy will also have low L. The emission spectra of $L < 3$ excited states dominate the emission spectra of atoms and ions since they are most easily measured. The emission of high-L excited states occurs, but at a much lower rate and typically in the infrared where it would require high-resolution spectrometers in order to resolve non-hydrogenic features. The RESIS method, on the other hand, relies on the upward excitation of Rydberg atoms or ions which means that all Ls are accessible. Figure 1.3 illustrates the basic idea of the RESIS technique (a schematic of the apparatus is shown in Fig. 3.1).

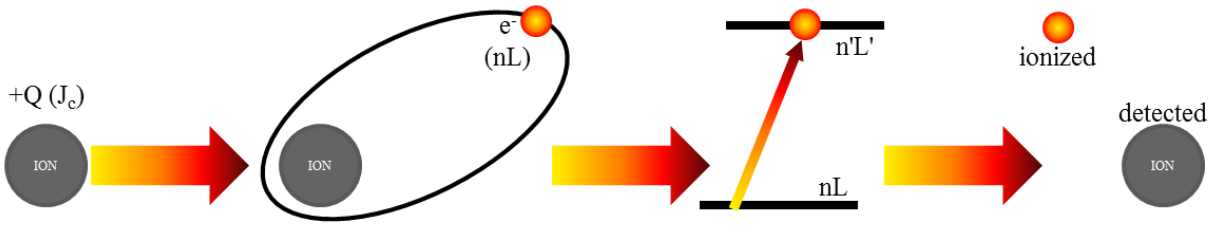

Figure 1.3: Illustration of the RESIS technique where a positive ion (J_c) of charge Q captures a high-L Rydberg electron (nL). The electron is excited to some upper state by a Doppler-tuned CO_2 laser before being Stark ionized and the resulting ion detected. States of all possible L values are formed in the capture process and can be excited upwards by the laser.

The optical RESIS technique typically provides the initial mapping of the pattern while the microwave RESIS technique gives more precise measurements. Both begin with an ion beam accelerated to a high velocity, $\frac{v}{c} \approx 0.001$. A small percentage of the ion beam charge captures a highly excited electron from a Rydberg target. The Rydberg target is created from a thermal beam of Rb which is step-wise excited to the 9*F* state using three diode lasers. The beam then enters the region of the initial stripper where it encounters an electric field strong enough to ionize any electrons with $n > 15$ and deflect any remaining ions. The beam then enters the first laser interaction region (LIR) where it intersects a Doppler-tuned CO_2 laser beam which excites the Rydberg electrons from a low *n* to a previously depleted upper *n'*. The final stripper would then be set to Stark ionize states with that particular *n'*. In other words, an external field greater than that which binds the Rydberg electron to the core is applied, resulting in the ionization of the Rydberg electron [3]. The detector then measures the current synchronous with the chopping of the CO_2 laser. This current is measured as a function of the Doppler-tuned CO_2 laser frequency to reveal the optical RESIS spectrum and the high-*L* binding energies.

With the microwave RESIS technique, transitions between Rydberg levels of the same *n* are induced by microwave electric fields and detected by taking advantage of the RESIS excitation's resolution of the fine structure pattern. Two LIRs are used, both tuned to excite the same Rydberg level. The first LIR depletes the population of that level. A microwave interaction region, between the two LIRs, may replenish that level's population if it is in resonance with a transition to a different fine structure level (same *n*). If this occurs, the second LIR will excite more atoms to the upper state of the optical RESIS transition, increasing the detected Stark ionization current. The detector is set to measure the current synchronous with

the chopping of the microwave field, and this is measured as a function of the microwave frequency to reveal the resonance.

1.4 Past and Present

The theoretical framework for high-*L* Rydberg atoms with a J_c = 0 core has been studied for years. Such a system is described by a scalar potential with leading terms inversely proportional to the fourth and sixth powers of the Rydberg electron's radial coordinate:

$$V_{J_c=0} \sim -\frac{1}{2}\frac{\alpha_D}{r^4} - \frac{1}{2}\left(\frac{\alpha_Q - 6\beta_D}{r^6}\right) + \cdots . \tag{1.6}$$

(a brief history is presented in Section 2.1). Note that this potential neglects all magnetic interactions, so they must be included separately (Section 2.2D). Early experiments with J_c = 3/2, such as Ne^+ [4] and Ar^+ [5], lacked a rigorous derivation of the theoretical framework needed to describe the more complicated Rydberg fine structures of these atoms. The experimental study presented here of Ni^+, chosen because it has a J_c equal to 5/2, represents the most complicated high-*L* Rydberg atom studied to date. In addition to the vector and tensor terms mentioned in the Ne^+ and Ar^+ studies, the higher J_c of the nickel ion indicates the possibility of higher-order tensor terms not previously considered. It also highlights the need for a systematic derivation of the theory describing not just high-*L* Rydberg states of nickel, but generalized to any J_c and any charge for the positive ion. The theory derived in Chapter 2 lays a solid framework for a wide range of possible studies. Additionally, the study of Ni^+ opens up the possibility of future experiments on ions with J_c = 5/2.

Chapter 2: Theoretical Model of High-L Rydberg States

2.1 Introduction

The wave functions and energies of a single Rydberg electron bound to an atomic ion approach purely hydrogenic values as the angular momentum of the Rydberg electron increases. Since the inner classical turning point of the Rydberg electron's radial motion is greater than

$$r_{ITP} \geq \frac{L(L+1)}{2Q}, \tag{2.1}$$

where L is its angular momentum and Q is the net charge of the core ion, Rydberg electrons of sufficiently high L are effectively confined outside of the region of space occupied by the ion core. Their interactions with the ion core are dominated by the fully screened Coulomb attraction that binds them in their orbit. Any additional interactions are weak and long-ranged. In the absence of these additional interactions, all high-L Rydberg levels of the same principal quantum number would be degenerate except for small relativistic effects. The presence of the weak long-range interactions lifts this degeneracy and produces a pattern of binding energies that reflects the strength and character of these interactions. Measurement of these "fine structure patterns" is therefore a convenient probe of the core properties that control the strength of the long-range interactions, such as polarizabilities and permanent electric moments.

The complexity of these fine structure patterns depends directly on the angular momentum of the core ion, J_c. These patterns represent an example of "pair-coupling" where the spin splitting of the Rydberg electron is nearly negligible and the intermediate angular momentum,

$$\vec{K} = \vec{J}_c + \vec{L}, \tag{2.2}$$

describes the eigenstates [6]. In general there are $2J_c + 1$ energies possible for each value of the Rydberg electron's orbital angular momentum, *L*. Consequently, in what follows, *K* will be considered to be the total angular momentum of the Rydberg system and the small effect of the Rydberg electron's spin will be treated separately.

The basic idea of using the spectroscopy of nonpenetrating Rydberg levels to extract information about the properties of the ion core was discussed very early by Mayer and Mayer in 1933 [7]. In the case of Rydberg atoms or ions with *S*-state cores, the deviation of the term energies from their hydrogenic values was related to the dipole and quadrupole polarizabilities of the ion with a model considering the electric field and field gradient produced by a stationary Rydberg electron. This led to a simple expression for the energy change in terms of the expectation value of an effective potential:

$$\Delta E_{J_c=0} = \left\langle -\frac{1}{2}\frac{\alpha_D}{r^4} - \frac{1}{2}\frac{\alpha_Q}{r^6} \right\rangle_{nL} . \tag{2.3}$$

The two basic assumptions underlying this approach are common to all treatments of high-*L* Rydberg structure, including this work:

A1. The Rydberg electron is distinguishable from the electrons in the ion core.

A2. The Rydberg electron is always farther from the nucleus than any of the core electrons.

In He^+ the assumption that the Rydberg electron is distinguishable appears to be valid for H states (L = 5) or higher [8]. For other ions the size of this effect is not clear. In addition to these assumptions, this early approximation neglects the dynamics of the Rydberg electron, effectively assuming that the core adjusts adiabatically to the motion of the Rydberg electron. A number of approaches were later advanced to incorporate corrections to this adiabatic

model [9, 10, 11]. If the corrections to the adiabatic picture are small, Kleinman, Hahn, and Spruch showed that adding a term proportional to r^{-6} to the potential could account approximately for the nonadiabatic effects [11]:

$$\alpha_Q \Rightarrow \left(\alpha_Q - 6\beta_D\right), \tag{2.4}$$

where β_D was an additional core property often referred to as the "nonadiabatic dipole polarizability".

A major step in the further development of the effective potential model for high-*L* Rydberg structure was the treatment of Rydberg levels of helium by Drachman [12, 13, 14]. In a sequence of papers, he systematically derived an effective potential for helium Rydberg electrons that contained additional terms proportional to higher inverse powers of the Rydberg radial coordinate up to r^{-10}. The dynamics of the Rydberg electron were found to lead to significant deviations from the adiabatic model, and these were systematically included. Since the core ion in this case was He^+, whose nonrelativistic wave functions were known, all the coefficients occurring in the effective potential were calculated analytically. Although Drachman used the Feshbach projection operator technique to organize his calculation, in essence it consisted of systematically applying three expansions:

I. Static perturbation theory.

II. Multipole expansion of the perturbing term.

III. A power series expansion of the energy denominators occurring in I, described fully below, which is referred to as the "adiabatic expansion" because the leading term corresponds to the adiabatic model.

Because the zeroth-order wave functions of the Rydberg electron satisfy the hydrogenic radial equation, it was possible to manipulate the resulting expressions into a form where successive

terms were proportional to increasing negative powers of *r*, yielding the effective potential. The expectation value of each term could be evaluated using standard expressions for the radial expectation values of hydrogenic functions. In the case of helium Rydberg levels, the results of this approach were confirmed with completely independent variational calculations [15] and with precise experimental measurements [16, 17]. The precision of the predictions obtained with the effective potential method is limited by the convergence of the asymptotic series of terms, but this approach has the great advantage that it can be applied to any Rydberg level, (nL), without the necessity of a specific calculation for that state's wave function. The variational method is much more computationally intensive.

The calculation presented here is modeled after the work of Drachman. Its key feature is use of the adiabatic expansion and manipulation of the perturbation expressions using the hydrogenic radial equation satisfied by the zeroth-order Rydberg electron wave function. However, the present calculation extends the work of Drachman in two significant ways. First, the core properties that occur in the effective potential are expressed as functions of the matrix elements and energies of the core ion instead of being evaluated analytically as was possible for the He^+ core. Second, the angular momentum of the core ion, J_c, is not restricted. This gives rise to higher rank tensor operators not present in the helium case. Taken together, these extensions make the results applicable to a wide range of Rydberg systems. Some of the terms derived here are well known, such as the terms in Eq. 2.3 and the related tensor polarization terms. Others are new. Many of the higher-order terms occur in a related treatment of Rydberg electrons bound to anisotropic core ions, treated in a coupled-channel approach by Clark, Greene, and Miecznik [18]. The approach presented here differs from that calculation in several ways. The main difference is that this report, based on a perturbation expansion, calculates only

the differences from the known zeroth-order Rydberg energies. In contrast, the approach of Clark, Greene, and Miecznik depends on a specific calculation of the radial function and full energy eigenvalue for each level in the appropriate channel potential. Another difference between the calculations is in the method of including corrections to the adiabatic approximation. The effective potential model presented here has the advantage that it is easily applied to describe a wide range of high-*L* Rydberg systems without the need for extensive calculations.

2.2 Derivation

For simplicity, a completely nonrelativistic system of *N* electrons, bound to a nucleus of charge *Z*, is initially assumed. Using assumption A1 above, the N^{th} electron is taken to be the distinguishable Rydberg electron, and the Hamiltonian is written in a form that makes that distinction. The zeroth-order Hamiltonian is the sum of a Hamiltonian describing the free ion and a Hamiltonian describing a hydrogenic Rydberg electron bound by the net charge of the core ion. Everything left over from the full nonrelativistic Hamiltonian represents the perturbation *V*:

$$H = \left(H^0_{core} + H^0_{Ryd} \right) + V , \tag{2.5}$$

where

$$H^0_{core} = \sum_{i=1}^{N-1} \left(\frac{\left| \vec{p}_i \right|^2}{2} - \frac{Z}{r_i} \right) + \sum_{\substack{i=1 \\ j>i}}^{N-1} \frac{1}{r_{ij}} , \tag{2.6}$$

$$H^0_{Ryd} = \frac{\left| \vec{p}_N \right|^2}{2} - \frac{Q}{r_N} , \tag{2.7}$$

and

$$V = \sum_{i=1}^{N-1} \frac{1}{r_{iN}} - \frac{(N-1)}{r_N} , \tag{2.8}$$

and where Z is the nuclear charge, $Q = Z - N + 1$ is the charge of the ion core, and $N - 1$ is the number of electrons within the ion core. The further assumption A2 allows the potential to be written as a multipole expansion with no scalar (i.e. $\kappa = 0$) term:

$$V = \sum_{\kappa=1}^{\infty} \sum_{i=1}^{N-1} r_i^{\kappa} C^{[\kappa]}(\hat{r}_i) \cdot \frac{C^{[\kappa]}(\hat{r}_N)}{r_N^{\kappa+1}} = \sum_{\kappa=1}^{\infty} M^{[\kappa]} \cdot \frac{C^{[\kappa]}(\hat{r}_N)}{r_N^{\kappa+1}}, \tag{2.9}$$

where

$$M^{[\kappa]} = \sum_{i=1}^{N-1} r_i^{\kappa} C^{[\kappa]}(\hat{r}_i). \tag{2.10}$$

The operators $M^{[\kappa]}$ with $\kappa = 1, 2, 3, 4$ represent the dipole, quadrupole, octupole, and hexadecapole moment operators acting on the core ion wave function, while $C^{[\kappa]}$ represents a spherical κ^{th}-rank tensor either in the space of the core $(\hat{r}_i)$ or Rydberg electron $(\hat{r}_N)$. The potential is thus the scalar product of tensor orders (see Eq. 5.2.4 of Ref. [19]). The subscript on r_N may now be dropped since the core electrons' positions are not explicitly mentioned again.

The zeroth-order wave functions are products of the form

$$\left|\Psi^0\right\rangle = \left|\Psi^0_{core}\right\rangle \left|\Psi^0_{Ryd}\right\rangle,$$

where $\left|\Psi^0_{core}\right\rangle$ is the wave function of the free ion core and $\left|\Psi^0_{Ryd}\right\rangle$ is the hydrogenic wave function of the Rydberg electron. The core functions are assumed to be eigenstates of parity, angular momentum, and H^0_{core}. They are denoted by $\left|\lambda, J_c, m_J\right\rangle$, where λ stands for any additional quantum numbers required to specify a particular state. These functions, of course, are known only in the abstract. The Rydberg functions are specified by $\left|n, L, m\right\rangle$ and are the well-known hydrogenic wave functions corresponding to a core charge of Q and a reduced mass $\mu = m_e m_c / (m_e + m_c)$. Ignoring the spin of the electron, these wave functions couple together to

form the angular momentum *K*:

$$\vec{K} = \vec{L} + \vec{J}_c ,$$

where *K* ranges in integer steps from $\left|\vec{L} - \vec{J}_c\right|$ to $\left|\vec{L} + \vec{J}_c\right|$. In general, an arbitrary state of the combined system is denoted as $\left|\lambda' J_c', nL; K\right\rangle$. The goal is to describe the energies of Rydberg levels that correspond in zeroth-order to states in which the core is in its ground state, denoted as $\left|gJ_c\right\rangle$, the Rydberg electron is in the $\left(nL\right)$ level, and the total angular momentum, exclusive of Rydberg spin, is *K*. These levels are denoted as $\left|gJ_c, nL; K\right\rangle$ or by the shorthand notation $\left|nL_K\right\rangle$.

2.2A Zeroth- and First-order Energies

Applying static perturbation theory, the energy of the nL_K state is given by

$$E\left(nL_K\right) = E^{[0]} + E^{[1]} + E^{[2]} + \cdots . \tag{2.11}$$

The zeroth-order energy is the sum of that of a free ion and a hydrogenic electron:

$$E^{[0]}\left(n\right) = E\left(gJ_c\right) - \frac{1}{2}\frac{m_c}{\left(m_c + m_e\right)}\frac{Q^2}{n^2} , \tag{2.12}$$

where m_c is the core mass and m_e is the electron mass. Note that atomic units are used throughout this chapter.

The first-order energy perturbation energies come from the permanent electric moments of the core ion. There are no odd permanent moments because of parity constraints. An ion core with angular momentum of $J_c \geq 1$, however, may have a quadrupole moment, while a nonzero hexadecapole moment is possible if $J_c \geq 2$. Using the methods of Ref. [19] (including Eqs. 7.1.6 and 5.4.1) the first-order energy may be evaluated and written in terms of the permanent moments:

$$E^{[1]}\left(nL_K\right)=\left\langle gJ_c,nL;K\left|\sum_{\kappa=1}^{\infty}M^{[\kappa]}\cdot\frac{C^{[\kappa]}\left(\hat{r}\right)}{r^{\kappa+1}}\right|gJ_c,nL;K\right\rangle$$
$$=-Q\left\langle r^{-3}\right\rangle_{nL}\frac{\left\langle X^{[2]}\left(J_c\right)\cdot C^{[2]}\left(\hat{r}\right)\right\rangle}{\begin{pmatrix}J_c & 2 & J_c\\ -J_c & 0 & J_c\end{pmatrix}}-\Pi\left\langle r^{-5}\right\rangle_{nL}\frac{\left\langle X^{[4]}\left(J_c\right)\cdot C^{[4]}\left(\hat{r}\right)\right\rangle}{\begin{pmatrix}J_c & 4 & J_c\\ -J_c & 0 & J_c\end{pmatrix}}+\cdots, \quad (2.13)$$

where

$$Q\equiv-\left\langle gJ_c,m_J=J_c\left|M_0^{[2]}\right|gJ_c,m_J=J_c\right\rangle \quad (2.14)$$

is the core's electric quadrupole moment, and

$$\Pi\equiv-\left\langle gJ_c,m_J=J_c\left|M_0^{[4]}\right|gJ_c,m_J=J_c\right\rangle \quad (2.15)$$

is the core's electric hexadecapole moment. $X^{[b]}\left(J_c\right)$ is a unit b^{th}-rank tensor in the space of the ion core while $C^{[b]}\left(\hat{r}\right)$ is a spherical b^{th}-rank tensor in the Rydberg electron's angular position. The parentheses $\begin{pmatrix}\ \end{pmatrix}$ in the denominator represent 3J-symbols [19]. The expectation values of the Rydberg radial coordinate are represented by $\left\langle r^{-s}\right\rangle_{nL}$ [2]. The next possible permanent moment, of order κ = 6, requires $J_c \geq 3$.

2.2B Second-order Energy (Core Excited Intermediate States)

Equation 2.16 shows the general expression for the second-order energies:

$$E^{[2]}\left(nL_K\right)=$$
$$\sum_{\lambda',J_c',n',L'}\frac{\left\langle gJ_c,nL;K\left|\sum_{\kappa_1=1}^{\infty}M^{[\kappa_1]}\cdot\frac{C^{[\kappa_1]}\left(\hat{r}\right)}{r^{\kappa_1+1}}\right|\lambda'J_c',n'L';K\right\rangle\left\langle\lambda'J_c',n'L';K\left|\sum_{\kappa_2=1}^{\infty}M^{[\kappa_2]}\cdot\frac{C^{[\kappa_2]}\left(\hat{r}\right)}{r^{\kappa_2+1}}\right|gJ_c,nL;K\right\rangle}{\left[E\left(gJ_c\right)+E\left(n\right)\right]-\left[E\left(\lambda'J_c'\right)+E\left(n'\right)\right]}. \quad (2.16)$$

Initially only the portion of the total second-order energy that is due to intermediate states where the core is electronically excited is considered. This excludes intermediate states where the core is in its ground electronic state, either the true ground state or an excited fine structure level of the ground electronic state. The total second-order energy is the sum of terms consisting of the various multipole orders occurring in the potential *V*,

$$E^{[2]}\left(nL_K\right)=\sum_{\kappa_1,\kappa_2}E^{[2]}\left(\kappa_1,\kappa_2\right).$$

Using the methods of Ref. [19], the core and Rydberg electron parts of the matrix elements may be factored and the partial contribution due to specific multipole terms κ_1 and κ_2 written as

$$E^{[2]}\left(\kappa_1,\kappa_2\right)= -\sum_{\lambda',J_c',n',L'}\left[\frac{\left(-1\right)^{J_c'-J_c}\begin{Bmatrix}K & L & J_c\\ \kappa_1 & J_c' & L'\end{Bmatrix}\begin{Bmatrix}K & L' & J_c'\\ \kappa_2 & J_c & L\end{Bmatrix}\begin{pmatrix}L & \kappa_1 & L'\\ 0 & 0 & 0\end{pmatrix}\begin{pmatrix}L' & \kappa_2 & L\\ 0 & 0 & 0\end{pmatrix}\left(2L+1\right)\left(2L'+1\right)}{\Delta E\left(\lambda' J_c'\right)+E\left(n'\right)-E\left(n\right)}\right.$$
$$\left.\times\left\langle gJ_c\left\|M^{[\kappa_1]}\right\|\lambda' J_c'\right\rangle\left\langle\lambda' J_c'\left\|M^{[\kappa_2]}\right\|gJ_c\right\rangle\left\langle nL\left|r^{-(\kappa_1+1)}\right|n'L'\right\rangle\left\langle n'L'\left|r^{-(\kappa_2+1)}\right|nL\right\rangle\right], \tag{2.17}$$

where

$$\Delta E\left(\lambda' J_c'\right)=E\left(\lambda' J_c'\right)-E\left(gJ_c\right).$$

The curly brackets $\{\ \}$ represent 6J-symbols while the parentheses $(\ )$ represent 3J-symbols, both associated with the coupling of angular momenta [19]. The terms involving angle brackets $\langle\ \rangle$ and the core operators $M^{[\kappa]}$ represent reduced matrix elements of those tensor operators. The terms involving angle brackets and the Rydberg radial coordinate $r^{-(\kappa+1)}$ represent radial integrals. Note that, following from the triangle relations [6], only multipole terms with $\kappa_1+\kappa_2$ even can contribute to $E^{[2]}$.

Further simplification of this expression relies upon the "adiabatic expansion". This expansion is based on the assumption that the energy difference in the denominator is primarily due to the core energy difference, allowing the denominator to be expanded as

$$\frac{1}{\Delta E\left(\lambda' J_c'\right)+E\left(n'\right)-E\left(n\right)}=\frac{1}{\Delta E\left(\lambda' J_c'\right)}-\frac{\left(E\left(n'\right)-E\left(n\right)\right)}{\left(\Delta E\left(\lambda' J_c'\right)\right)^2}+\frac{\left(E\left(n'\right)-E\left(n\right)\right)^2}{\left(\Delta E\left(\lambda' J_c'\right)\right)^3}+\cdots. \quad (2.18)$$

If it is valid, the adiabatic expansion allows the sums over n' to be carried out explicitly using the properties of hydrogenic radial functions. The leading term, for instance, corresponds to the adiabatic approximation where the dynamics of the Rydberg electron are neglected. When this is substituted into Eq. 2.17, the only dependence on n' is in the radial matrix elements and the completeness of the radial functions for fixed L' allows the summation over n' to be carried out:

$$\sum_{n'}\left\langle nL\left|r^{-s}\right|n'L'\right\rangle\left\langle n'L'\left|r^{-q}\right|nL\right\rangle=\left\langle r^{-(s+q)}\right\rangle_{nL}. \quad (2.19)$$

Note that in this and similar sums, the sum over n' includes continuum levels of the same L'. This leads to expressions, described below, for all the adiabatic terms in the effective potential.

The second term in the adiabatic expansion also leads to expressions that can be simplified using properties of the Rydberg radial functions. Making use of the radial wave equation satisfied by hydrogenic functions, and using repeated application of integration by parts, it can be shown that

$$\sum_{n'}\left(E\left(n'\right)-E\left(n\right)\right)\left\langle nL\left|r^{-s}\right|n'L'\right\rangle\left\langle n'L'\left|r^{-q}\right|nL\right\rangle=\frac{1}{2}\left[sq-L\left(L+1\right)+L'\left(L'+1\right)\right]\left\langle r^{-(s+q+2)}\right\rangle_{nL}. \quad (2.20)$$

The details of this derivation are shown in Appendix A. This leads to a sequence of terms, detailed below, referred to as the 1st nonadiabatic terms.

The expressions obtained by substituting the third term of the adiabatic expansion into Eq. 2.17 can also be simplified. Using the radial equation satisfied by the Rydberg radial functions, it can be shown that

$$\begin{aligned}
&\sum_{n'}\left(E(n')-E(n)\right)^2\left\langle nL\,|\,r^{-s}\,|\,n'L'\right\rangle\left\langle n'L'\,|\,r^{-q}\,|\,nL\right\rangle = \\
&-\frac{sq}{s+q+1}\left(Q\left\langle r^{-(s+q+3)}\right\rangle_{nL}-L(L+1)\left\langle r^{-(s+q+4)}\right\rangle_{nL}\right) \\
&+\frac{1}{4}(s+q)(s+q+3)\left(-L(L+1)+L'(L'+1)\right)\left\langle r^{-(s+q+4)}\right\rangle_{nL} \\
&+\frac{1}{4}\left[-s(s+1)-L(L+1)+L'(L'+1)\right]\left[-q(q+1)-L(L+1)+L'(L'+1)\right]\left\langle r^{-(s+q+4)}\right\rangle_{nL}.
\end{aligned} \tag{2.21}$$

The resulting additional terms are referred to in the effective potential as the 2nd nonadiabatic terms. The derivation of Eq. 2.21 is also shown in Appendix A.

The second-order energy for a particular κ_1 and κ_2 may thus be written as an adiabatic term

$$\begin{aligned}
&E^{[2]}(\kappa_1,\kappa_2)_{\mathrm{AD}} = \\
&-\sum_{\lambda',J_c',L'}\left[\begin{array}{l}
(-1)^{J_c'-J_c}\begin{Bmatrix} K & L & J_c \\ \kappa_1 & J_c' & L' \end{Bmatrix}\begin{Bmatrix} K & L' & J_c' \\ \kappa_2 & J_c & L \end{Bmatrix}\begin{pmatrix} L & \kappa_1 & L' \\ 0 & 0 & 0 \end{pmatrix}\begin{pmatrix} L' & \kappa_2 & L \\ 0 & 0 & 0 \end{pmatrix}(2L+1)(2L'+1) \\
\dfrac{\left\langle gJ_c\left\|M^{[\kappa_1]}\right\|\lambda'J_c'\right\rangle\left\langle\lambda'J_c'\left\|M^{[\kappa_2]}\right\|gJ_c\right\rangle}{\Delta E(\lambda'J_c')}\left\langle r^{-(\kappa_1+\kappa_2+2)}\right\rangle_{nL}
\end{array}\right],
\end{aligned} \tag{2.22}$$

a 1st nonadiabatic term

$$\begin{aligned}
&E^{[2]}(\kappa_1,\kappa_2)_{\text{1st NA}} = \\
&-\sum_{\lambda',J_c',L'}\left[\begin{array}{l}
(-1)^{J_c'-J_c}\begin{Bmatrix} K & L & J_c \\ \kappa_1 & J_c' & L' \end{Bmatrix}\begin{Bmatrix} K & L' & J_c' \\ \kappa_2 & J_c & L \end{Bmatrix}\begin{pmatrix} L & \kappa_1 & L' \\ 0 & 0 & 0 \end{pmatrix}\begin{pmatrix} L' & \kappa_2 & L \\ 0 & 0 & 0 \end{pmatrix}(2L+1)(2L'+1) \\
\dfrac{\left\langle gJ_c\left\|M^{[\kappa_1]}\right\|\lambda'J_c'\right\rangle\left\langle\lambda'J_c'\left\|M^{[\kappa_2]}\right\|gJ_c\right\rangle}{\left(\Delta E(\lambda'J_c')\right)^2}\left(-\frac{1}{2}\left[(\kappa_1+1)(\kappa_2+1)-L(L+1)+L'(L'+1)\right]\right)\left\langle r^{-(\kappa_1+\kappa_2+4)}\right\rangle_{nL}
\end{array}\right],
\end{aligned} \tag{2.23}$$

and a 2nd nonadiabatic term

$$E^{[2]}(\kappa_1,\kappa_2)_{\text{2nd NA}} =$$
$$-\sum_{\lambda',J_c',L'}\left[\begin{array}{l}(-1)^{J_c'-J_c}\begin{Bmatrix}K & L & J_c\\ \kappa_1 & J_c' & L'\end{Bmatrix}\begin{Bmatrix}K & L' & J_c'\\ \kappa_2 & J_c & L\end{Bmatrix}\begin{pmatrix}L & \kappa_1 & L'\\ 0 & 0 & 0\end{pmatrix}\begin{pmatrix}L' & \kappa_2 & L\\ 0 & 0 & 0\end{pmatrix}(2L+1)(2L'+1)\dfrac{\left\langle gJ_c\left\|M^{[\kappa_1]}\right\|\lambda'J_c'\right\rangle\left\langle\lambda'J_c'\left\|M^{[\kappa_2]}\right\|gJ_c\right\rangle}{\left(\Delta E(\lambda'J_c')\right)^3}\\ \left(-\dfrac{(\kappa_1+1)(\kappa_2+1)}{\kappa_1+\kappa_2+3}Q\left\langle r^{-(\kappa_1+\kappa_2+5)}\right\rangle_{nL}+\left(\begin{array}{l}\dfrac{(\kappa_1+1)(\kappa_2+1)}{\kappa_1+\kappa_2+3}L(L+1)+\dfrac{1}{4}(\kappa_1+\kappa_2+2)(\kappa_1+\kappa_2+5)\left(-L(L+1)+L'(L'+1)\right)\\ +\dfrac{1}{4}\left[-(\kappa_1+1)(\kappa_1+2)-L(L+1)+L'(L'+1)\right]\left[-(\kappa_2+1)(\kappa_2+2)-L(L+1)+L'(L'+1)\right]\end{array}\right)\left\langle r^{-(\kappa_1+\kappa_2+6)}\right\rangle_{nL}\right)\end{array}\right].$$

(2.24)

Taken together this gives a total second-order energy, from electronically excited core levels, of

$$E^{[2]}(nL_K) = \sum_{\kappa_1,\kappa_2}\left[E^{[2]}(\kappa_1,\kappa_2)_{\text{AD}} + E^{[2]}(\kappa_1,\kappa_2)_{\text{1st NA}} + E^{[2]}(\kappa_1,\kappa_2)_{\text{2nd NA}}\right]. \tag{2.25}$$

Note that each successive term in the adiabatic expansion is proportional to higher inverse powers of the Rydberg radial coordinate.

The contributions to the second-order perturbation energy from a fixed multipole order (κ_1, κ_2) and adiabatic order (AD, 1st NA, 2nd NA) can each be decomposed into contributions of different tensor orders. This decomposition is most easily accomplished by noting that the entire dependence on *K* is contained in the product of two 6J-symbols that occurs in each of the expressions above. The $2J_c$ + 1 dimensional space corresponding to the different values of *K* for a common *L* is spanned by the basis vectors

$$V_b(K) = (-1)^{J_c+L+K}\begin{Bmatrix}K & L & J_c\\ b & J_c & L\end{Bmatrix}\sqrt{2b+1}\ \ (\text{b} = 0, 1, 2, ...), \tag{2.26}$$

which satisfy

$$\sum_K (2K+1)V_b(K)V_{b'}(K) = \delta_{bb'}. \tag{2.27}$$

The 6J-symbol products that occur in the energy expressions may be written as linear combinations of these basis vectors using Eq. 6.2.12 of Ref. [19]:

$$\begin{Bmatrix} K & L & J_c \\ \kappa_1 & J_c' & L' \end{Bmatrix} \begin{Bmatrix} K & L' & J_c' \\ \kappa_2 & J_c & L \end{Bmatrix} = \sum_{b=0}^{\infty} a_b\left(J_c', L'\right) V_b\left(K\right), \tag{2.28}$$

where

$$a_b\left(J_c', L'\right) = \left[(-1)^{L+L'} \begin{Bmatrix} L' & \kappa_1 & L \\ b & L & \kappa_2 \end{Bmatrix} \right] \left[(-1)^{J_c+J_c'} \begin{Bmatrix} J_c' & \kappa_1 & J_c \\ b & J_c & \kappa_2 \end{Bmatrix} \right] \left[(-1)^b \sqrt{2b+1} \right]. \tag{2.29}$$

Notice that this substitution factors the dependence on L' and J_c'. Notice also that the 6J-symbols restrict the possible tensor orders, *b*, to between $\left|\kappa_1 - \kappa_2\right|$ and $\left|\kappa_1 + \kappa_2\right|$, with an upper limit of the smaller of 2*L* and 2 J_c.

Substituting this result into the energy expressions allows each to be written as a sum of tensor orders:

$$E^{[2]}\left(nL_K\right) = \sum_b E_b^{[2]}\left(nL_K\right), \tag{2.30}$$

where

$$E_b^{[2]}\left(nL_K\right) = \sum_{\kappa_1,\kappa_2} E_b^{[2]}\left(\kappa_1,\kappa_2\right)_{\text{AD}} + E_b^{[2]}\left(\kappa_1,\kappa_2\right)_{\text{1st NA}} + E_b^{[2]}\left(\kappa_1,\kappa_2\right)_{\text{2nd NA}}. \tag{2.31}$$

Since the resulting expressions separate the terms involving L', the sum over L' may be segregated in each expression, defining the functions $f1_b\left(\kappa_1,\kappa_2\right)$, $f2_b\left(\kappa_1,\kappa_2\right)$, $f3_b\left(\kappa_1,\kappa_2\right)$, and $f4_b\left(\kappa_1,\kappa_2\right)$. The adiabatic term becomes

$$\begin{aligned} E_b^{[2]}\left(\kappa_1,\kappa_2\right)_{\text{AD}} = & \left[\sum_{\lambda', J_c'} (-1)^{2J_c'} \begin{Bmatrix} J_c' & \kappa_1 & J_c \\ b & J_c & \kappa_2 \end{Bmatrix} \frac{\left\langle gJ_c \left\| M^{[\kappa_1]} \right\| \lambda' J_c' \right\rangle \left\langle \lambda' J_c' \left\| M^{[\kappa_2]} \right\| gJ_c \right\rangle}{\Delta E\left(\lambda' J_c'\right)} \right], \\ & \times f1_b\left(\kappa_1,\kappa_2\right) \left[(-1)^{b+1} \sqrt{2b+1} \left\langle r^{-(\kappa_1+\kappa_2+2)} \right\rangle_{nL} V_b\left(K\right) \right] \end{aligned} \tag{2.32}$$

where

$$f1_b(\kappa_1,\kappa_2)=\sum_{L'}(-1)^{L+L'}\begin{pmatrix}L & \kappa_1 & L'\\ 0 & 0 & 0\end{pmatrix}\begin{pmatrix}L & \kappa_2 & L'\\ 0 & 0 & 0\end{pmatrix}(2L+1)(2L'+1)\begin{Bmatrix}L' & \kappa_1 & L\\ b & L & \kappa_2\end{Bmatrix}, \quad (2.33)$$

while the 1st nonadiabatic term is written as

$$E_b^{[2]}(\kappa_1,\kappa_2)_{\text{1st NA}}=\left[\sum_{\lambda',J_c'}(-1)^{2J_c'}\begin{Bmatrix}J_c' & \kappa_1 & J_c\\ b & J_c & \kappa_2\end{Bmatrix}\frac{\left\langle gJ_c\left\|M^{[\kappa_1]}\right\|\lambda_c'J_c'\right\rangle\left\langle\lambda'J_c'\left\|M^{[\kappa_2]}\right\|gJ_c\right\rangle}{\left(\Delta E(\lambda'J_c')\right)^2}\right], \quad (2.34)$$
$$\times f2_b(\kappa_1,\kappa_2)\left[(-1)^{b+1}\sqrt{2b+1}\left\langle r^{-(\kappa_1+\kappa_2+4)}\right\rangle_{nL}V_b(K)\right]$$

with

$$f2_b(\kappa_1,\kappa_2)=\sum_{L'}(-1)^{L+L'}\begin{pmatrix}L & \kappa_1 & L'\\ 0 & 0 & 0\end{pmatrix}\begin{pmatrix}L & \kappa_2 & L'\\ 0 & 0 & 0\end{pmatrix}(2L+1)(2L'+1)\begin{Bmatrix}L' & \kappa_1 & L\\ b & L & \kappa_2\end{Bmatrix}, \quad (2.35)$$
$$\times-\frac{1}{2}\left[(\kappa_1+1)(\kappa_2+1)-L(L+1)+L'(L'+1)\right]$$

and the 2nd nonadiabatic term becomes

$$E_b^{[2]}(\kappa_1,\kappa_2)_{\text{2nd NA}}=\left[\sum_{\lambda',J_c'}(-1)^{2J_c'}\begin{Bmatrix}J_c' & \kappa_1 & J_c\\ b & J_c & \kappa_2\end{Bmatrix}\frac{\left\langle gJ_c\left\|M^{[\kappa_1]}\right\|\lambda'J_c'\right\rangle\left\langle\lambda'J_c'\left\|M^{[\kappa_2]}\right\|gJ_c\right\rangle}{\left(\Delta E(\lambda'J_c')\right)^3}\right],$$
$$\times\left[f3_b(\kappa_1,\kappa_2)\left\langle r^{-(\kappa_1+\kappa_2+5)}\right\rangle_{nL}+f4_b(\kappa_1,\kappa_2)\left\langle r^{-(\kappa_1+\kappa_2+6)}\right\rangle_{nL}\right]\left[(-1)^{b+1}\sqrt{2b+1}\,V_b(K)\right] \quad (2.36)$$

with

$$f3_b(\kappa_1,\kappa_2)=\sum_{L'}(-1)^{L+L'}\begin{pmatrix}L & \kappa_1 & L'\\ 0 & 0 & 0\end{pmatrix}\begin{pmatrix}L & \kappa_2 & L'\\ 0 & 0 & 0\end{pmatrix}(2L+1)(2L'+1)\begin{Bmatrix}L' & \kappa_1 & L\\ b & L & \kappa_2\end{Bmatrix} \quad (2.37)$$
$$\times\left[-\frac{(\kappa_1+1)(\kappa_2+1)}{\kappa_1+\kappa_2+3}Q\right]$$

and

$$
\begin{aligned}
& f4_b(\kappa_1,\kappa_2) = \\
& \sum_{L'} (-1)^{L+L'} \begin{pmatrix} L & \kappa_1 & L' \\ 0 & 0 & 0 \end{pmatrix} \begin{pmatrix} L & \kappa_2 & L' \\ 0 & 0 & 0 \end{pmatrix} (2L+1)(2L'+1) \begin{Bmatrix} L' & \kappa_1 & L \\ b & L & \kappa_2 \end{Bmatrix} \\
& \times \left[\begin{array}{l} \dfrac{(\kappa_1+1)(\kappa_2+1)}{\kappa_1+\kappa_2+3} L(L+1) + \dfrac{1}{4}(\kappa_1+\kappa_2+2)(\kappa_1+\kappa_2+5)\left(-L(L+1)+L'(L'+1)\right) \\ + \dfrac{1}{4}\left[-(\kappa_1+1)(\kappa_1+2)-L(L+1)+L'(L'+1)\right]\left[-(\kappa_2+1)(\kappa_2+2)-L(L+1)+L'(L'+1)\right] \end{array} \right].
\end{aligned}
$$

(2.38)

Calculations for the "f functions" are shown in Appendix B. Ref. [19] provides the formulas for calculating 3J-symbols and the 6J-symbols when b = 0, 1, and 2. Ref. [20] gives expressions for calculating W coefficients, which can then be related to the 6J-symbols for b = 3 and 4 using Eq. 6.2.13 of Ref. [19]. The sum over J_c', however, becomes part of the core properties $\alpha_{M,b}$, $\beta_{M,b}$, and $\gamma_{M,b}$. The Greek symbols correspond to the different terms in the adiabatic expansion: α for the adiabatic term, β for the first nonadiabatic term, and γ for the second nonadiabatic term. The first subscript indicates the term in the potential that the parameter depends on (*D* for dipole-dipole, *DO* for dipole-octupole, etc.) while the second subscript denotes the tensor order.

To simplify the appearance of the final expressions for the second-order perturbation energy, the basis vectors V_b are rewritten in more familiar form. For example, the scalar basis vector $V_0(K)$ is simply a constant dependent on *L* and J_c,

$$
V_0(K) = \frac{1}{\sqrt{2J_c+1}} \frac{1}{\sqrt{2L+1}}. \tag{2.39}
$$

Note that the scalar term requires that κ_1 equal κ_2, allowing the 6J-symbol in the J_c' sum to be rewritten as

$$\begin{Bmatrix} J_c' & \kappa & J_c \\ 0 & J_c & \kappa \end{Bmatrix} = (-1)^{J_c'+J_c+\kappa} \frac{1}{\sqrt{2\kappa+1}} \frac{1}{\sqrt{2J_c+1}}, \tag{2.40}$$

where κ has replaced κ_1 and κ_2. With these substitutions, the scalar terms in the second-order energy become:

$$E_0^{[2]}(nL_K) = -\frac{1}{2}\left(\alpha_{D,0}\left\langle r^{-4}\right\rangle_{nL} + \left(\alpha_{Q,0} - 6\beta_{D,0}\right)\left\langle r^{-6}\right\rangle_{nL} - \frac{16Q}{5}\gamma_{D,0}\left\langle r^{-7}\right\rangle_{nL} + \left(\alpha_{O,0} - 6\beta_{Q,0} + 72\gamma_{D,0}\left(1+\frac{L(L+1)}{10}\right)\right)\left\langle r^{-8}\right\rangle_{nL}\right), \tag{2.41}$$

where the coefficients in front of the core parameters follow the convention of Ref. [12]. The core parameters are given by

$$\alpha_{D,0} = \frac{2}{3}\frac{1}{2J_c+1}\sum_{\lambda',J_c'} \frac{\left\langle gJ_c \left\| M^{[1]} \right\| \lambda' J_c' \right\rangle^2}{\Delta E\left(\lambda' J_c'\right)}, \tag{2.42}$$

$$\alpha_{Q,0} = \frac{2}{5}\frac{1}{2J_c+1}\sum_{\lambda',J_c'} \frac{\left\langle gJ_c \left\| M^{[2]} \right\| \lambda' J_c' \right\rangle^2}{\Delta E\left(\lambda' J_c'\right)}, \tag{2.43}$$

$$\alpha_{O,0} = \frac{2}{7}\frac{1}{2J_c+1}\sum_{\lambda',J_c'} \frac{\left\langle gJ_c \left\| M^{[3]} \right\| \lambda' J_c' \right\rangle^2}{\Delta E\left(\lambda' J_c'\right)}, \tag{2.44}$$

$$\beta_{D,0} = \frac{1}{3}\frac{1}{2J_c+1}\sum_{\lambda',J_c'} \frac{\left\langle gJ_c \left\| M^{[1]} \right\| \lambda' J_c' \right\rangle^2}{\left(\Delta E\left(\lambda' J_c'\right)\right)^2}, \tag{2.45}$$

$$\beta_{Q,0} = \frac{1}{2}\frac{1}{2J_c+1}\sum_{\lambda',J_c'} \frac{\left\langle gJ_c \left\| M^{[2]} \right\| \lambda' J_c' \right\rangle^2}{\left(\Delta E\left(\lambda' J_c'\right)\right)^2}, \tag{2.46}$$

and

$$\gamma_{D,0} = \frac{1}{6}\frac{1}{2J_c+1}\sum_{\lambda',J_c'}\frac{\left\langle gJ_c \left\| M^{[1]} \right\| \lambda' J_c' \right\rangle^2}{\left(\Delta E\left(\lambda' J_c'\right)\right)^3}. \tag{2.47}$$

Notice that the summed quantities are positive definite, so each of the scalar coefficients is a simple sum of the contributions from the several possible branches characterized by J_c'. The terms proportional to r^{-4} and r^{-6} are well known. The later terms are analogous to those derived by Drachman, but are not restricted to the special case $J_c = 0$. The terms proportional to r^{-4} and r^{-6} agree with the results of Clark, Greene, and Miecznik [18] except that their expression for the coefficient analogous to $\beta_{D,0}$ contains an additional contribution (the second term in their Eq. 28).

The vector term of the second-order energy ($b = 1$) can be written as

$$E_1^{[2]}\left(nL_K\right) = \left(\beta_{D,1}\left\langle r^{-6}\right\rangle_{nL} + \left(\beta_{Q,1}+\gamma_{D,1}\right)\left\langle r^{-8}\right\rangle_{nL}\right)\vec{L}\cdot\vec{J}_c\,, \tag{2.48}$$

since

$$\begin{aligned} V_1(K) &= (-1)^{J_c+L+K}\begin{Bmatrix} K & L & J_c \\ 1 & J_c & L \end{Bmatrix}\sqrt{2\cdot 1+1} \\ &= \frac{4\sqrt{3}}{\sqrt{2J_c\left(2J_c+1\right)\left(2J_c+2\right)}}\frac{\vec{L}\cdot\vec{J}_c}{\sqrt{2L\left(2L+1\right)\left(2L+2\right)}} \end{aligned}, \tag{2.49}$$

and

$$\vec{L}\cdot\vec{J}_c = \frac{1}{2}\left[K\left(K+1\right) - L\left(L+1\right) - J_c\left(J_c+1\right)\right]. \tag{2.50}$$

The core parameters are defined by

$$\beta_{D,1} = \frac{\sqrt{6}}{\sqrt{2J_c\left(2J_c+1\right)\left(2J_c+2\right)}}\sum_{\lambda',J_c'}(-1)^{J_c'+J_c}\begin{Bmatrix} J_c' & 1 & J_c \\ 1 & J_c & 1 \end{Bmatrix}\frac{\left\langle gJ_c \left\| M^{[1]} \right\| \lambda' J_c' \right\rangle^2}{\left(\Delta E\left(\lambda' J_c'\right)\right)^2}, \tag{2.51}$$

$$\beta_{Q,1} = -3\sqrt{\frac{6}{5}} \frac{1}{\sqrt{2J_c(2J_c+1)(2J_c+2)}} \sum_{\lambda', J_c'} (-1)^{J_c'+J_c} \begin{Bmatrix} J_c' & 2 & J_c \\ 1 & J_c & 2 \end{Bmatrix} \frac{\left\langle gJ_c \left\| M^{[2]} \right\| \lambda' J_c' \right\rangle^2}{\left(\Delta E(\lambda' J_c')\right)^2}, \quad (2.52)$$

and

$$\gamma_{D,1} = -9\sqrt{6} \frac{1}{\sqrt{2J_c(2J_c+1)(2J_c+2)}} \sum_{\lambda', J_c'} (-1)^{J_c'+J_c} \begin{Bmatrix} J_c' & 1 & J_c \\ 1 & J_c & 1 \end{Bmatrix} \frac{\left\langle gJ_c \left\| M^{[1]} \right\| \lambda' J_c' \right\rangle^2}{\left(\Delta E(\lambda' J_c')\right)^3}. \quad (2.53)$$

In this case, the contributions of the several J_c' branches may either add or subtract from the total coefficient. Notice also that there is no adiabatic vector term. This is due to a cancellation between the contributions of adiabatic terms with different L'. A similar cancellation does not occur in the nonadiabatic terms because of the extra factors of L and L' that occur in Eqs. 2.20 and 2.21. The vector term in high-L Rydberg fine structure has an interesting history, discussed later in Section 2.3. The existence of a vector term in Rydberg electric fine structure was first predicted by Zygelman [21]. Its coefficient was first calculated by Clark, Greene, and Miecznik [18], who also emphasized its essentially nonadiabatic nature. The expression for $\beta_{D,1}$ agrees with their result. The terms proportional to r^{-8} are new. In nature these terms compete with a much larger vector term due to the magnetic dipole moment of the core electron, discussed in Section 2.2D. Nevertheless, the electric vector structure has been measured in both argon [5] and neon [4].

For consistency with previous publications and with the leading term from Section 2.2A proportional to the quadrupole moment, the $b = 2$ basis vector is written as proportional to

$$\frac{\left\langle X^{[2]}(J_c) \cdot C^{[2]}(\hat{r}) \right\rangle}{\begin{pmatrix} J_c & 2 & J_c \\ -J_c & 0 & J_c \end{pmatrix}} \quad (2.54)$$

given that

$$V_2(K)=(-1)^{J_c+L+K}\begin{Bmatrix} K & L & J_c \\ 2 & J_c & L \end{Bmatrix}\sqrt{2\cdot 2+1}=-2\sqrt{5}\,\frac{\left\langle X^{[2]}(J_c)\cdot C^{[2]}(\hat{r})\right\rangle}{\sqrt{\frac{2L(2L+1)(2L+2)}{(2L-1)(2L+3)}}}. \qquad (2.55)$$

This leads to tensor terms of the form:

$$E_2^{[2]}(nL_K)= -\frac{1}{2}\begin{pmatrix} \alpha_{D,2}\left\langle r^{-4}\right\rangle_{nL}+\left(\alpha_{Q,2}-6\beta_{D,2}+\alpha_{DO,2}\right)\left\langle r^{-6}\right\rangle_{nL}-\frac{16Q}{5}\gamma_{D,2}\left\langle r^{-7}\right\rangle_{nL} \\ +\left(\alpha_{O,2}-6\beta_{Q,2}+\alpha_{QH,2}-6\beta_{DO,2}+72\left(\frac{1}{4}+\frac{L(L+1)}{10}\right)\gamma_{D,2}\right)\left\langle r^{-8}\right\rangle_{nL} \end{pmatrix}\frac{\left\langle X^{[2]}(J_c)\cdot C^{[2]}(\hat{r})\right\rangle}{\begin{pmatrix} J_c & 2 & J_c \\ -J_c & 0 & J_c \end{pmatrix}}, \qquad (2.56)$$

where the core parameters are given by

$$\alpha_{D,2}=2\sqrt{\frac{10}{3}}\begin{pmatrix} J_c & 2 & J_c \\ -J_c & 0 & J_c \end{pmatrix}\sum_{\lambda',J_c'}(-1)^{J_c'+J_c}\begin{Bmatrix} J_c' & 1 & J_c \\ 2 & J_c & 1 \end{Bmatrix}\frac{\left\langle gJ_c\left\|M^{[1]}\right\|\lambda' J_c'\right\rangle^2}{\Delta E(\lambda' J_c')}, \qquad (2.57)$$

$$\alpha_{Q,2}=-2\sqrt{\frac{10}{7}}\begin{pmatrix} J_c & 2 & J_c \\ -J_c & 0 & J_c \end{pmatrix}\sum_{\lambda',J_c'}(-1)^{J_c'+J_c}\begin{Bmatrix} J_c' & 2 & J_c \\ 2 & J_c & 2 \end{Bmatrix}\frac{\left\langle gJ_c\left\|M^{[2]}\right\|\lambda' J_c'\right\rangle^2}{\Delta E(\lambda' J_c')}, \qquad (2.58)$$

$$\alpha_{O,2}=\frac{4}{3}\sqrt{\frac{15}{7}}\begin{pmatrix} J_c & 2 & J_c \\ -J_c & 0 & J_c \end{pmatrix}\sum_{\lambda',J_c'}(-1)^{J_c'+J_c}\begin{Bmatrix} J_c' & 3 & J_c \\ 2 & J_c & 3 \end{Bmatrix}\frac{\left\langle gJ_c\left\|M^{[3]}\right\|\lambda' J_c'\right\rangle^2}{\Delta E(\lambda' J_c')}, \qquad (2.59)$$

$$\alpha_{DO,2}= -4\sqrt{\frac{15}{7}}\begin{pmatrix} J_c & 2 & J_c \\ -J_c & 0 & J_c \end{pmatrix}\sum_{\lambda',J_c'}(-1)^{2J_c'}\begin{Bmatrix} J_c' & 1 & J_c \\ 2 & J_c & 3 \end{Bmatrix}\frac{\left\langle gJ_c\left\|M^{[1]}\right\|\lambda' J_c'\right\rangle\left\langle \lambda' J_c'\left\|M^{[3]}\right\|gJ_c\right\rangle}{\Delta E(\lambda' J_c')}, \qquad (2.60)$$

$$\alpha_{QH,2}= 4\sqrt{\frac{10}{7}}\begin{pmatrix} J_c & 2 & J_c \\ -J_c & 0 & J_c \end{pmatrix}\sum_{\lambda',J_c'}(-1)^{2J_c'}\begin{Bmatrix} J_c' & 2 & J_c \\ 2 & J_c & 4 \end{Bmatrix}\frac{\left\langle gJ_c\left\|M^{[2]}\right\|\lambda' J_c'\right\rangle\left\langle \lambda' J_c'\left\|M^{[4]}\right\|gJ_c\right\rangle}{\Delta E(\lambda' J_c')}, \qquad (2.61)$$

$$\beta_{D,2} = \frac{1}{2}\sqrt{\frac{10}{3}}\begin{pmatrix} J_c & 2 & J_c \\ -J_c & 0 & J_c \end{pmatrix}\sum_{\lambda',J_c'}(-1)^{J_c'+J_c}\begin{Bmatrix} J_c' & 1 & J_c \\ 2 & J_c & 1 \end{Bmatrix}\frac{\left\langle gJ_c\left\|M^{[1]}\right\|\lambda' J_c'\right\rangle^2}{\left(\Delta E\left(\lambda' J_c'\right)\right)^2}, \tag{2.62}$$

$$\beta_{Q,2} = -2\sqrt{\frac{10}{7}}\begin{pmatrix} J_c & 2 & J_c \\ -J_c & 0 & J_c \end{pmatrix}\sum_{\lambda',J_c'}(-1)^{J_c'+J_c}\begin{Bmatrix} J_c' & 2 & J_c \\ 2 & J_c & 2 \end{Bmatrix}\frac{\left\langle gJ_c\left\|M^{[2]}\right\|\lambda' J_c'\right\rangle^2}{\left(\Delta E\left(\lambda' J_c'\right)\right)^2}, \tag{2.63}$$

$$\beta_{DO,2} =$$
$$-4\sqrt{\frac{15}{7}}\begin{pmatrix} J_c & 2 & J_c \\ -J_c & 0 & J_c \end{pmatrix}\sum_{\lambda',J_c'}(-1)^{2J_c'}\begin{Bmatrix} J_c' & 1 & J_c \\ 2 & J_c & 3 \end{Bmatrix}\frac{\left\langle gJ_c\left\|M^{[1]}\right\|\lambda' J_c'\right\rangle\left\langle \lambda' J_c'\left\|M^{[3]}\right\|gJ_c\right\rangle}{\left(\Delta E\left(\lambda' J_c'\right)\right)^2}, \tag{2.64}$$

$$\gamma_{D,2} = \frac{1}{2}\sqrt{\frac{10}{3}}\begin{pmatrix} J_c & 2 & J_c \\ -J_c & 0 & J_c \end{pmatrix}\sum_{\lambda',J_c'}(-1)^{J_c'+J_c}\begin{Bmatrix} J_c' & 1 & J_c \\ 2 & J_c & 1 \end{Bmatrix}\frac{\left\langle gJ_c\left\|M^{[1]}\right\|\lambda' J_c'\right\rangle^2}{\left(\Delta E\left(\lambda' J_c'\right)\right)^3}. \tag{2.65}$$

The term proportional to r^{-4} is standard, and the expression for $\alpha_{D,2}$ agrees with that first described by Angel and Sandars [22]. The terms proportional to r^{-6} agree with the results of Clark, Greene, and Miecznik [18], except for an additional term that is included in their Eq. 29. The additional terms are new.

The portion of $E^{[2]}$ proportional to the scalar product of third-rank tensors is initially found as a multiple of $V_3(K)$:

$$V_3(K) = \sqrt{7}\left\langle X^{[3]}(J_c)\cdot X^{[3]}(\hat{r})\right\rangle, \tag{2.66}$$

where $X^{[3]}(J_c)$ and $X^{[3]}(\hat{r})$ are unit tensors. Since only matrix elements diagonal in *L* are desired for this term, it is convenient to write it in terms of a specific third-rank tensor

$$T^{[3]}(\hat{r}) \equiv \left(C^{[2]}(\hat{r})\otimes\vec{L}\right)^{[3]}, \tag{2.67}$$

whose reduced matrix elements are given by:

$$\left\langle L\left|T^{[3]}\left(\hat{r}\right)\right|L\right\rangle = -\frac{1}{4}\sqrt{\frac{3}{5}}\sqrt{\frac{(2L-2)2L(2L+1)(2L+2)(2L+4)}{(2L-1)(2L+3)}}\,. \tag{2.68}$$

The resulting contributions to $E^{[2]}$ are

$$E_3^{[2]}\left(nL_K\right) = \left(\beta_{Q,3}+\beta_{DO,3}\right)\left\langle r^{-8}\right\rangle_{nL}\left\langle X^{[3]}\left(J_c\right)\cdot T^{[3]}\left(\hat{r}\right)\right\rangle, \tag{2.69}$$

with the core parameters defined as

$$\beta_{Q,3} = \sqrt{\frac{21}{2}}\sum_{\lambda',J_c'}(-1)^{J_c'+J_c}\begin{Bmatrix} J_c' & 2 & J_c \\ 3 & J_c & 2\end{Bmatrix}\frac{\left\langle gJ_c\left\|M^{[2]}\right\|\lambda' J_c'\right\rangle^2}{\left(\Delta E\left(\lambda' J_c'\right)\right)^2}, \tag{2.70}$$

and

$$\beta_{DO,3} = \sqrt{35}\sum_{\lambda',J_c'}(-1)^{2J_c'}\begin{Bmatrix} J_c' & 1 & J_c \\ 3 & J_c & 3\end{Bmatrix}\frac{\left\langle gJ_c\left\|M^{[1]}\right\|\lambda' J_c'\right\rangle\left\langle \lambda' J_c'\left\|M^{[3]}\right\|gJ_c\right\rangle}{\left(\Delta E\left(\lambda' J_c'\right)\right)^2}. \tag{2.71}$$

Notice, again, that there is no adiabatic term in the third-rank tensor portion of $E^{[2]}$. This is similar to the vector term and suggests that all odd-order adiabatic contributions will be zero. Prior to the study of nickel presented later in Chapter 4, no experimental evidence of such third-rank tensor structure had been seen. As with the vector structure, it is possible that magnetic structure, in this case magnetic octupole structure, could compete with third-rank electric fine structure. This would be expected to be proportional to the permanent octupole moment of the core ion (requiring $J_c > 1$) and to the inverse fifth power of Rydberg radial coordinate.

For $b = 4$, the leading term from Section 2.2A is proportional to the core's hexadecapole moment and is given in Eq. 2.13. For consistency, the terms in the effective potential of this order are also written as proportional to

$$\frac{\left\langle X^{[4]}(J_c)\cdot C^{[4]}(\hat{r})\right\rangle}{\begin{pmatrix} J_c & 4 & J_c \\ -J_c & 0 & J_c \end{pmatrix}}, \tag{2.72}$$

where

$$V_4(K) = 8\frac{\left\langle X^{[4]}(J_c)\cdot C^{[4]}(\hat{r})\right\rangle}{\sqrt{\frac{(2L-2)2L(2L+1)(2L+2)(2L+4)}{(2L-3)(2L-1)(2L+3)(2L+5)}}}. \tag{2.73}$$

The energy thus becomes

$$E_4^{[2]}(nL_K) = -\frac{1}{2}\left[\left(\alpha_{Q,4}+\alpha_{DO,4}\right)\left\langle r^{-6}\right\rangle_{nL} + \left(\alpha_{O,4}-6\beta_{Q,4}+\alpha_{QH,4}-6\beta_{DO,4}\right)\left\langle r^{-8}\right\rangle_{nL}\right]\frac{\left\langle X^{[4]}(J_c)\cdot C^{[4]}(\hat{r})\right\rangle}{\begin{pmatrix} J_c & 4 & J_c \\ -J_c & 0 & J_c \end{pmatrix}}, \tag{2.74}$$

where

$$\alpha_{Q,4} = \frac{18}{5}\sqrt{\frac{10}{7}}\begin{pmatrix} J_c & 4 & J_c \\ -J_c & 0 & J_c \end{pmatrix}\sum_{\lambda',J_c'}(-1)^{J_c'+J_c}\begin{Bmatrix} J_c' & 2 & J_c \\ 4 & J_c & 2 \end{Bmatrix}\frac{\left\langle gJ_c\left\|M^{[2]}\right\|\lambda' J_c'\right\rangle^2}{\Delta E(\lambda' J_c')}, \tag{2.75}$$

$$\alpha_{O,4} = -18\sqrt{\frac{2}{77}}\begin{pmatrix} J_c & 4 & J_c \\ -J_c & 0 & J_c \end{pmatrix}\sum_{\lambda',J_c'}(-1)^{J_c'+J_c}\begin{Bmatrix} J_c' & 3 & J_c \\ 4 & J_c & 3 \end{Bmatrix}\frac{\left\langle gJ_c\left\|M^{[3]}\right\|\lambda' J_c'\right\rangle^2}{\Delta E(\lambda' J_c')}, \tag{2.76}$$

$$\alpha_{DO,4} = 24\sqrt{\frac{1}{7}}\begin{pmatrix} J_c & 4 & J_c \\ -J_c & 0 & J_c \end{pmatrix}\sum_{\lambda',J_c'}(-1)^{2J_c'}\begin{Bmatrix} J_c' & 1 & J_c \\ 4 & J_c & 3 \end{Bmatrix}\frac{\left\langle gJ_c\left\|M^{[1]}\right\|\lambda' J_c'\right\rangle\left\langle \lambda' J_c'\left\|M^{[3]}\right\|gJ_c\right\rangle}{\Delta E(\lambda' J_c')}, \tag{2.77}$$

$$\alpha_{QH,4} = -24\sqrt{\frac{5}{77}}\begin{pmatrix} J_c & 4 & J_c \\ -J_c & 0 & J_c \end{pmatrix}\sum_{\lambda',J_c'}(-1)^{2J_c'}\begin{Bmatrix} J_c' & 2 & J_c \\ 4 & J_c & 4 \end{Bmatrix}\frac{\left\langle gJ_c\left\|M^{[2]}\right\|\lambda' J_c'\right\rangle\left\langle \lambda' J_c'\left\|M^{[4]}\right\|gJ_c\right\rangle}{\Delta E(\lambda' J_c')}, \tag{2.78}$$

$$\beta_{Q,4} = \frac{3}{2}\sqrt{\frac{10}{7}}\begin{pmatrix} J_c & 4 & J_c \\ -J_c & 0 & J_c \end{pmatrix}\sum_{\lambda', J_c'} (-1)^{J_c'+J_c} \begin{Bmatrix} J_c' & 2 & J_c \\ 4 & J_c & 2 \end{Bmatrix} \frac{\left\langle gJ_c \left\| M^{[2]} \right\| \lambda' J_c' \right\rangle^2}{\left(\Delta E\left(\lambda' J_c'\right)\right)^2}, \qquad (2.79)$$

and

$$\beta_{DO,4} =$$
$$10\sqrt{\frac{1}{7}}\begin{pmatrix} J_c & 4 & J_c \\ -J_c & 0 & J_c \end{pmatrix}\sum_{\lambda', J_c'} (-1)^{2J_c'} \begin{Bmatrix} J_c' & 1 & J_c \\ 4 & J_c & 3 \end{Bmatrix} \frac{\left\langle gJ_c \left\| M^{[1]} \right\| \lambda' J_c' \right\rangle \left\langle \lambda' J_c' \left\| M^{[3]} \right\| gJ_c \right\rangle}{\left(\Delta E\left(\lambda' J_c'\right)\right)^2}. \qquad (2.80)$$

The two terms proportional to r^{-6} agree with the results of Clark, Greene, and Miecznik [18]. The other terms are new.

This completes the list of terms which contribute to $E^{[2]}$ proportional to r^{-s} with $s \le 8$, as long as $J_c < 3$. This is sufficient to account for all cases studied experimentally to date. The full effective potential to this point consists of the sum of all the second-order terms listed above plus the two first-order terms from Eq. 2.13.

2.2C Rydberg Intermediate States

The expression for the second-order perturbation energy derived in Section 2.2B excluded the contributions to $E^{[2]}$ from intermediate states where the core was in its ground electronic state. The number of such states depends on the ion in question. For an ion with an *S*-state ground electronic state, for example, there is only one ground state. However, for ions with higher angular momentum there may be two or more fine structure levels within the same electronic state. For example, the ion Ar^+ has a $^2P_{3/2}$ ground state and a $^2P_{1/2}$ excited level within the same electronic state. Any state of the combined system in which the core is in the ground electronic state is considered to be a "Rydberg state" and denote it by

$$\left(gJ_c'\right)n'L_K'. \qquad (2.81)$$

The contribution of such states to the second-order perturbation energy, omitted in Section 2.2B, is given by

$$E_{RS}^{[2]}\left(nL_K\right) = -\sum_{J_c',n',L'}{}' \frac{\left\langle \left(gJ_c\right)nL_K \left| V \right| \left(gJ_c'\right)n'L_K' \right\rangle \left\langle \left(gJ_c'\right)n'L_K' \left| V \right| \left(gJ_c\right)nL_K \right\rangle}{\Delta E\left(gJ_c'\right) + E\left(n'\right) - E\left(n\right)} \tag{2.82}$$

where the prime on the summation symbol indicates that the intermediate states do not include the initial state $\left(gJ_c\right)nL_K$. This term describes the shift in energy of a particular Rydberg level $\left(gJ_c\right)nL_K$ due to its coupling with other Rydberg states, either bound to the same core fine structure level $\left(J_c\right)$ or to a different fine structure level $\left(J_c'\right)$. Note that only the even operators in *V* give nonzero results given the constraints due to parity. In low-*L* Rydberg levels, it is usual for these couplings to be strong, leading to perturbation of one Rydberg series by another. When these perturbations are strong compared to the spacing between adjacent Rydberg states, they make it necessary to describe the Rydberg structure using the formalism of multi-channel quantum defect theory (MCQDT). In high-*L* Rydberg levels the effects of these couplings are generally very small, partly because all the matrix elements of *V* decrease rapidly with *L*. For example, even the diagonal elements of the leading multipole (quadrupole) term in *V* decrease approximately as L^{-3}. Thus as *L* increases, all the effects of inter-series coupling decrease rapidly and become small corrections to the Rydberg energies. Of course, an exception would occur if, by chance, two Rydberg states bound to two different core levels happened to be very nearly degenerate so that even a small coupling matrix element would produce a large shift in energy. Another possible near degeneracy arises between Rydberg levels bound to the core ground state $\left(J_c\right)$ and having the same *n* but different *L*. One might assume that the quadrupole term in *V* would lead to strong coupling between the $\left(J_c\right)nL_K$ and $\left(J_c\right)n\left(L\pm 2\right)_K$ levels, which

are nearly degenerate even after the first-order perturbation energies are applied. However, in this case, the quadrupole coupling is identically zero for hydrogenic wave functions because of the selection rule

$$\left\langle nL\left|r^{-3}\right|n,L\pm 2\right\rangle = 0\,. \tag{2.83}$$

Higher permanent moments could, in principal, couple such levels, but in practice the energies of these Rydberg levels differ as a result of the first- and second-order energies discussed in Sections 2.2A and 2.2B above. The weak couplings due to the hexadecapole and higher multipoles in V produce only very minor energy shifts even when $J_c' = J_c$ and $n' = n$. The main effect of the quadrupole couplings is through nondegenerate intermediate states. It is given by

$$\begin{aligned} E_{RS}^{[2]}(QQ) &= -\sum_{J_c',n',L}{}' \frac{\left\langle (gJ_c)nL_K\left|M^{[2]}\cdot\frac{C^{[2]}(\hat{r})}{r^3}\right|(gJ_c')n'L_K'\right\rangle\left\langle (gJ_c')n'L_K'\left|M^{[2]}\cdot\frac{C^{[2]}(\hat{r})}{r^3}\right|(gJ_c)nL_K\right\rangle}{\Delta E(gJ_c')+E(n')-E(n)} \\ &= -\sum_{J_c',n',L}{}' \begin{Bmatrix} K & L & J_c \\ 2 & J_c' & L' \end{Bmatrix}^2 \begin{pmatrix} L & 2 & L' \\ 0 & 0 & 0 \end{pmatrix}^2 (2L+1)(2L'+1)\left\langle gJ_c\left\|M^{[2]}\right\|gJ_c'\right\rangle^2 \frac{\left\langle nL\left|r^{-3}\right|n'L'\right\rangle^2}{\Delta E(gJ_c')+E(n')-E(n)} \end{aligned} . \tag{2.84}$$

Evaluation of this expression requires the off-diagonal matrix elements of the quadrupole operator between the ground state fine structure levels. The diagonal element is easily estimated from the gross features of the high-L Rydberg fine structure, which reveal the ground state quadrupole moment. Assuming that the ground state levels are approximately LS-coupled leads to an estimate of the off-diagonal element that is typically of sufficient precision. The selection rules for couplings due to the quadrupole term are ΔJ_c = 0, ±1, ±2, and ΔL = 0, ±2.

The primary difficulty in evaluating Eq. 2.84 is carrying out the sum over n', which includes both discrete and continuum levels. Because of the quadratic dependence of the

centrifugal potential on L', the $L' = L + 2$ sum is especially dependent on the continuum contributions. The sum may be evaluated by explicit summation over a range of discrete levels and integration over continuum levels. Alternatively, it can be evaluated using the method of Dalgarno and Lewis [23] where

$$\sum_{n'} \frac{\langle nL|r^{-s}|n'L'\rangle\langle n'L'|r^{-q}|nL\rangle}{\Delta E(gJ_c') + E(n') - E(n)} = \langle nL|r^{-s}|f(r)\rangle \tag{2.85}$$

where the function $f(r)$ is the first-order correction to the wave function $|nL\rangle$ and satisfies a differential equation specific to each (J_c', L') series [24].

The results of Sections 2.2A and 2.2B can be described as an effective potential in the space of Rydberg levels whose expectation value gives the most important contributions to the Rydberg energies. Since the quadrupole term is the leading term in the effective potential and Eq. 2.82 describes its effect through mixing different Rydberg levels, it begins to represent application of the effective potential in "second-order" within the space of Rydberg levels. It is useful to consider whether other terms in the effective potential could also have significant effects of this type.

The simplest example of this is the shift caused by application of the leading scalar term in V_{eff} proportional to the adiabatic scalar dipole polarizability $\alpha_{D,0}$. This was considered by Drachman in his treatment of the case of helium Rydberg levels $(J_c = 0)$. He showed that the lowest multipole term in the fourth-order perturbation energy containing an intermediate Rydberg level corresponded, after making the adiabatic approximation to the two other energy denominators, to application of the $\alpha_{D,0}$ term in second-order, giving the result

$$E^{[4]}\left(nL_K\right) = -\sum_{n'} \frac{\left\langle \left(gJ_c\right) nL_K \left| -\frac{1}{2}\frac{\alpha_{D,0}}{r^4} \right| \left(gJ_c\right) n'L_K \right\rangle^2}{E\left(n'\right) - E\left(n\right)} + \cdots . \tag{2.86}$$

This led to a significant shift of the energy levels in helium [12]. The shift is a universal function of $\left(n, L\right)$ and $\alpha_{D,0}$, and it was later evaluated analytically by Drake and Swainson [25].

In considering the more general case of $J_c \geq 0$, the leading terms in the effective potential have the form

$$V_{eff} \approx -\frac{1}{2}\frac{\alpha_{D,0}}{r^4} - \left(\frac{Q}{r^3} + \frac{1}{2}\frac{\alpha_{D,2}}{r^4}\right) \frac{X^{[2]}\left(J_c\right) \cdot C^{[2]}\left(\hat{r}\right)}{\begin{pmatrix} J_c & 2 & J_c \\ -J_c & 0 & J_c \end{pmatrix}} . \tag{2.87}$$

The terms proportional to the scalar and tensor dipole polarizabilities also have the potential to mix different Rydberg series and produce energy shifts to a particular level. These energy shifts occur formally as parts of the third- and fourth-order perturbation in *V*. They are likely the largest contributions from third- and fourth-order perturbation since they include contributions of one intermediate state where the core is not electronically excited. Terms proportional to $Q\alpha$ occur in the third-order perturbation energy while terms proportional to $\alpha\alpha$ occur in the fourth-order perturbation energy. Both types of terms include one Rydberg intermediate level (denoted $\left(gJ_c'\right) n'L_K'$ in Eq. 2.88) and contain the factor

$$\sum_{\lambda'', J_c'', n'', L''} \frac{\left\langle \left(gJ_c\right) nL_K \left| M^{[1]} \cdot \frac{C^{[1]}\left(\hat{r}\right)}{r^2} \right| \left(\lambda'' J_c''\right) n''L_K'' \right\rangle \left\langle \left(\lambda'' J_c''\right) n''L_K'' \left| M^{[1]} \cdot \frac{C^{[1]}\left(\hat{r}\right)}{r^2} \right| \left(gJ_c'\right) n'L_K' \right\rangle}{\Delta E\left(\lambda'' J_c''\right)} , \tag{2.88}$$

which can be shown to be equal to

$$\left\langle (gJ_c)nL_K \left| \frac{1}{2}\frac{\alpha_{D,0}}{r^4} + \frac{1}{2}\frac{\alpha_{D,2}(J_c')}{r^4}\frac{X^{[2]}(J_c)\cdot C^{[2]}(\hat{r})}{\begin{pmatrix} J_c & 2 & J_c \\ -J_c & 0 & J_c \end{pmatrix}} \right| (gJ_c')n'L_K' \right\rangle, \tag{2.89}$$

where the reduced matrix elements of $X^{[2]}(J_c)$, both diagonal and off-diagonal in J_c, are equal to 1. The coefficient $\alpha_{D,0}$ is the usual scalar dipole polarizability, given in Section 2.2B, and the term proportional to it satisfies the selection rules $\Delta J_c = \Delta L = 0$. The coefficient $\alpha_{D,2}(J_c')$ is given by the expression

$$\alpha_{D,2}(J_c') = 2\sqrt{\frac{10}{3}}\begin{pmatrix} J_c & 2 & J_c \\ -J_c & 0 & J_c \end{pmatrix}(-1)^{J_c'-J_c}\sum_{\lambda'',J_c''}(-1)^{2J_c''}\begin{Bmatrix} J_c'' & 1 & J_c \\ 2 & J_c' & 1 \end{Bmatrix}\frac{\left\langle gJ_c \left\| M^{[1]} \right\| \lambda'' J_c'' \right\rangle \left\langle \lambda_c'' J_c'' \left\| M^{[1]} \right\| gJ_c' \right\rangle}{\Delta E(\lambda'' J_c'')} \tag{2.90}$$

Note that this reduces to the result shown in Section 2.2B if $J_c' = J_c$, i.e. for terms diagonal in J_c, but it differs for nondiagonal terms. For example, if $J_c = 5/2$, there are contributions to $\alpha_{D,0}$ and $\alpha_{D,2}$ from branches with $J_c'' = 3/2$, 5/2, and 7/2, but an off-diagonal $\alpha_{D,2}$ coupling to levels with $J_c' = 3/2$ can have no contribution from the $J_c'' = 7/2$ branch. This restriction is enforced by the triangle relations on the 6J-symbol in Eq. 2.90. This term satisfies the same selection rules as the quadrupole term: $\Delta J_c = 0, \pm 1, \pm 2$, and $\Delta L = 0, \pm 2$.

This implies that the leading "second-order" effects of V_{eff} can be written as

$$E_{eff}^{[2]}(nL_K) = -\sum_{J_c',n',L}{}' \frac{\left\langle (gJ_c)nL_K \left| V_{eff} \right| (gJ_c')n'L_K' \right\rangle \left\langle (gJ_c')n'L_K' \left| V_{eff} \right| (gJ_c)nL_K \right\rangle}{\Delta E(gJ_c') + E(n') - E(n)}, \tag{2.91}$$

where

$$V_{eff} \approx -\frac{1}{2}\frac{\alpha_{D,0}}{r^4} - \left(\frac{Q(J_c')}{r^3} + \frac{1}{2}\frac{\alpha_{D,2}(J_c')}{r^4} \right) \frac{X^{[2]}(J_c)\cdot C^{[2]}(\hat{r})}{\begin{pmatrix} J_c & 2 & J_c \\ -J_c & 0 & J_c \end{pmatrix}}, \tag{2.92}$$

in which $\alpha_{D,2}(J_c')$ is given by Eq. 2.90 and

$$Q(J_c') = (-1)^{J_c'-J_c} \sqrt{\frac{2J_c'+1}{2J_c+1}} \frac{\begin{Bmatrix} S_c & L_c & J_c \\ 2 & J_c' & L_c \end{Bmatrix}}{\begin{Bmatrix} S_c & L_c & J_c \\ 2 & J_c & L_c \end{Bmatrix}} \left\langle gJ_c \left\| M^{[2]} \right\| gJ_c \right\rangle \begin{pmatrix} J_c & 2 & J_c \\ -J_c & 0 & J_c \end{pmatrix}, \tag{2.93}$$

where L_c and S_c are the assumed *L* and *S* values, respectively, for the core ground electronic state. This expression reduces to the usual quadrupole moment for diagonal terms and gives the result indicated by pure *LS* coupling for the off-diagonal quadrupole coupling.

When $E_{eff}^{[2]}$ (Eq. 2.91) is evaluated, it reduces to terms analogous to Eq. 2.84 while containing sums like Eq. 2.85 with (s, q) = (3,3), (3,4), and (4,4). The higher inverse powers generally correspond to smaller shifts, and examining the dependence of the calculated shift on the total inverse power can provide a clue to the probable precision of a result truncated with these terms. If necessary, higher terms in V_{eff} can also be included.

2.2D Spin and Relativistic Terms

There are several small additional terms not included in the nonrelativistic model described above. The first is the standard relativistic correction to the kinetic energy of a hydrogenic Rydberg electron, given by

$$E_{\text{rel}} = \frac{1}{2}\alpha_{FS}^2 \frac{Q^2}{n^4}\left(\frac{3}{4} - \frac{n}{L+\frac{1}{2}} \right), \tag{2.94}$$

where α_{FS} is the fine-structure constant. This term is due to the "p^4" contributions to the kinetic energy.

The next two terms describe the magnetic interaction between the Rydberg electron and the core ion's magnetic moments. The dominant effect is due to the magnetic dipole moment of the core, given by

$$E_{\text{CoreM1}} = \left\langle -\frac{1}{2}\alpha_{FS}^2 \frac{g_J}{r^3} \vec{L} \cdot \vec{J}_c \right\rangle, \tag{2.95}$$

where g_J is the core's g-value. This term is generally much larger than the electric vector terms discussed in Section 2.2B. Another possible magnetic interaction with the core ion is through its permanent magnetic octupole moment. An octupole moment could occur in any ion with $J_c \geq 3/2$ and thus contribute to the Rydberg fine structure through a term similar to the third-order tensor terms in V_{eff}. Here the term is simply parameterized as

$$E_{\text{CoreM3}} = \left\langle \frac{C_{\text{M3}}}{r^5} \left(X^{[3]}(J_c) \cdot T^{[3]}(\hat{r}) \right) \right\rangle, \tag{2.96}$$

where $T^{[3]}(\hat{r})$ is defined in Eq. 2.67.

An additional magnetic interaction is with the magnetic moment of the Rydberg electron, either through spin-orbit interaction from its own orbital motion or with the magnetic field from the core ion's magnetic moment. These are given by

$$E_{S_R} = \left\langle \frac{1}{2}\alpha_{FS}^2 \frac{1}{r^3} \left[\vec{L} \cdot \vec{S}_R + g_J \vec{J}_c \cdot (1 - 3\hat{r}\hat{r}) \cdot \vec{S}_R \right] \right\rangle, \tag{2.97}$$

where $\vec{S}_R$ is the Rydberg spin. This interaction splits the nL_K level into two states with $J = K \pm 1/2$. Rewriting this gives

$$E_{S_R} = \frac{1}{2}\alpha_{FS}^2 \left\langle r^{-3} \right\rangle_{nL} \left[Qa - g_J b \right] \vec{K} \cdot \vec{S}_R , \tag{2.98}$$

where

$$a = \frac{K(K+1) + L(L+1) - J_c(J_c+1)}{2K(K+1)} , \tag{2.98a}$$

$$b = \sqrt{15}\sqrt{2J_c(2J_c+1)(2J_c+2)}\sqrt{\frac{2L(2L+1)(2L+2)}{(2L-1)(2L+3)}}\sqrt{\frac{2K+1}{2K(2K+2)}}\begin{Bmatrix} J_c & J_c & 1 \\ L & L & 2 \\ K & K & 1 \end{Bmatrix}, \tag{2.98b}$$

and

$$\vec{K} \cdot \vec{S}_R = \frac{1}{2}\left[J(J+1) - K(K+1) - \tfrac{1}{2}\left(\tfrac{1}{2}+1\right) \right]. \tag{2.99}$$

All of these terms make only small contributions to the energy of a nonpenetrating Rydberg electron since such an electron is very nonrelativistic.

2.3 Discussion

The main application of the effective potential model is to provide a framework for extracting measurements of core ion properties from experimental measurements of high-L Rydberg fine structure patterns. A good example of this is a recent study of argon Rydberg levels [5]. In that study, the relative positions of twenty Rydberg levels within the $n = 10$ manifold with $5 \le L \le 9$ were measured with precision of better than 1 MHz. This pattern of level positions, which spanned a range of more than 25,000 MHz, could be expected to represent the expectation value of the effective potential generated by interactions with the Ar^+ core ion. More precisely, this would be the case except for the small level shifts represented by the relativistic corrections in Eq. 2.94 and the second-order effects of V_{eff} from Eq. 2.91. Calculation of $E_{eff}^{[2]}$, of course, requires some level of knowledge of the core parameters. Rough

values of the core parameters may be obtained by initially assuming that $E_{eff}^{[2]}$ is zero. Using these approximate numbers, $E_{eff}^{[2]}$ may be recalculated and then new values for the core properties found. The process is repeated until consistent. Table V of Ref. [5] shows the effect of these small corrections and the results once they are removed from the observed pattern. The calculated contributions of $E_{eff}^{[2]}$ are small and decrease smoothly with *L*, indicating that the influence of mixing between different Rydberg series is relatively minor.

Once the corrections were removed, the data pattern could be decomposed into the contributions of scalar, vector and tensor orders, defining the structure factors shown in Table VI of Ref. [5]: $A_0(L)$, $A_1(L)$, and $A_2(L)$. Note that since Ar^+ has a $^2P_{3/2}$ ground state, a third-order contribution to the structure is possible. A satisfactory fit of the data pattern, however, was obtained without including this term. The variation of the structure factors with *L* was then used, in combination with the form of the effective potential, to extract experimental estimates of the leading core properties. For example, the tensor structure factor $A_2(L)$ is expected to be dominated by a contribution proportional to $\langle r^{-3} \rangle_{nL}$, with smaller contributions proportional to $\langle r^{-4} \rangle_{nL}$ and perhaps $\langle r^{-6} \rangle_{nL}$. Thus scaling the measured $A_2(L)$ factors by $\langle r^{-3} \rangle_{nL}$ and plotting the ratio vs. $\langle r^{-4} \rangle_{nL} / \langle r^{-3} \rangle_{nL}$ leads to the plot shown in Fig. 7 of Ref. [5], from which core properties *Q* and $\alpha_{D,2}$ were both determined. A similar scaled plot of $A_1(L)$, Fig. 8 in Ref. [5], determined the g_J value of Ar^+ and the core property $\beta_{D,1}$. The A_0 plot is slightly more complicated since only the relative positions of the twenty levels were measured experimentally. Consequently, only differences of $A_0(L)$ factors are significant. Still, a plot of

$A_0(L+1)-A_0(L)$ scaled to the difference of expectation values of r^{-4} was used to determine $\alpha_{D,0}$ from the experimental measurements, and is shown in Fig. 9 of Ref. [5].

In all cases, the appearance of the scaled plots was completely consistent with the expectations based on the form of the effective potential. The precision of the core properties derived in this way is remarkable. The quadrupole moment, *Q*, was determined to 0.004% while the scalar polarizability, $\alpha_{D,0}$, was determined to 0.03%. Measurements of comparable properties of neutral atoms are difficult or impossible to obtain at this precision. Measurements of these ion properties pose a challenging test of even the most advanced theoretical methods. Confidence in the form of the effective potential is an important factor in analyzing such experimental measurements.

One limitation of the derivation presented in Section 2.2 is its reliance on the convergence of the adiabatic expansion. Recall that this is based on the dominance of the core excitation energy, $\Delta E(\lambda' J_c')$, in the denominator of the second-order perturbation energy as compared to the difference of Rydberg energies, $E(n')-E(n)$, that also occurs there. It is possible to predict the failure of this expansion in a particular case by using the properties of Rydberg electrons to estimate the typical value of the second quantity. Using the case where $\kappa_1=\kappa_2=1$ as an example, the "average" Rydberg energy difference can be estimated using Eqs. 2.20 and 2.21:

$$\begin{aligned}\left(E(n')-E(n)\right)_{AV} &\equiv \frac{\sum_{n'}\left(E(n')-E(n)\right)\left\langle nL\,|\,r^{-2}\,|\,n'L'\right\rangle^2}{\sum_{n'}\left\langle nL\,|\,r^{-2}\,|\,n'L'\right\rangle^2} \\ &= \frac{1}{2}\left(4-L(L+1)+L'(L'+1)\right)\frac{\left\langle r^{-6}\right\rangle_{nL}}{\left\langle r^{-4}\right\rangle_{nL}}\end{aligned}. \qquad (2.100)$$

If the ratio of this average Rydberg energy difference and the lowest core excitation is small, then the adiabatic expansion is likely to converge well. Take for example the $n = 10$ and $L = 6$ Rydberg level of a neutral Rydberg system. In this case the average Rydberg energy difference is +2897 cm^{-1} if $L' = 7$ and -1287 cm^{-1} if $L' = 5$. If the core ion is He^+, where the lowest dipole excitation is 329,179 cm^{-1}, or Ni^+ where the lowest dipole excitation is at 51,558 cm^{-1}, this suggests rapid convergence of successive terms of the adiabatic expansion. If the core ion is Sr^+, where the lowest dipole excitation is 14,556 cm^{-1}, convergence is likely to be less rapid. Of course, since the ratio of expectation values of r^{-6} and r^{-4} decreases rapidly with L, sufficiently high L Rydberg levels should show good convergence in most systems.

Fortunately, if a case of nonconvergence of the adiabatic expansion is encountered, the cause is often a single low-lying excited core level with a known position, and this suggests a fairly simple solution. The contribution to the second-order perturbation energy from intermediate states containing this single excited core level can be calculated separately and added to the expectation value of the effective potential describing the contributions of all other intermediate states. The calculated contribution from states containing the specific low-lying core level must be calculated individually for each Rydberg level of interest, and its dependence on n, L, and K may be very different from the form predicted by the effective potential. It is also usually known only up to a constant that represents the square of the matrix element coupling the core ground state to the low-lying state of interest. This constant can be treated as an additional parameter in matching observed fine structure patterns to the form predicted by the effective potential. This procedure was followed by Gallagher, Kachru, and Tran [10] and Snow and Lundeen [26] in their analysis of the barium Rydberg spectrum. In this case the offending low-lying level is the 5*d* level, which dominates the quadrupole polarization energies.

Another issue that has arisen in analysis of Rydberg spectra involves the problem of fitting the fine structure pattern's dependence on L to a sequence of inverse powers of r, as briefly described above. While the expectation value of each successive inverse power of r decreases smoothly with L, the variation between r^{-4} and r^{-6} or between r^{-6} and r^{-8} is much more dramatic than between r^{-6} and r^{-7}. It may be possible to fit the data pattern to a sum of contributions proportional to r^{-4}, r^{-6} and r^{-8}, but impossible to distinguish possible contributions proportional to r^{-7} or to the very similar $L(L+1)r^{-8}$. This problem is exacerbated by the possibility of an additional contribution proportional to r^{-7} coming from the lowest multipole adiabatic third-order perturbation energy which gives rise to a term proportional to a quantity "δ", discussed in Ref. [27]. This is most significant when it is desired to extract a reliable measurement of the coefficient of r^{-6} in the pattern of experimental energies, as in Si^{2+} [27] or Th^{3+} [28].

The effective potential derived here is similar to the potential derived by Clark, Greene, and Miecznik in the case of nondegenerate channels (their Eq. 20) [18]. Their potential contains terms only up to the inverse sixth power of the Rydberg radial coordinate, and all of their adiabatic terms agree with the ones presented here. Their nonadiabatic terms, however, differ slightly from the analogous results shown here. The potential of their Eq. 20 represents the simplest form of their description of high-L Rydberg spectroscopy. Still, by numerically finding the eigenvalues in that potential, one would already include some terms which in the formulation derived here would be included in $E_{eff}^{[2]}$, i.e. the effects of mixing between Rydberg levels of the same L but different n all coupled to the ground state of the ion core. Clark, Greene, and Miecznik continue by describing more complex formalisms in which the coupling to other

channels corresponding to different values of L and perhaps J_c, but the same value of K, are also included prior to numerical solution of the eigenvalue problem. Without a doubt, a calculation based on these more complex formalisms should be more successful in describing the structure of Rydberg levels where coupling between different Rydberg series is significant. Whether this is necessary to describe a particular Rydberg system will depend on the details of the Rydberg core interactions.

One interesting feature of the effective potential is the presence of odd-order tensor interactions, both vector and third-order. The vector terms in high-L Rydberg structure have an extensive history. The first clear observation of such effects occurred in a study of high-L Rydberg states of barium by Gallagher, Kachru, and Tran [10]. In this case the core ion was a $^2S_{1/2}$ state, and large splittings were observed between the two possible values of $K = L \pm ½$. The observed splittings were much larger than could be accounted for by the expected magnetic interactions. Some years later, stimulated by related, but much smaller anomalies in the structure of high-L Rydberg levels of Si^{2+}, these vector splittings were explained as an indirect effect of the spin-orbit splittings in excited ^2P levels of Ba^+ [29]. These indirect spin-orbit splittings, or K-splittings as they were also called, were later exploited to extract precise measurements of dipole and quadrupole transition strengths in Ba^+ [30, 31, 32]. In the meantime, an apparently different type of vector splitting was predicted by Zygelman [21] using a Berry phase argument. This splitting was thought to be limited to cases where the core ion had nonzero orbital angular momentum. It was later rederived and calculated more definitively by Clark, Greene, and Miecznik [18], who coined the name "vector hyperpolarizability" to describe it. This is precisely the term represented in Eq. 2.48 in Section 2.2B that is proportional to the coefficient $\beta_{D,1}$. Experimental measurements first in neon [4] and later in argon [5] displayed contributions of this

type, vector terms proportional to r^{-6}, and confirmed the coefficient calculated by Clark, Greene, and Miecznik [18]. The argon measurements also suggested that higher-order terms proportional to r^{-8} might be present, as is now predicted by Eq. 2.48 in Section 2.2B. These two types of vector interactions, indirect spin-orbit and vector hyperpolarizability, showed many superficial similarities. They were both proportional to $\vec{L} \cdot \vec{J}_c$ and r^{-6} in lowest order, and both were traced to nonadiabatic response of the core to the Rydberg electron. However, the vector hyperpolarizability was thought to require a nonzero core angular momentum, and would therefore be absent in the barium Rydberg states. In fact they are both described by Eq. 2.48 of Section 2.2B. When the coefficients $\beta_{D,1}$ and $\beta_{Q,1}$ are evaluated for the case of a $^2S_{1/2}$ core ion, they reproduce the results given in Eqs. 15 and 22 of Ref. [29]. Note that for this case, both coefficients would be zero in the absence of spin-orbit splittings in the excited states of the core, as emphasized by the appearance of Eqs. 15 and 22 of Ref. [29]. Yet, the two effects, thought to be quite different, are truly aspects of the same physical effect.

Another issue is the completely nonrelativistic derivation of the effective potential. One may question whether it is reasonable to expect that the calculation based on a completely nonrelativistic Hamiltonian will describe Rydberg levels in a system where the core ion's nuclear charge is large, thus making the core electrons relativistic even if the Rydberg electron is nonrelativistic. In the absence of a fully relativistic calculation describing the complete Rydberg system, there is no way to answer this question definitively. However, it seems plausible that the physical properties of the core, polarizabilities and permanent moments, would exist even for a highly relativistic core ion, and would interact in a similar way with the nonrelativistic Rydberg electron. These properties, of course, could never be accurately calculated within the nonrelativistic model used in this report, but would instead require much more sophisticated

relativistic formulations of atomic structure theory. There is some circumstantial evidence to suggest that the form of the potential is correct even if the core ion is highly relativistic and that it is still correct to use the form of the potential to interpret the spectroscopy of nonpenetrating Rydberg electrons to extract core properties, even of highly relativistic positive ions. The strongest evidence along these lines is the agreement between the dipole polarizabilities of Pb^{2+} and Pb^{4+} extracted from spectroscopy of high-L Rydberg levels of PbII and PbIV [33] and the calculated values obtained using relativistic many-body perturbation theory [34]. The experimental values were 13.62(8) and 3.61(4) a.u. [33] and the calculated values were 13.30 and 3.63 a.u. [34]. There is, as yet, no comparable comparison for Rydberg states bound to highly relativistic core ions with nonzero orbital angular momentum.

Note: The majority of this chapter has been published as

Shannon L. Woods and S. R. Lundeen, Phys. Rev. A **85**, 042505 (2012)

Chapter 3: RESIS Experimental Apparatus

3.1 Introduction

Determination of the core parameters presented in the previous chapter can be accomplished by precise measurement of the Rydberg fine structure patterns. The Resonant Excitation Stark Ionization Spectroscopy (RESIS) technique can provide such measurements. Figure 3.1 shows a schematic of the experimental setup.

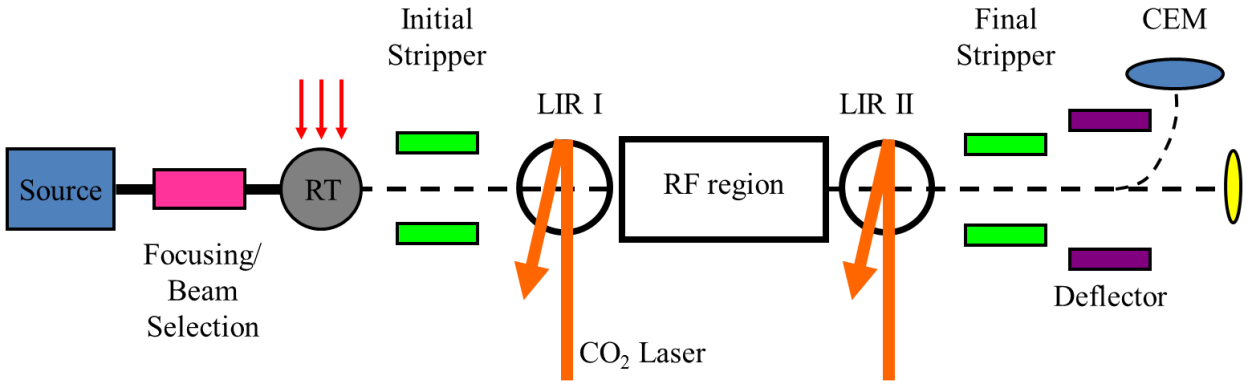

Figure 3.1: Experimental apparatus schematic for the microwave RESIS technique. It begins with the ion beam source on the left. The beam then enters the focusing/beam selection region which uses a $\vec{v} \times \vec{B}$ filter to steer the desired type of ion down the rest of the beamline. The ions capture a Rydberg electron from the Rydberg target (RT), which consists of a thermal plume of Rb step-wise excited by three diode lasers. At the initial stripper all Rydberg atoms with $n > 15$ are Stark ionized and deflected, along with any remaining ions. Both laser interaction regions (LIRs) are set to excite the Rydberg electron from a lower n to a higher n' (ex: 9→19 or 10→30), while the RF region excites a transition within the lower n. In the detector, the final stripper Stark ionizes states with the upper n' which are then deflected into the channel electron multiplier (CEM).

Section 3.2 discusses the creation of the ion beam, along with the focusing and beam selection. Section 3.3 describes the Rb Rydberg target, followed by the section detailing the initial stripper. Section 3.5 explains the excitation in the optical RESIS technique, while Section 3.6 describes the detection. The microwave RESIS technique is discussed in the section 3.7.

3.2 Ion Beam Creation and Selection

The RF ion source produces Ni^+ ions by sputtering from a solid nickel target. The ions are extracted and then accelerated to approximately 9500 V. The ions are then focused using a lens system and mass-separated using a $\vec{v} \times \vec{B}$ filter. The RF ion source was manufactured by Beam Imagining Solutions while the lens system and $\vec{v} \times \vec{B}$ filter were manufactured by Colutron Corporation. The source is shown in the following picture.

Figure 3.2: Picture of the RF ion source showing the gas isolator, RF coil, and discharge chamber. For scale, the horizontal length of what is shown is around 5".

The electrical connections of the source and the $\vec{v} \times \vec{B}$ filter are shown in Fig. 3.3, which also notes the metal sputter target inside the source discharge chamber. To operate the source, a working gas is sent through the discharge chamber and power is applied to the RF coil. An RF power generator and matching network are used to excite the RF coil. When power is first applied to the RF coil, the load and tune capacitors of the matching network are adjusted to reduce the reflected power to 0 W. According to Ref. [35] the source is primarily operated in the inductively coupled plasma (ICP) mode. The time-varying magnetic field around the RF coil,

due to the time-varying electric current flowing through it, induces electric currents in the gas which lead to a plasma. The need to once again readjust the load and tune capacitors to reduce the reflected power is a sign that the source has started in the ICP mode.

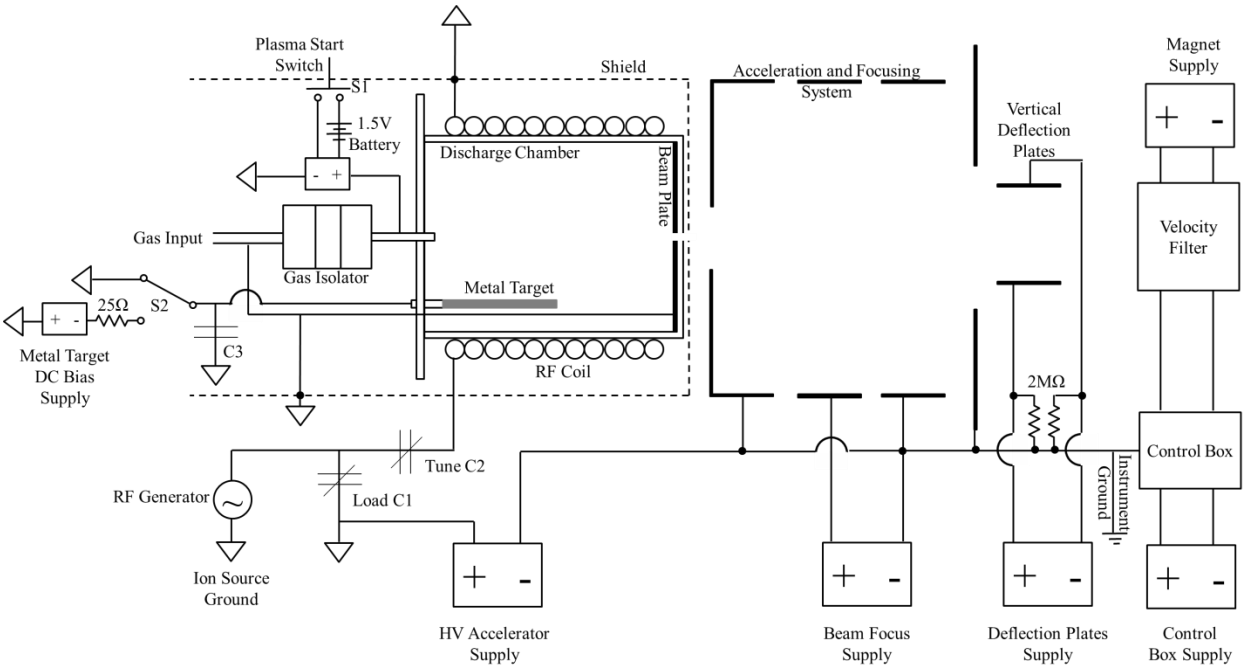

Figure 3.3: Electrical connections of the source and $\vec{v} \times \vec{B}$ filter. Note that this diagram is not to scale.

A typical day would begin by pumping the system down to a pressure of high 10^{-7} T, as measured downstream of the source discharge chamber in the region of the $\vec{v} \times \vec{B}$ filter. The system is then flushed with argon for ten minutes at a pressure of low 10^{-4} T. During this time, the acceleration voltage is turned up to 9500 V and the RF source water cooling turned on. Note that a large acceleration current before the RF power is turned on might mean that the cooling water needs to be replaced with fresh distilled water. The RF forward power is then raised to ~ 160 W and the tune and load capacitors are adjusted to reduce the reflected power to 0 W. If one is unable to lower the reflected power, one should first check that everything is connected properly. If the source has just been reinstalled, it may also indicate that there is something wrong with the RF coil. For example, it may be that the RF coil is touching the outer shielding

or itself, requiring removal of the source and repositioning of the RF coil. Once the reflected power has been lowered, it is now time to get the source "started". Usually this involves raising the RF power to 300 W for a few seconds before lowering it back to 160 W. Note that keeping the RF power too high for too long can cause, for example, the nickel sputter target to deform and possibly block the gas inlet tube. The main indicators that the source has started are that the reflected power and acceleration current suddenly increase. The next step is to reduce the reflected power to 0 W using the tune and load capacitors, while also lowering the forward power to the typical running condition of ~ 100 W. Changing the tune and load capacitors or the forward power too quickly can cause the source to "unlight".

The entire process typically took a minimum of ten minutes, although there are many reasons why it may take longer. The source start time usually got longer as the source got "dirtier" from repeated sputtering of nickel or if the gas inlet was starting to clog. At this point, one can try increasing the pressure to help get the source started. Note that increasing the pressure too high can cause the accelerator to arc. If the source does not start after a day or two of trying, it may be necessary to uninstall it and clean both the source chamber and the gas inlet tube.

Once the source has successfully started, the pressure is usually reduced to high 10^{-5} T in order to maximize the argon beam. Typical argon beam sizes at the end of the beamline (note that there are various apertures along the way) were 300-500 nA. The next step is to turn the sputter bias up to some low voltage, around -30 V, for about ten minutes in order to sputter off any oxide layers on the sputter target. The sputter bias is then increased to around -60 V. On a good day, the nickel beam would be ~ 20 nA. A low beam current may indicate that the sputter target is mostly gone. One can temporarily extend the life of the sputter target by increasing the

RF power or the sputter bias voltage, but again this may deform the sputter target until it is blocking the gas inlet. If the source is unstable, it may indicate either that the pressure is too low or that the source chamber is getting coated with the sputter material and needs to be cleaned.

After the RF ion source is the focusing lens and the $\vec{v} \times \vec{B}$ filter system. They are used to select and focus the desired beam such that it intersects the Rydberg target (Section 3.3) and goes through any downstream apertures (such as the initial stripper discussed in Section 3.4). Typical operation of the $\vec{v} \times \vec{B}$ filter involved setting the electric field voltage to a specific value and scanning through the voltage on the magnet's power supply in order to select either argon or nickel. Figure 3.4 shows a scan of the beam current, measured at the end of the beamline, versus "V_{mag}".

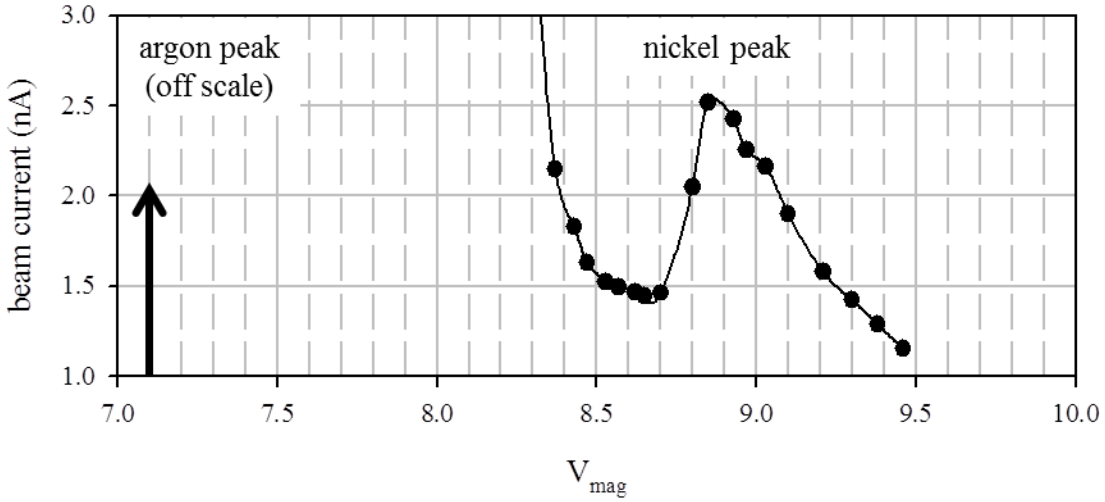

Figure 3.4: Scan of the magnet voltage (V_{mag}) versus beam current as measured at the end of the beamline. The nickel beam current peak is clearly visible at V_{mag}~8.85 and distinguishable from the argon peak at V_{mag}~7.1 (not shown). (Taken from SW03_135.)

In this figure, the nickel beam current peak is clearly visible in spite of being more than a hundred times smaller than the nearby argon beam at V_{mag}~7.1 (not shown). Not resolved in this particular V_{mag} scan is the fact that nickel is made up primarily of two isotopes: ^{58}Ni at 68% and

^{60}Ni at 26%. For the optical RESIS technique (Section 3.5), knowledge of which isotope is being excited is critical because this determines the calculated speed of the beam and thus the excitation energy.

There are two basic ways to separate isotopes produced by the ion source. The first is to use the $\vec{v} \times \vec{B}$ filter to increase the angular separation between the isotopes such that only one will be directed down the beamline. This can be done by increasing the electric field, thus increasing the magnetic field needed. Since the ratio of the magnetic fields for two masses goes roughly like the square-root of the masses

$$\frac{B_{Ni^{60}}}{B_{Ni^{58}}} \sim \sqrt{\frac{m_{Ni^{60}}}{m_{Ni^{58}}}} \sim 1.017 \tag{3.1}$$

the separation between masses is also increased. One limitation to this method is the size of electric and magnetic fields that can be used in the $\vec{v} \times \vec{B}$ filter, so it may be that the largest electric field does not lead to a separation in magnetic fields that is easily measured. This also means that heavier ions cannot be steered down the beamline at large electric fields, which can be inconvenient if one needs quick access to such an ion since different electric fields require different focusing settings. Another option for separating isotopes is to place a slit in the beamline to physically stop a particular isotope from reaching the detector. The drawback to this method is that imperfect focusing and alignment can also reduce the amount of the desired isotope that reaches the detector.

Fortunately for the microwave RESIS technique (Section 3.7) the mass difference between ^{58}Ni and ^{60}Ni does not present a problem. Although the different masses will result in different Doppler-shifts, this will be averaged out because each transition is measured in both co- and counter-propagating directions. It would slightly affect the analysis of the measurements,

discussed in Chapter 4, since the calculated expectation values of the Rydberg electron's radial coordinate in the effective potential model has a mass dependence. It can be shown, however, that this effect makes a difference at the kHz level and is thus not large enough to be measured.

3.3 Rydberg State Formation

Once the ion beam has been mass-selected, it captures an electron from the Rydberg target and passes through the initial stripper where ions that have not captured an electron are deflected, and neutral Rydberg atoms with $n \geq 15$ are ionized and then deflected. The Rydberg target consists of a thermal plume of rubidium step-wise excited by three diode lasers, all around 10 mW, to the 9*F* state. The excitation scheme in Fig. 3.5 shows the three exciting lasers at 780.24 nm (L1), 1529.3 nm (L2), and 770 nm (L3). The diagram in Fig. 3.6 shows the paths that the lasers take to the target. L1 and L2 are co-aligned before being sent into a cell of Rb, where a photodiode monitors the fluorescence. The output voltage of the photodiode is sent to an oscilloscope, where a clear peak can be seen when L1 and L2 are on resonance with their transitions, thus allowing both to be set before entering the target region. L3 is sent into the target region such that all three lasers intersect at a point in the Rb plume. Although L3 excites up to the 9*F* state, its population is in fact shared through a mirrorless maser transition with the 10*D* level lying just below it [36]. The fluorescence from the transition between the 10*D* and 5*P* states results in a blue-green glow that can be easily seen by eye. For more precise tuning, the "blue" is monitored using a phototube. Note that the amount of blue fluorescence depends on the amount of rubidium along with the alignment of the diode lasers, both with each other and with respect to the rubidium plume.

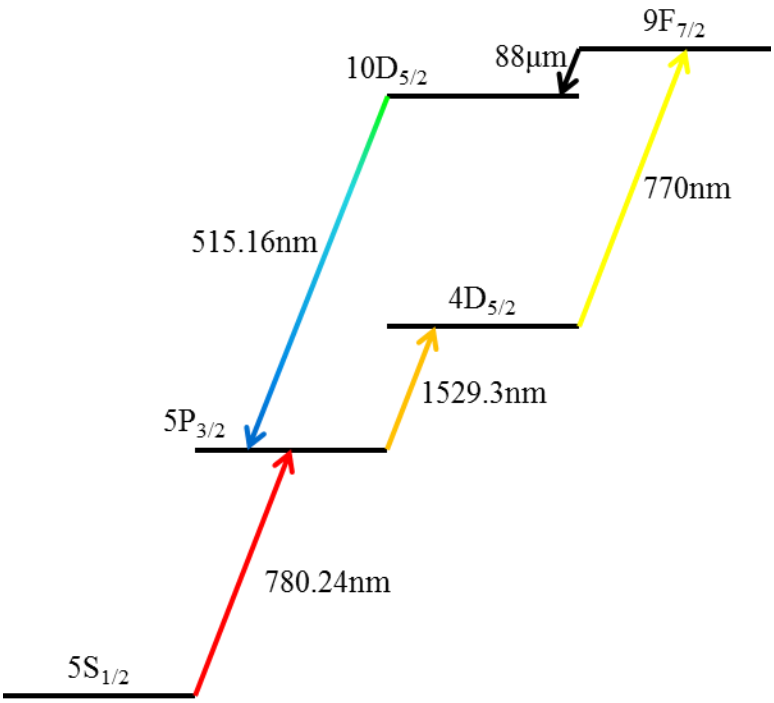

Figure 3.5: Rb excitation scheme showing the three exciting lasers at 780.24 nm (L1), 1529.3 nm (L2), and 770 nm (L3). A mirrorless maser transition transfers population from the 9*F* state to the 10*D* state at approximately 88 μm. The blue fluorescence from the 10*D* state to the 5*P* state is monitored using a phototube.

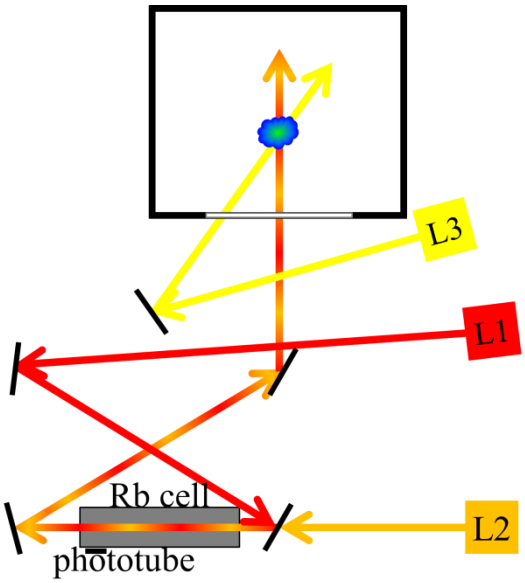

Figure 3.6: Rb excitation optics schematic with three excitation lasers (L1, L2, L3). L1 and L2 are aligned and sent through a Rb cell, where a phototube monitors the fluorescence of the two-step excitation. They are then sent through a window, along with L3, where they intersect a thermal Rb plume. When the lasers are properly aligned and on-resonance with their respective transitions, a blue-green fluorescence can be seen.

3.4 Initial Stripper

After passing through the Rydberg target, the beam of ions and neutral Rydberg atoms then enter the region of the initial stripper. The purpose of the initial stripper is essentially to reduce the background measured in the detector. One way it does this is by removing from the beam any ions that did not capture an electron from the target, thus reducing the possibility of Rydberg state formation through means outside the target region. The other is to ionize any neutral atoms with very high *n*, since those states would be ionized in the detector. The initial stripper (or pre-ionizer), shown in Fig. 3.7, is located within a Conflat-cross, approximately 20 cm away from the Rydberg target.

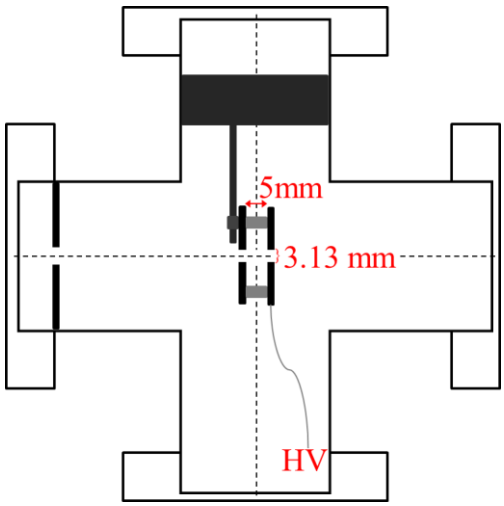

Figure 3.7: Initial stripper with plates separated by 5 mm, where the upstream plate (left) is grounded and the downstream plate (right) is held at a high voltage (HV).

It consists of two plates separated by 5 mm with apertures 3.13 mm in diameter for the beam to pass through. The upstream plate is held at ground while the other plate is held at 10 kV, which is large enough to repel any ions, either those left in the primary beam or those ionized by the initial stripper. The electric field required to ionize the states of a given *n* and *Q* depends on the

energy of the Stark state and how rapidly the atom or ion enters the field, and is approximately given by [37]

$$\frac{1}{9}\frac{Q^3}{n^4} * 5.14 * 10^9 \, {}^{V}\!/_{cm} \le F_{\substack{\text{stripper} \\ \text{ionization}}} \le \frac{2}{9}\frac{Q^3}{n^4} * 5.14 * 10^9 \, {}^{V}\!/_{cm}. \tag{3.2}$$

The resulting field in the initial stripper of 20 kV/cm is large enough to ionize any states of $n > 15$. There is an additional plate between the Rydberg target and the initial stripper, with a hole of diameter ~ 3.65 mm; it is used to prevent the rubidium from coating the initial stripper.

3.5 Optical RESIS Technique

In the optical RESIS technique, the Rydberg atoms are excited by a CO_2 laser beam in a Laser Interaction Region (LIR), Stark ionized in the final stripper, and then deflected into a channel electron multiplier to be detected. Figure 3.8 shows a simulated nickel spectrum, which spans two CO_2 laser lines and includes two transitions. The LIR is set to excite a transition between a low n, such as $n = 9$, and a high n, such as $n' = 19$ or 20. Although transitions with $\Delta L = L' - L = \pm 1$ and $\Delta K = K' - K = 0, \pm 1$ are possible, the dominant transitions are when $\Delta L = \Delta K = +1$.

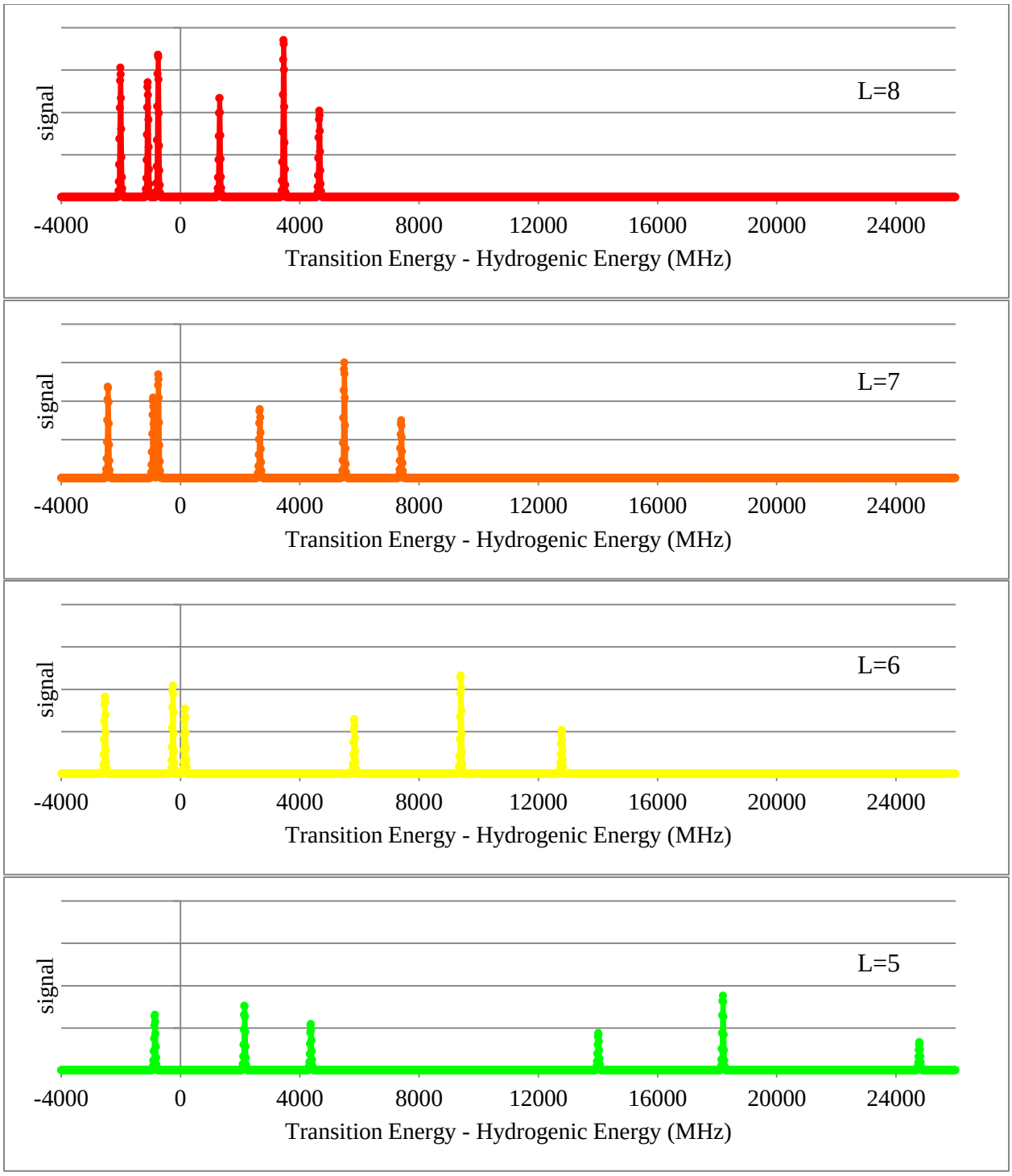

Figure 3.8: Simulated Ni optical spectrum showing $n = 9$ to $n' = 19$ and 20 for individual Ls. The signal (y-axis) has arbitrary units, although the signal heights have been weighted by $(2K+1)(2L+1)$ to roughly reflect the relative signal sizes that one would expect to see. The dividing line between the two transitions is around 4000 MHz.

First, a CO_2 laser beam enters the LIR and initially intersects the atom beam at approximately 90°, before reflecting off a mirror at an angle controlled by the stage (θ_s). The reading of θ_S when the reflected laser intersects the atom beam at exactly 90° is labeled $\theta_\perp$.

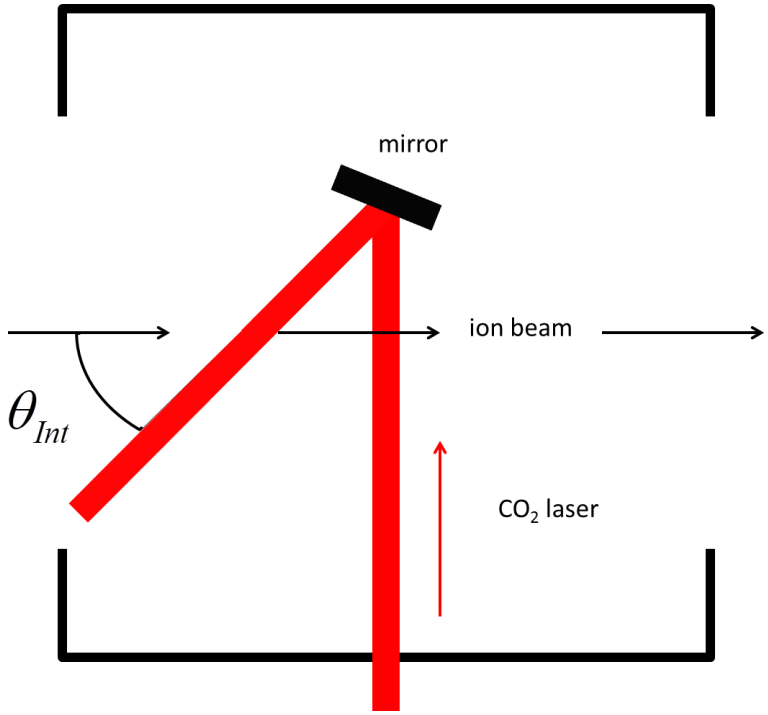

Figure 3.9: LIR angle diagram showing the ion beam moving to the right. The CO_2 laser beam enters from the bottom, initially intersecting the ion beam at an approximate right angle, before reflecting off a stage-controlled mirror and intersecting the ion beam again at what is referred to as θ_{Int}.

Knowing these two angles, along with the laser frequency ν_L and β, the ratio between the velocity v and the speed of light c, the laser frequency as seen by the Rydberg atom can be calculated with the following:

$$\nu_L' = \frac{\nu_L}{\sqrt{1-\beta^2}}\left[1+\beta\cos\left(\theta_{Int}\right)\right] = \frac{\nu_L}{\sqrt{1-\beta^2}}\left[1+\beta\sin\left(2\theta_s - 2\theta_\perp\right)\right], \tag{3.3}$$

where

$$\theta_{Int} = 90^\circ - 2\left(\theta_s - \theta_\perp\right). \tag{3.4}$$

A precise determination of ν_L' would require determining both β and $\theta_\perp$ precisely, as has been done previously [38], by making measurements of another atom with known core properties. The β of the calibration atom and $\theta_\perp$ could then be extracted, and the β of the atom of interest found by knowing the square root of the mass ratio between the two atoms. As the focus of this dissertation is measurements made using the microwave RESIS technique, which do not require knowing either β or $\theta_\perp$ exactly, the details of such a calibration will not be presented here.

One constraint of the LIR setup is the range of angles that can be scanned. In practice, the maximum $|\theta_s - \theta_\perp|$ is less than 30°, meaning that the range of frequencies for a particular laser line is approximately

$$|\nu_L' - \nu_L| < 0.9\beta\nu_L . \tag{3.5}$$

For the case of Ni^+, with $\beta_{Ni} \approx 0.00056$, the tuning range is less than 0.1% of a particular CO_2 laser frequency. Given that the frequencies are on the order of 1000 cm^{-1} and spaced more than 1 cm^{-1} apart, some frequencies are unavailable. As such, it may be necessary to look at more than one $n \rightarrow n'$ transition in order to optically map the entire Rydberg fine structure pattern.

Another point of concern is the width of the transition signal. A lower limit is placed on it by the transit time through the CO_2 laser, which is given by

$$T_{CO_2} = \frac{w_0}{c\beta \sin\theta_{Int}} , \tag{3.6}$$

where w_0 is the waist of the Gaussian laser beam and has a value of 2.25 mm for the Ultra Lasertech PX2500G CO_2 laser system used in this experiment. The full-width half-maximum (FWHM) of the transition can then be calculated using

$$\Delta\nu_{transit} = \frac{\sqrt{2\ln 2}}{\pi}\frac{1}{T_{CO_2}} = 0.375\frac{c\beta\sin\theta_{Int}}{w_0} \sim 29\ \text{MHz} . \tag{3.7}$$

Equating this to the derivative of Eqn. 3.3 with respect to angle and then solving for $\Delta\theta$ gives a minimum linewidth (in θ_s):

$$\Delta\theta_s\left(\text{in rad}\right) \geq \frac{0.375}{2}\frac{c}{w_o \nu_L}, \tag{3.8}$$

which can be rewritten as

$$\Delta\theta_s\left(\text{in deg}\right) \geq \frac{1}{2}\frac{214.86}{w_o\left(\text{in mm}\right)\nu_L\left(\text{in cm}^{-1}\right)} \sim 0.044°$$

using more convenient units.

Figure 3.10 is a typical optical scan. It shows the $9L_{7.5}$-$19M_{8.5}$ and $9K_{6.5}$-$19L_{7.5}$ peaks, along with the degenerate $9L_{9.5}$-$19M_{10.5}$ and $9K_{8.5}$-$19L_{9.5}$ peak.

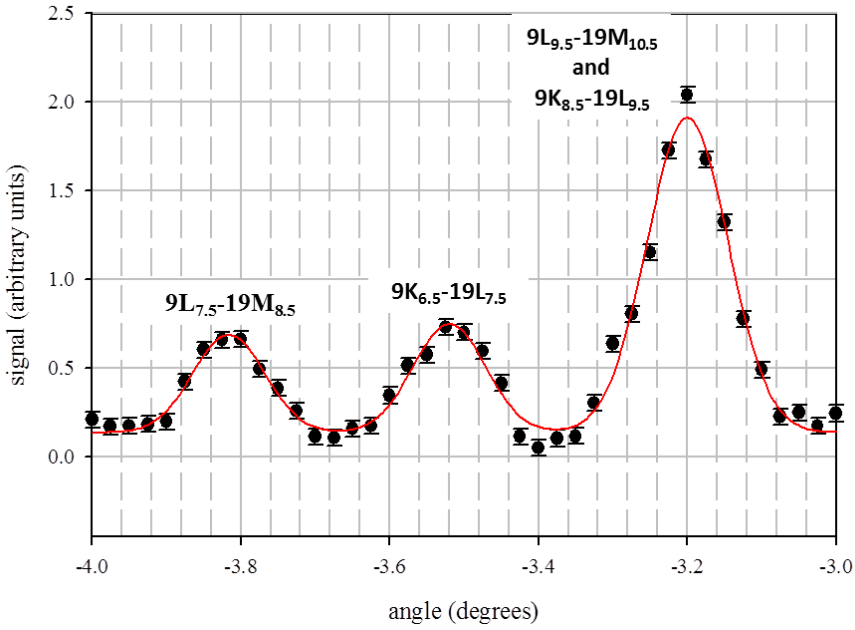

Figure 3.10: A typical Ni optical scan in LIR I showing the $9L_{7.5}$-$19M_{8.5}$ and $9K_{6.5}$-$19L_{7.5}$ peaks, along with the degenerate $9L_{9.5}$-$19M_{10.5}$ and $9K_{8.5}$-$19L_{9.5}$ peak. Each peak has been fit to a Gaussian. The tuning rate for this measurement is between 500 and 600 MHz per degree stage. (Taken from SW06_121)

Note that if a signal is fit to a Gaussian of the form

$$y_0 + ae^{-\frac{1}{2}\left(\frac{\theta-\theta_0}{b}\right)^2},$$

then the FWHM is related to *b* by

$$b = \frac{FWHM}{2.35}.$$

The two peaks on the left have a FWHM of approximately 0.11° while the double peak on the right is slightly larger at 0.13°. Each of these, however, is larger than the estimated minimum FWHM of 0.044° mentioned above. This is most likely due to the angular spread of the ion beam.

3.6 Detection

Once the Rydberg electron has been excited, it then moves into the detector where states with high *n* are Stark ionized and deflected into a channel electron multiplier (CEM). The beam passes through both a "short-gap stripper" and a "long-gap stripper". Each final stripper consists of two plates with an aperture in the center for the beam to go through. The plates of the "short-gap stripper" have a separation of 0.8 cm between them. Typically a potential of 5250 V was applied, sufficient enough to ionize states with $n \geq 19$. The "long-gap stripper", with a separation of 2.5 cm and a potential of 3000 V, was used when looking at the Ar electric field diagnostic transition with $n = 10$ to $n' = 30$, discussed later in Chapter 4. Ions formed by Stark ionization in either stripper are effectively energy tagged by an increase (or decrease in the case of a negative potential) in kinetic energy, thus distinguishing them from other ions in the beam since they would require different deflection potentials into the CEM. A lock-in amplifier monitors the current in the CEM synchronous with the chopping of the CO_2 laser.

3.7 Microwave RESIS Technique

The microwave RESIS technique consists of two LIRs separated by an RF region. Figure 3.11 shows a schematic of the RF region used in the study of nickel. It consists of an

inner conductor cylinder with diameter 0.246" (d) inside an outer conductor cylinder of diameter 1.290" (D). Knowing that the centers of the conductors are separated by 0.465" (c) allows one to calculate the impedance *Z* using [39]

$$Z = 60\cosh^{-1}(u)\ \Omega, \tag{3.9}$$

where

$$u = \frac{1}{2}\left(\frac{D}{d} + \frac{d}{D} - \frac{4c^2}{dD}\right), \tag{3.10}$$

to find a value of $Z = 49.14\ \Omega$.

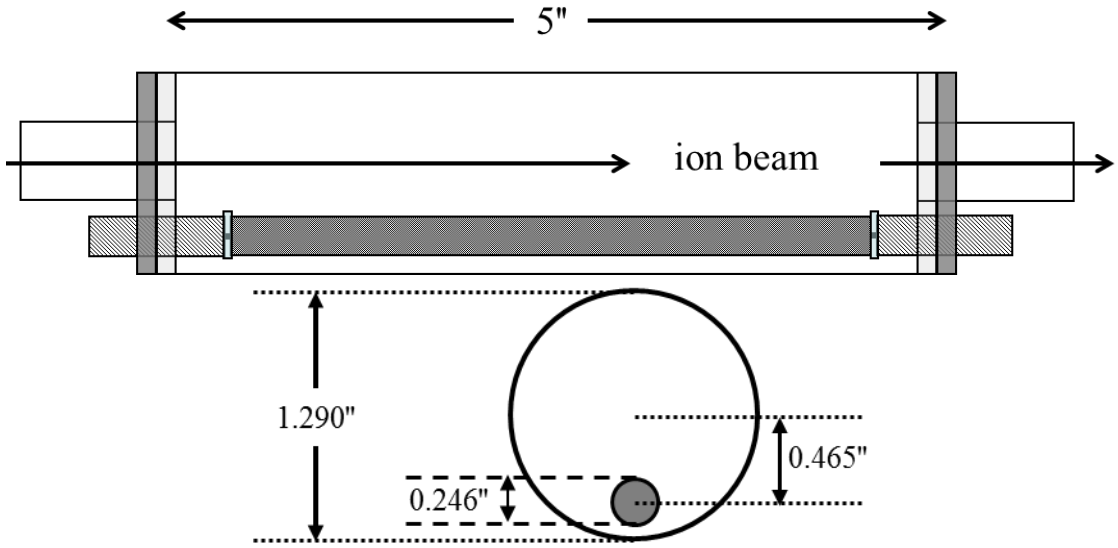

Figure 3.11: RF region diagram giving its basic appearance (top) and showing the dimensions of the inner and outer conductors (bottom).

The first step in setting up for an RF measurement is to set LIR I and LIR II to excite the proper transitions; typically the LIRs are set to the same transition. An example transition with $9K_{4.5}$ to $20L_{5.5}$ is shown below with the LIR I scan on the top and the LIR II scan on the bottom. It is assumed that transitions are saturated.

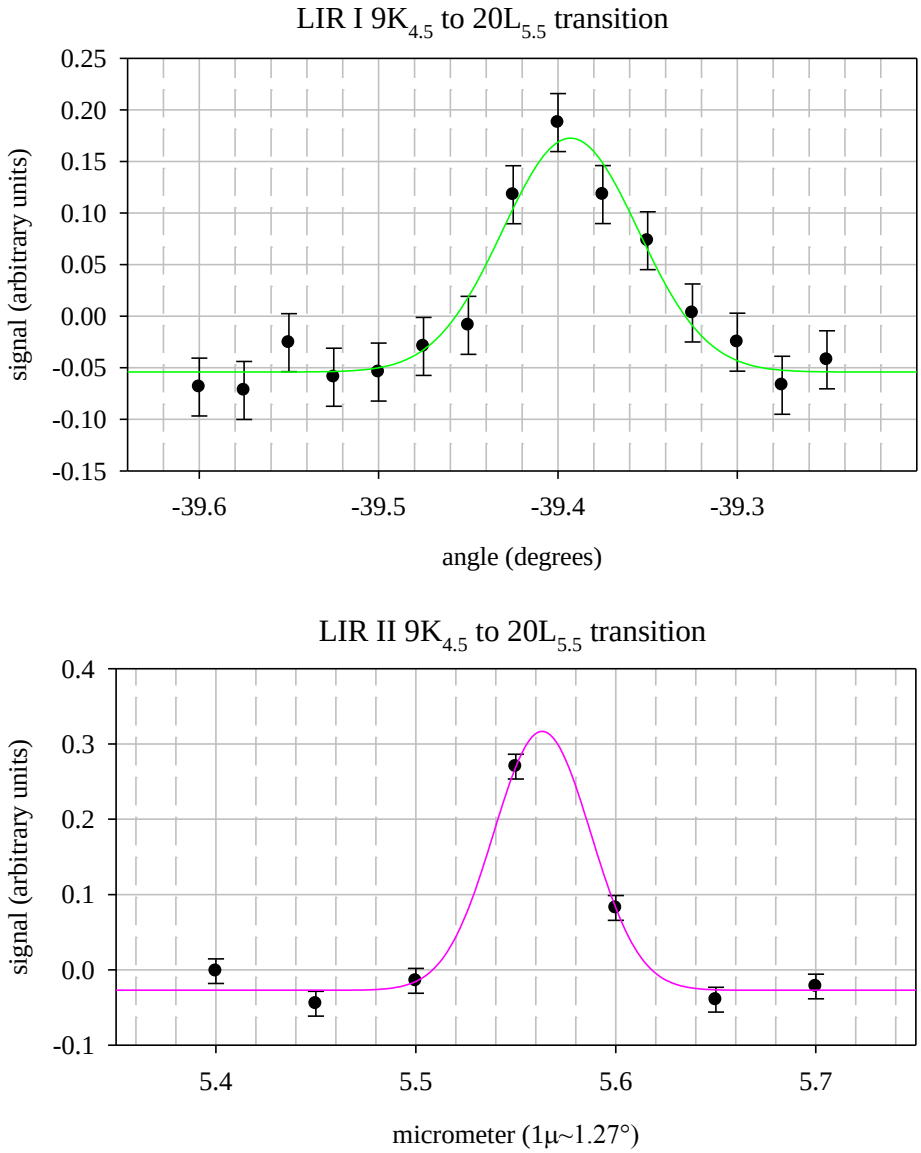

Figure 3.12: Scans of the Ni $9K_{4.5}$ to $20L_{5.5}$ transition in LIR I and II. Each peak has been fit to a Gaussian. LIR I: θ_s = -39.393(3)° and b = 0.038(3)°. LIR II: μ_s = 5.563(5) and b = 0.024(6) ~ 0.031°. Note that the LIR I signal (top) is taken from SW03_075 while the LIR II signal (bottom) is taken from SW03_076. Also, LIR II is controlled by a micrometer stage where 1 micrometer is approximately 1.27°.

In order to verify that the LIRs are set to excite the same transition, one can do an optical "dip scan" by setting LIR II to its peak signal and sweeping through LIR I. The signal is measured with reference to the chopping of the CO_2 laser beam entering LIR II. The laser beam in LIR I is not chopped. An example is shown below in Fig. 3.13, again for the $9K_{4.5}$ to $20L_{5.5}$ case. As

LIR I moves through the transition frequency, the signal in LIR II dips as the laser beam reduces the population of the $9K_{4.5}$ state and thus the $20L_{5.5}$ state.

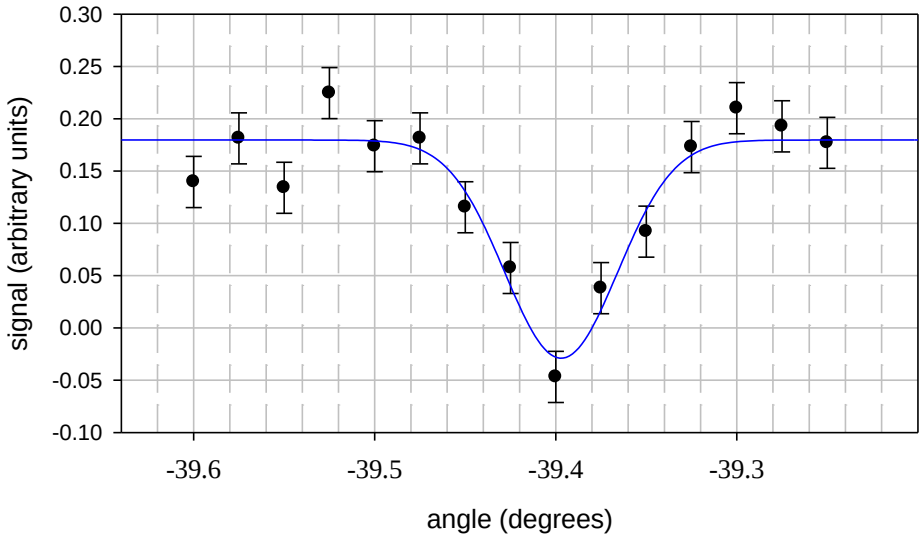

Figure 3.13: Dip scan for the Ni $9K_{4.5}$ to $20L_{5.5}$ transition, taken from SW03_076b. Note that the signal is with reference to the chopping of the CO_2 laser beam going into LIR II while sweeping through the angle in LIR I (where the laser beam is not chopped).

Note that the fact that the LIR II signal drops to near zero when LIR I is on resonance supports the assumption that both regions saturate the transition. In this particular situation, the proper positions of LIR I and LIR II are fairly clear. In cases where the desired LIR signal overlaps with another, it is best to perform a dip scan before moving onto the RF scan.

The proper power needed for the RF field can be determined by measuring an RF signal at different powers. An example of such a saturation curve is shown below for an argon transition. The power should be high enough to saturate the transition, although setting the power above the transition point can result in power broadening and shifts in the transition frequency. The power is typically set to a level slightly lower than that which gives the peak signal. The power needed for other transitions can then be estimated using information about beam energy and *z* matrix elements.

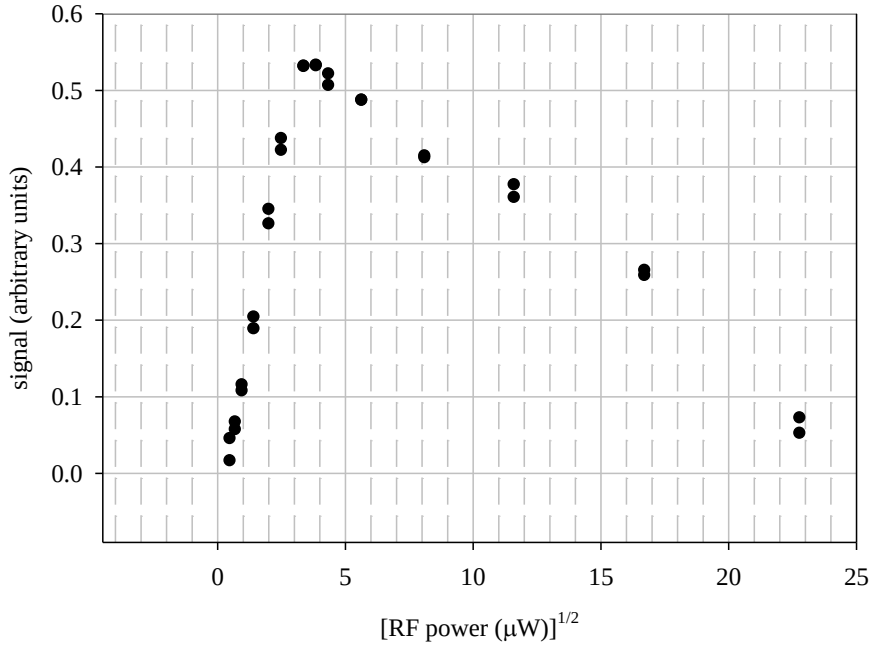

Figure 3.14: Saturation curve for the Ar $10H_{4.5}$ to $10I_{5.5}$ transition, taken from SW05_080, as measured after the RF region and a -3 dB pad.

The final step is to sweep through the RF frequencies with both LIRs set to the same transition. Figure 3.15 shows the population manipulation on- and off-signal. As one can see, the population on the upper n' is increased when the RF frequency ν_{RF} is on resonant with a transition between the lower n levels. Note that the frequency is Doppler-shifted because of the speed of the atoms. One could calculate the nominal Doppler shift using the following:

$$\nu_{co} = \nu_0 \frac{(1+\beta)}{\sqrt{1-\beta^2}} \tag{3.11}$$

or

$$\nu_{counter} = \nu_0 \frac{(1-\beta)}{\sqrt{1-\beta^2}} \tag{3.12}$$

where ν_0 is the unshifted frequency.

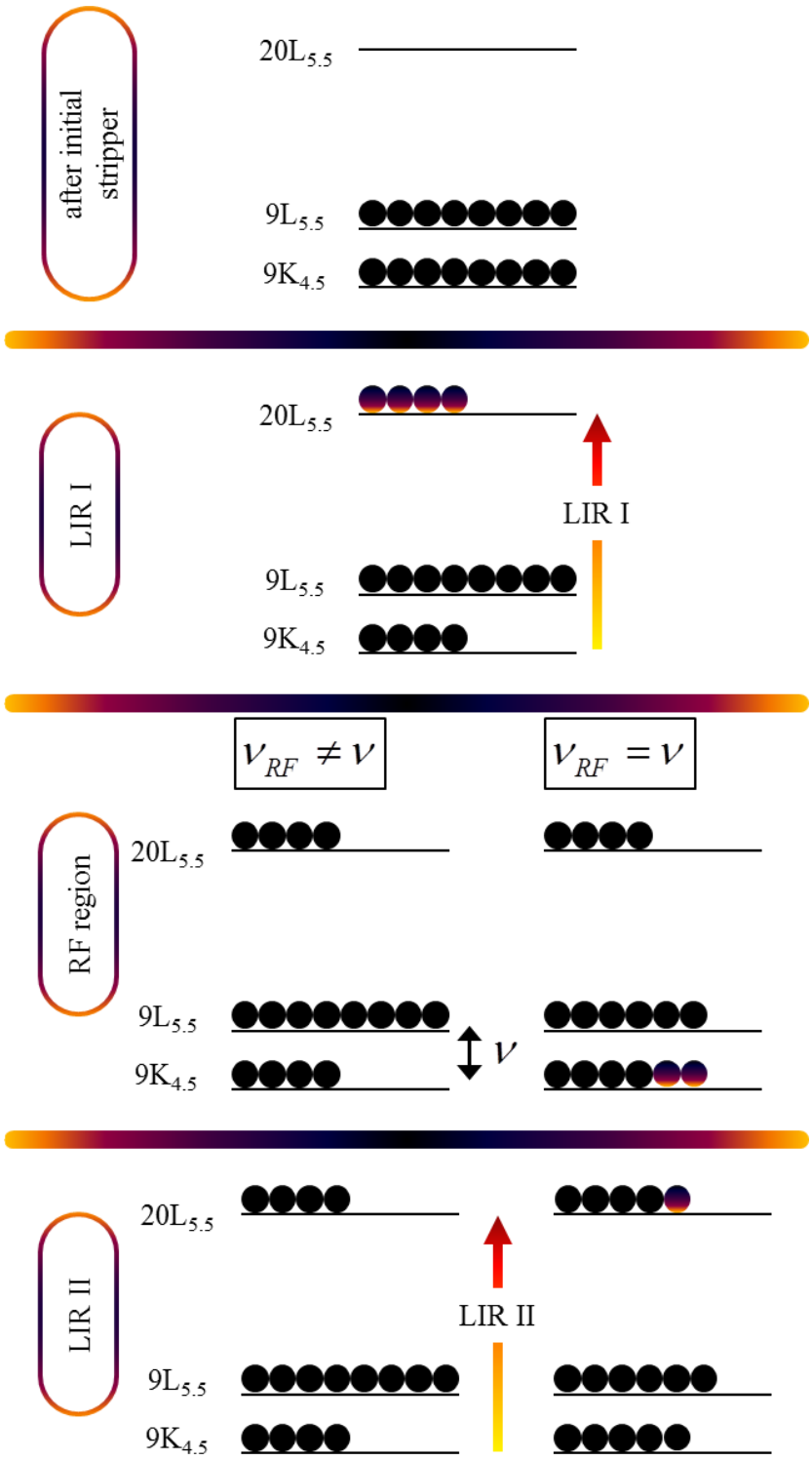

Figure 3.15: RF population diagram showing the RF frequency both on- and off-resonance.

The preferred method, however, to make the measurements with the RF field both co- and counter-propagating with respect to the Rydberg beam, and then average the results. Figure 3.16 shows an example of co- and counter-propagating measurements for a particular transition. Although the spin-splitting discussed in Section 2.2D can result in an increased width, the minimum FWHM of a signal is determined by the transit time through the RF region

$$\mathrm{FWHM}_{\mathrm{min}} = \frac{1}{T_{RF}} = \frac{c\beta}{\text{RF region length}}, \tag{3.13}$$

which would be approximately 1.3 MHz for the RF region shown in Fig. 3.11 (assuming $\beta_{Ni} \approx 0.00056$). The fitted curves of Fig. 3.16 show an average width of 1.4(1) MHz, indicating a small contribution from unresolved spin splitting.

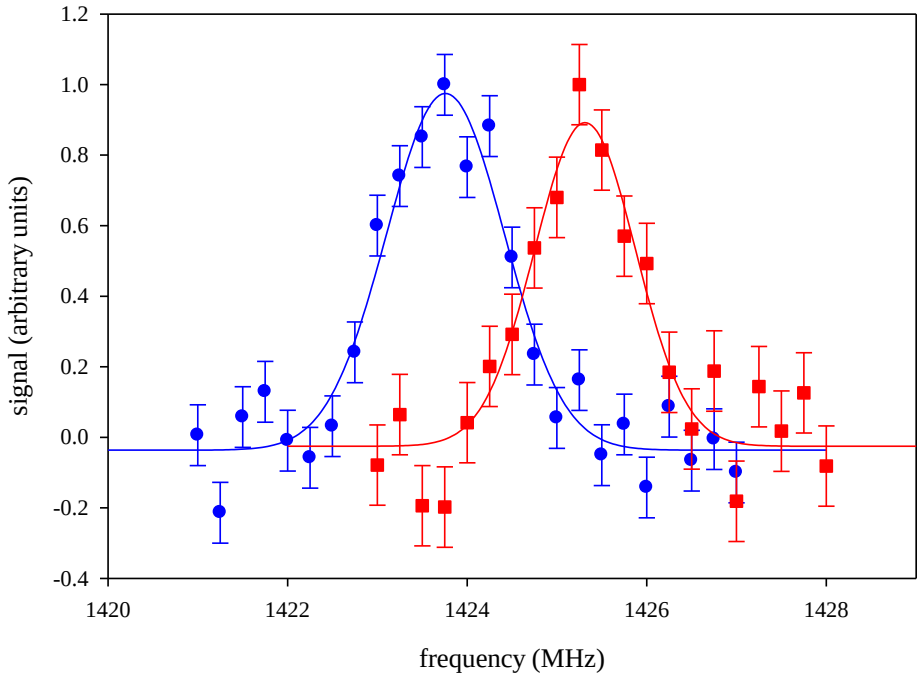

Figure 3.16: Ni co- and counter-propagating transition example ($9K_{5.5}$ to $9L_{6.5}$). The co-propagating signal is shown with red squares while the counter-propagating signal is shown with blue circles. (Data is taken from SW06_039 for the counter-propagating direction and SW06_042 for the co-propagating direction.)

As with the optical RESIS technique, the beam is then Stark ionized in the final stripper and deflected into the CEM. Unlike the optical technique, the CO_2 laser beam is not chopped in either LIR. Instead, the RF field is modulated by the RF generator and the CEM current synchronous with this modulation is measured as a function of RF frequency.

Chapter 4: Measurement of the Nickel Rydberg Fine Structure

4.1 Introduction

Transitions between energy levels of the nickel $n = 9$ Rydberg fine structure were measured using the Microwave Resonant Excitation Stark Ionization Spectroscopy technique. Measurement of fourteen transitions were made connecting 15 of the 18 energy levels within $L = 6$, 7, and 8. Each transition was measured in the co- and counter-propagating directions. Examples of each transition measured are shown in Appendix C.

The following chapter discusses how each measurement is fit to determine the line center. A diagnostic transition is used to measure the electric field at a given point in time and thus determine possible DC Stark shifts that a transition experiences. The AC Stark shift correction, applicable to two-photon transitions, is also discussed. The corrected transitions in the co- and counter-propagating directions are averaged and then used to determine the relative positions of the energy levels. These levels are corrected for relativistic and second-order effects, before being fit to find the structure parameters. Finally, the core properties are extracted by scaling and plotting the structure parameters. A flow chart detailing this process is shown in Fig. 4.1.

4.2 Fitting and Correcting the Observed Transition Frequencies

Each transition measurement was fit using two Gaussians separated by the calculated spin splitting due to the magnetic moment of the Rydberg electron. Assume a transition between nL_K and $nL'_{K'}$; each level is split into two states with $J = K \pm ½$ (or $J' = K' \pm ½$). The dominant transitions between J and J' are shown in Fig. 4.2. Note that the states are "normal", meaning that the K+½ state has a higher energy than the K-½ state.

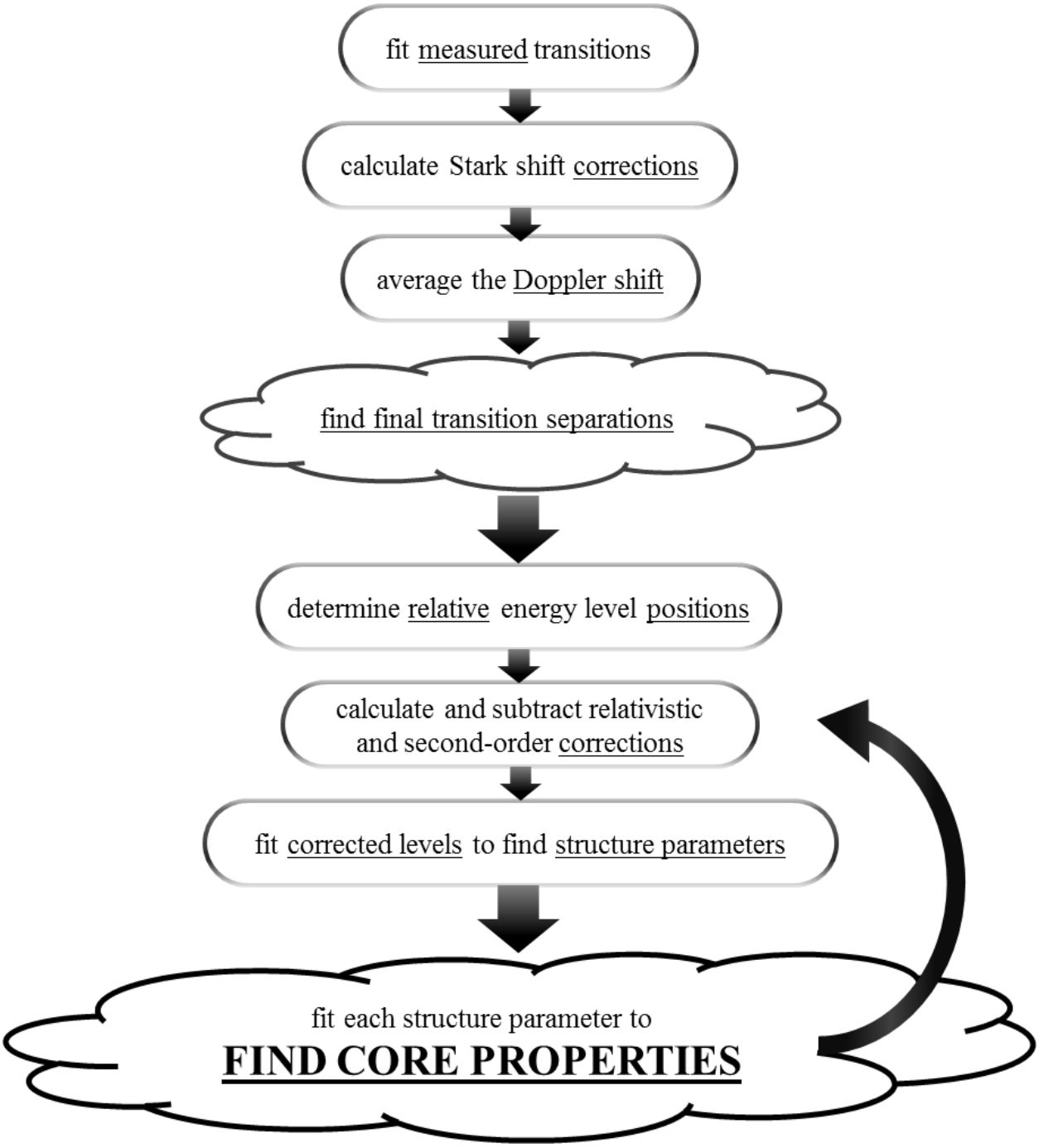

Figure 4.1: Flow chart describing the analysis procedure. Note that the process must be iterated because the second-order corrections depend on the core properties.

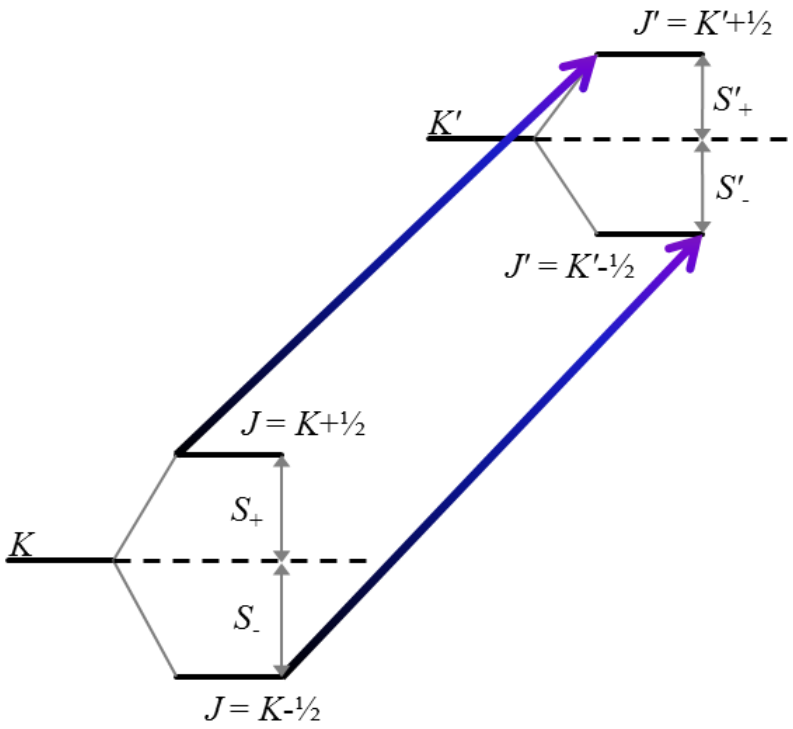

Figure 4.2: Diagram showing spin splitting for a K state ($J = K \pm 1/2$) and a K' state ($J' = K' \pm 1/2$). Arrows show the dominant J to J' transitions.

The fitting function took the form of

$$y_0 + a(2K+2)\exp\left[-\frac{1}{2}\left(\frac{x-(x_0+S'_+-S_+)}{b}\right)^2\right] + a(2K)\exp\left[-\frac{1}{2}\left(\frac{x-(x_0+S'_--S_-)}{b}\right)^2\right], \quad (4.1)$$

$$(S_- \text{ and } S'_- < 0)$$

where the calculated values for the splittings (Eq. 2.98 from Section 2.2D) are shown in Table 4.1. The coefficients $(2K+2)$ and $(2K)$ were included to allow for the slight difference in the relative weight of each transition. Figure 3.16 showed a transition where the spin-splitting is unresolved. Some of the transitions, however, had spin splittings larger than the minimum full-width half-maximum (discussed in Section 3.7). A fit of two independent Gaussians in these cases were consistent with the predicted spin splittings. Figure 4.3 shows an example of such a transition, $9I_{7.5}$ to $9K_{7.5}$, which gives a measured splitting, of 2.24(11) MHz, consistent with the predicted value of 2.2858 MHz. The results of these fits are shown in Table 4.2.

Table 4.1: Calculated spin splittings for $n = 9$. Column 1 gives the state. For clarity, the L and K of the state are explicitly written in columns 2 and 3, respectively. Column 4 gives the position of the $J = K+½$ state and column 5 gives the position of the $J = K-½$ state, both with respect to the center of gravity of the two states. The difference is in column 6. All energies are in MHz.

State	L	K	S_+	S_-	difference
$9I_{3.5}$	6	3.5	1.0881	-1.3990	2.4870
$9I_{4.5}$	6	4.5	1.2107	-1.4798	2.6905
$9I_{5.5}$	6	5.5	1.5183	-1.7943	3.3126
$9I_{6.5}$	6	6.5	2.0211	-2.3321	4.3532
$9I_{7.5}$	6	7.5	2.7384	-3.1035	5.8419
$9I_{8.5}$	6	8.5	3.6933	-4.1278	7.8210
$9K_{4.5}$	7	4.5	1.0073	-1.2311	2.2383
$9K_{5.5}$	7	5.5	1.1164	-1.3194	2.4359
$9K_{6.5}$	7	6.5	1.335	-1.5403	2.8753
$9K_{7.5}$	7	7.5	1.6669	-1.8892	3.5561
$9K_{8.5}$	7	8.5	2.1207	-2.3702	4.4908
$9K_{9.5}$	7	9.5	2.7066	-2.9915	5.6981
$9L_{5.5}$	8	5.5	0.8962	-1.0591	1.9553
$9L_{6.5}$	8	6.5	0.9874	-1.1394	2.1268
$9L_{7.5}$	8	7.5	1.1471	-1.3000	2.4471
$9L_{8.5}$	8	8.5	1.3769	-1.5389	2.9158
$9L_{9.5}$	8	9.5	1.681	-1.8580	3.5390
$9L_{10.5}$	8	10.5	2.0645	-2.2611	4.3256

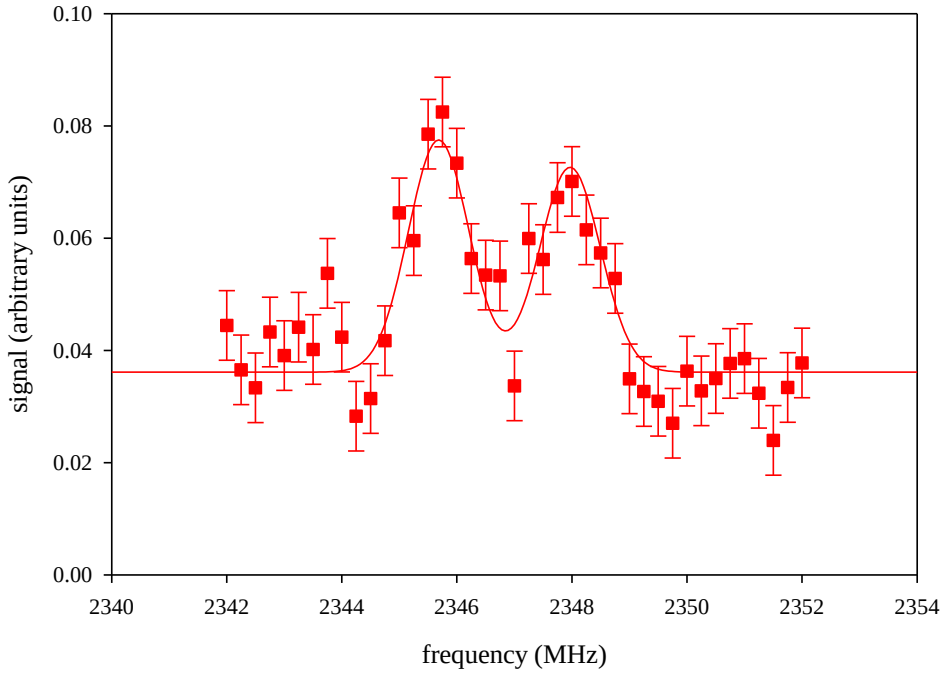

Figure 4.3: Ni microwave transition showing resolved spin splitting, specifically the co-propagating $9I_{7.5}$ to $9K_{7.5}$ transition. Calculations predict a splitting of 2.2858 MHz while a double Gaussian fit gives a completely consistent value of 2.24(11) MHz. (Taken from SW06_098.)

Table 4.2: Measured Ni transitions. The table is broken into different sections for each transition. Each section is headed by the specific microwave transition, the optical transitions for each LIR, the predicted spin splitting, the calculated DC Stark shift rate (and AC Stark Shift rate for two photon transitions), and the CO_2 laser line used. Column 1 specifies the particular measurement: the lab book and page it was taken on, along with the direction of propagation of the microwaves with respect to the atom beam. Column 2 gives the fitted *a* parameter value and uncertainty while column 3 does the same for the *b* parameter. The fitted center is in column 4. Each measurement is the average of two passes, except where noted. The single photon transitions have the DC Stark shift in column 5, while the two photon transitions have both the DC Stark shift and the AC Stark shift. Column 6 is the corrected center. Each co- and counter-propagating measurements pair is then Doppler averaged, as shown in column 7. Those numbers are then averaged to find the final transition separation, shown at the bottom of each section. The error quoted is the internal error except for the transitions where the external average is larger. Notes: The measurement marked with an [a] is the average of two single pass scans (SW03_142 and SW03_143). The measurements marked with an [1] are single pass scans. The [E] indicates no electric field diagnostic when that particular measurement was taken. An * indicates an external error. All energies are in MHz.

Transition: $9I_{4.5}$ to $9K_{5.5}$ Optical Transition (LIR I = LIR II): $9I_{4.5}$-$20K_{5.5}$ Laser Line: 9R(24)

Predicted Spin Splitting: 0.2547 MHz Calculated DC Stark Shift Rate: -0.71 MHz/(V/cm)^2

book	page	direction	fitted a	fitted b	fitted center	DC Stark Shift	corrected center	Doppler averaged
04	16	⇉	0.0018 (2)	0.59 (10)	3297.309 (81)	0.0000 (71) [E]	3297.309 (81)	3295.445 (49)
04	15	⇆	0.0017 (1)	0.62 (7)	3293.580 (54)	0.0000 (71) [E]	3293.580 (54)	
06	48	⇉	0.0017 (2)	0.51 (6)	3297.351 (52)	0.0000 (8)	3297.351 (52)	3295.498 (39)
06	47	⇆	0.0018 (2)	0.53 (7)	3293.645 (58)	0.0000 (8)	3293.645 (58)	

Final: 3295.471 (31)

Table 4.2 continued:

Transition: $9I_{5.5}$ to $9K_{6.5}$ Optical Transition (LIR I = LIR II): $9I_{5.5}$-$19K_{6.5}$ Laser Line: 9P(16)

Predicted Spin Splitting: 0.4373 MHz Calculated DC Stark Shift Rate: -4.20 MHz/(V/cm)^2

book	page	direction	fitted a	fitted b	fitted center	DC Stark Shift	corrected center	Doppler averaged
04	42	⇉	0.0023 (2)	0.78 (9)	1110.620 (58)	0.0000 (46)	1110.620 (58)	1109.979 (35)
04	47	⇆	0.0029 (2)	0.51 (5)	1109.337 (38)	0.0000 (46)	1109.337 (39)	
06	34	⇉	0.0022 (2)	0.60 (6)	1110.726 (47)	0.0000 (46)	1110.726 (47)	1110.013 (34)
06	37	⇆	0.0025 (2)	0.46 (6)	1109.299 (50)	0.0000 (46)	1109.299 (50)	

Final: 1109.996 (24)

Transition: $9I_{5.5}$ to $9K_{5.5}$ Optical Transition (LIR I = LIR II): $9I_{5.5}$-$19K_{6.5}$ Laser Line: 9P(16)

Predicted Spin Splitting: 0.9768 MHz Calculated DC Stark Shift Rate: -1.22 MHz/(V/cm)^2

book	page	direction	fitted a	fitted b	fitted center	DC Stark Shift	corrected center	Doppler averaged
04	45	⇉	0.0016 (5)	0.46 (19)	2719.626 (126)	0.0000 (13)	2719.626 (126)	2718.010 (76)
04	46	⇆	0.0019 (4)	0.50 (15)	2716.394 (84)	0.0000 (13)	2716.394 (84)	
06	35	⇉	0.0016 (3)	0.52 (16)	2719.474 (99)	0.0000 (13)	2719.474 (99)	2718.068 (66)
06	36	⇆	0.0017 (4)	0.36 (8)	2716.663 (87)	0.0000 (13)	2716.663 (87)	

Final: 2718.039 (50)

Table 4.2 continued:

Transition: $9I_{6.5}$ to $9K_{7.5}$ Optical Transition (LIR I = LIR II): $9I_{6.5}$-$19K_{7.5}$ Laser Line: 9P(16)

Predicted Spin Splitting: 0.7971 MHz Calculated DC Stark Shift Rate: -0.45 MHz/(V/cm)^2

book	page	direction	fitted a	fitted b	fitted center	DC Stark Shift	corrected center	Doppler averaged
04	56	⇉	0.0029 (5)	0.37 (7)	118.565 (61)	0.0000 (5)	118.565 (61)	118.561 (43)
04	53	⇆	0.0029 (5)	0.37 (7)	118.557 (60)	0.0000 (5)	118.557 (60)	
06	15	⇉	0.0021 (3)	0.46 (9)	118.532 (57)	0.0000 (5)	118.532 (57)	118.550 (43)
06	12	⇆	0.0017 (3)	0.45 (11)	118.569 (64)	0.0000 (5)	118.569 (64)	
							Final:	118.556 (30)

Transition: $9I_{7.5}$ to $9K_{8.5}$ Optical Transition (LIR I = LIR II): $9I_{7.5}$-$19K_{8.5}$ Laser Line: 9P(16)

Predicted Spin Splitting: 1.3510 MHz Calculated DC Stark Shift Rate: -53.06 MHz/(V/cm)^2

book	page	direction	fitted a	fitted b	fitted center	DC Stark Shift	corrected center	Doppler averaged
04	82	⇉	0.0034 (3)	0.60 (56)	517.477 (50)	-0.1246 (582)	517.601 (767)	517.247 (547)
04	79	⇆	0.0029 (2)	0.65 (6)	516.768 (52)	-0.1246 (582)	516.893 (780)	
06	24	⇉	0.0039 (2)	0.61 (37)	517.581 (34)	0.0000 (575)	517.581 (666)	517.307 (466)
06	27	⇆	0.0042 (2)	0.66 (40)	517.034 (31)	0.0000 (575)	517.034 (653)	
06	97	⇉	0.0029 (2)	0.66 (57)	517.588 (44)	0.0000 (575)	517.588 (724)	517.280 (524)
06	96	⇆	0.0026 (2)	0.60 (53)	516.972 (50)	0.0000 (575)	516.972 (758)	
							Final:	517.278 (297)

Table 4.2 continued:

Transition: $9I_{7.5}$ to $9K_{7.5}$ Optical Transition (LIR I = LIR II): $9I_{7.5}$-$19K_{8.5}$ Laser Line: 9P(16)

Predicted Spin Splitting: 2.2858 MHz Calculated DC Stark Shift Rate: -16.75 MHz/(V/cm)^2

book	page	direction	fitted a	fitted b	fitted center	DC Stark Shift	corrected center	Doppler averaged
04	81	⇉	0.0017 (2)	0.53 (62)	2346.738 (65)	-0.0393 (184)	2346.777 (671)	2345.472 (485)
04	80	⇆	0.0016 (1)	0.64 (56)	2344.127 (68)	-0.0393 (184)	2344.166 (701)	
06	25	⇉	0.0015 (2)	0.60 (67)	2346.736 (77)	0.0000 (181)	2346.736 (793)	2345.452 (587)
06	26	⇆	0.0012 (2)	0.52 (80)	2344.167 (85)	0.0000 (181)	2344.167 (866)	
06	98	⇉	0.0024 (2)	0.53 (47)	2346.755 (49)	0.0000 (181)	2346.755 (524)	2345.482 (365)
06	95	⇆	0.0017 (1)	0.54 (44)	2344.209 (47)	0.0000 (181)	2344.209 (508)	

Final: 2345.468 (282)

Transition: $9K_{4.5}$ to $9L_{5.5}$ Optical Transition (LIR I = LIR II): $9K_{4.5}$-$20L_{5.5}$ Laser Line: 9R(24)

Predicted Spin Splitting: 0.2831 MHz Calculated DC Stark Shift Rate: 0.37 MHz/(V/cm)^2

book	page	direction	fitted a	fitted b	fitted center	DC Stark Shift	corrected center	Doppler averaged
04	21	⇉	0.0029 (2)	0.52 (6)	2903.362 (49)	0.0000 (37) E	2903.362 (49)	2901.718 (34)
04	22	⇆	0.0030 (2)	0.55 (6)	2900.074 (47)	0.0000 (37) E	2900.074 (47)	
06	44	⇉	0.0015 (1)	0.57 (6)	2903.238 (54)	0.0000 (4)	2903.238 (54)	2901.622 (47)
06	45	⇆	0.0014 (2)	0.56 (9)	2900.006 (76)	0.0000 (4)	2900.006 (76)	
06	113	⇉	0.0022 (2)	0.56 (7)	2903.262 (56)	0.0000 (4)	2903.262 (56)	2901.662 (45)
06	114	⇆	0.0016 (2)	0.65 (9)	2900.063 (71)	0.0000 (4)	2900.063 (71)	

Final: 2901.667 (28) *

Table 4.2 continued:

Transition: $9K_{5.5}$ to $9L_{6.5}$ Optical Transition (LIR I = LIR II): $9K_{5.5}$-$19L_{6.5}$ Laser Line: 9P(16)

Predicted Spin Splitting: 0.3090 MHz Calculated DC Stark Shift Rate: 0.71 MHz/(V/cm)^2

book	page	direction	fitted a	fitted b	fitted center	DC Stark Shift	corrected center	Doppler averaged
04	65	⇉	0.0026 (2)	0.58 (7)	1425.328 (43)	0.0000 (8)	1425.328 (43)	1424.535 (30)
04	68	⇆	0.0027 (2)	0.55 (5)	1423.741 (42)	0.0000 (8)	1423.741 (42)	
06	42	⇉	0.0018 (2)	0.54 (6)	1425.301 (51)	0.0000 (8)	1425.301 (51)	1424.524 (33)
06	39	⇆	0.0024 (1)	0.64 (5)	1423.746 (42)	0.0000 (8)	1423.746 (42)	

Final: 1424.529 (22)

Transition: $9K_{5.5}$ to $9L_{5.5}$ Optical Transition (LIR I = LIR II): $9K_{5.5}$-$19L_{6.5}$ Laser Line: 9P(16)

Predicted Spin Splitting: 0.4805 MHz Calculated DC Stark Shift Rate: 0.35 MHz/(V/cm)^2

book	page	direction	fitted a	fitted b	fitted center	DC Stark Shift	corrected center	Doppler averaged
04	66	⇉	0.0015 (2)	0.41 (9)	2128.471 (67)	0.0000 (4)	2128.471 (67)	2127.264 (47)
04	67	⇆	0.0020 (3)	0.48 (9)	2126.056 (65)	0.0000 (4)	2126.056 (65)	
06	41	⇉	0.0016 (4)	0.24 (7)	2128.568 (54)	0.0000 (4)	2128.568 (54)	2127.342 (48)
06	40	⇆	0.0013 (2)	0.47 (10)	2126.116 (79)	0.0000 (4)	2126.116 (79)	

Final: 2127.303 (39) *

Table 4.2 continued:

Transition: $9K_{6.5}$ to $9L_{7.5}$ Optical Transition (LIR I = LIR II): $9K_{6.5}$-$19L_{7.5}$ Laser Line: 9P(16)

Predicted Spin Splitting: 0.4282 MHz Calculated DC Stark Shift Rate: -2.98 MHz/(V/cm)^2

book	page	direction	fitted a	fitted b	fitted center	DC Stark Shift	corrected center	Doppler averaged
04	63	⇉	0.0024 (3)	0.46 (7)	179.817 (56)	0.0000 (32)	179.817 (56)	179.696 (37)
04	62	⇆	0.0019 (2)	0.54 (6)	179.575 (49)	0.0000 (32)	179.575 (49)	
06	23	⇉	0.0029 (1)	0.59 (4)	179.735 (29)	0.0000 (32)	179.735 (29)	179.664 (19)
06	22	⇆	0.0029 (1)	0.52 (3)	179.593 (24)	0.0000 (32)	179.593 (25)	
							Final:	179.680 (21)

Transition: $9K_{7.5}$ to $9L_{8.5}$ Optical Transition (LIR I = LIR II): $9K_{7.5}$-$19L_{8.5}$ Laser Line: 9P(16)

Predicted Spin Splitting: 0.6403 MHz Calculated DC Stark Shift Rate: -17.93 MHz/(V/cm)^2

book	page	direction	fitted a	fitted b	fitted center	DC Stark Shift	corrected center	Doppler averaged
04	57	⇉	0.0023 (2)	0.56 (6)	444.713 (41)	0.0000 (194)	444.713 (45)	444.456 (33)
04	60	⇆	0.0025 (2)	0.58 (7)	444.199 (45)	0.0000 (194)	444.199 (49)	
06	16	⇉	0.0033 (2)	0.50 (4)	444.622 (29)	0.0000 (194)	444.622 (35)	444.403 (23)
06	19	⇆	0.0040 (2)	0.58 (4)	444.184 (25)	0.0000 (194)	444.184 (31)	
06	102	⇉	0.0024 (1)	0.58 (5)	444.686 (36)	0.0000 (194)	444.686 (41)	444.445 (25)
06	105	⇆	0.0040 (1)	0.57 (3)	444.205 (22)	0.0000 (194)	444.205 (29)	
							Final:	444.435 (16)

Table 4.2 continued:

Transition: $9K_{7.5}$ to $9L_{7.5}$ Optical Transition (LIR I = LIR II): $9K_{7.5}$-$19L_{8.5}$ Laser Line: 9P(16)

Predicted Spin Splitting: 1.1090 MHz Calculated DC Stark Shift Rate: -9.60 MHz/(V/cm)^2

book	page	direction	fitted a	fitted b	fitted center	DC Stark Shift	corrected center	Doppler averaged
04	58	⇉	0.0014 (2)	0.62 (12)	1417.276 (69)	0.0000 (104)	1417.276 (70)	1416.503 (61)
04	59	⇆	0.0013 (3)	0.35 (8)	1415.731 (100)	0.0000 (104)	1415.731 (101)	
06	17	⇉	0.0011 (2)	0.66 (19)	1417.272 (109)	0.0000 (104)	1417.272 (109)	1416.522 (61)
06	18	⇆	0.0015 (1)	0.66 (9)	1415.772 (54)	0.0000 (104)	1415.772 (55)	
06	103	⇉	0.0015 (2)	0.64 (13)	1417.046 (75)	0.0000 (104)	1417.046 (76)	1416.442 (52)
06	104	⇆	0.0016 (2)	0.59 (11)	1415.838 (72)	0.0000 (104)	1415.838 (72)	

Final: 1416.489 (34)

Table 4.2 continued:

Transition: $9I_{3.5}$ to $9L_{5.5}$ Optical Transition (LIR I, LIR II): $9I_{3.5}$-$20K_{4.5}$, $9L_{5.5}$-$20M_{6.5}$ Laser Line: 9R(24)

★2 PHOTON★ Calculated DC Stark Shift Rate: 0.27 MHz/(V/cm)^2

Predicted Spin Splitting: 0.2659 MHz Measured AC Stark Shift Rate: 0.0023(18) MHz/mW

book	page	direction	fitted a	fitted b	fitted center	Stark Shift	corrected center	Doppler averaged
03	142	⇉	-0.0018 (2)	0.32 (4)	4301.740 (31) [a]	DC 0.0000 (27) [E] AC 0.0782 (626)	4301.662 (70)	4299.242 (51)
03	145	⇆	-0.0017 (2)	0.29 (4)	4296.899 (38) [1]	DC 0.0000 (27) [E] AC 0.0782 (626)	4296.821 (73)	
06	50	⇉	-0.0031 (3)	0.28 (4)	4301.741 (28)	DC 0.0000 (3) AC 0.0920 (736)	4301.649 (79)	4299.216 (58)
06	51	⇆	-0.0023 (4)	0.27 (5)	4296.875 (43) [1]	DC 0.0000 (3) AC 0.0920 (736)	4296.783 (85)	
06	108	⇉	-0.0034 (3)	0.30 (4)	4301.713 (29)	DC 0.0000 (3) AC 0.0621 (497)	4301.651 (57)	4299.198 (43)
06	107	⇆	-0.0028 (4)	0.24 (4)	4296.812 (34)	DC 0.0000 (3) AC 0.0667 (531)	4296.745 (63)	

The spin splittings and shift rates noted above refer to the *measured* transition and must be multiplied by two if discussing the *full* transition.

Final: 4299.218 (29)

Full Transition: 8598.437 (59)

Table 4.2 continued:

Transition: $9I_{7.5}$ to $9L_{9.5}$ Optical Transition (LIR I = LIR II): $9I_{7.5}$-$19K_{8.5}$ Laser Line: 9P(16)

★2 PHOTON★ Calculated DC Stark Shift Rate: 34.83 MHz/(V/cm)^2

Predicted Spin Splitting: 1.1515 MHz Measured AC Stark Shift Rate: 0.0108(23) MHz/mW

book	page	direction	fitted a	fitted b	fitted center	Stark Shift	corrected center	Doppler averaged
04	83	⇉	0.0022 (2)	0.35 (2)	266.490 (31)	DC 0.0818 (191) AC 0.0810 (171)	266.327 (40)	266.195 (38)
04	84	⇆	0.0010 (1)	0.39 (5)	266.219 (60)	DC 0.0818 (191) AC 0.0756 (160)	266.062 (65)	
06	93	⇉	0.0021 (1)	0.33 (2)	266.359 (22)	DC 0.0000 (377) AC 0.0713 (150)	266.287 (46)	266.145 (32)
06	94	⇆	0.0025 (1)	0.33 (2)	266.075 (20)	DC 0.0000 (377) AC 0.0713 (150)	266.003 (46)	

The spin splittings and shift rates noted above refer to the *measured* transition and must be multiplied by two if discussing the *full* transition.

Final: 266.170 (25)

Full Transition: 532.340 (50)

Once the transition centers have been found they must be corrected for DC Stark shifts and, if applicable, AC Stark shifts. The first correction considered is the possibility of a DC Stark shift due to stray electric fields. Measurements of a diagnostic transition, $10H_{4.5}$ to $10I_{5.5}$ in argon, were made often since the field, most likely due to the charging up of surfaces in the RF region, varied day-to-day. Reference [5] referred to this transition as *D* and determined its zero-field position, D_0, to be

$$D_0 = 1398.13(20)\ \text{MHz}. \tag{4.2}$$

With a shift rate of 184.6 MHz/(V/cm)^2, this diagnostic transition is more than twice as sensitive to stray electric fields as any of the nickel transitions measured. The square of the electric field is thus given by

$$\left|\vec{E}\right|^2 = \frac{D - D_0}{184.6\ \text{MHz}/\left(\text{V/cm}\right)^2}. \tag{4.3}$$

If the measurement of *D* was consistent with D_0, the shift would be 0 MHz but assigned an uncertainty of

$$0.20\text{MHz} \times \frac{\text{Ni transition shift rate}}{184.6\ \text{MHz}/\left(\text{V/cm}\right)^2}. \tag{4.4}$$

Note that the 0.20 MHz comes from the uncertainty in the position of D_0. If a nickel transition measurement occurred without a measurement of *D* nearby then it was assigned a 0 MHz shift. Its uncertainty, however, was (0.1 V/cm)^2 times the shift rate. The value of 0.1 V/cm was chosen since it is larger than any value of $\left|\vec{E}\right|$ measured throughout this experiment.

The second correction considered, affecting only the two-photon transitions, is the possibility of AC Stark shifts. Note that for the two-photon transitions all corrections are made to the observed frequency, giving a result that is then doubled to give the full separation between

the two energy levels. Measurements were made in the co-propagating direction at multiple powers for both of the two-photon transitions. By plotting these measurements versus power for each transition, once can find the rate at which these transitions shift due to power. Figure 4.4 shows such a plot for the nickel $9I_{3.5}$ to $9L_{5.5}$ transition. A linear fit to the data gives an AC Stark shift rate of 0.0023(18) MHz/mW and thus a shift of less than 0.1 MHz to the observed frequencies. Plotting the $9I_{7.5}$ to $9L_{9.5}$ transition, Fig. 4.5, gave an AC Stark shift rate of 0.0108(23) MHz/mW and again a shift of less than 0.1 MHz to the observed frequencies.

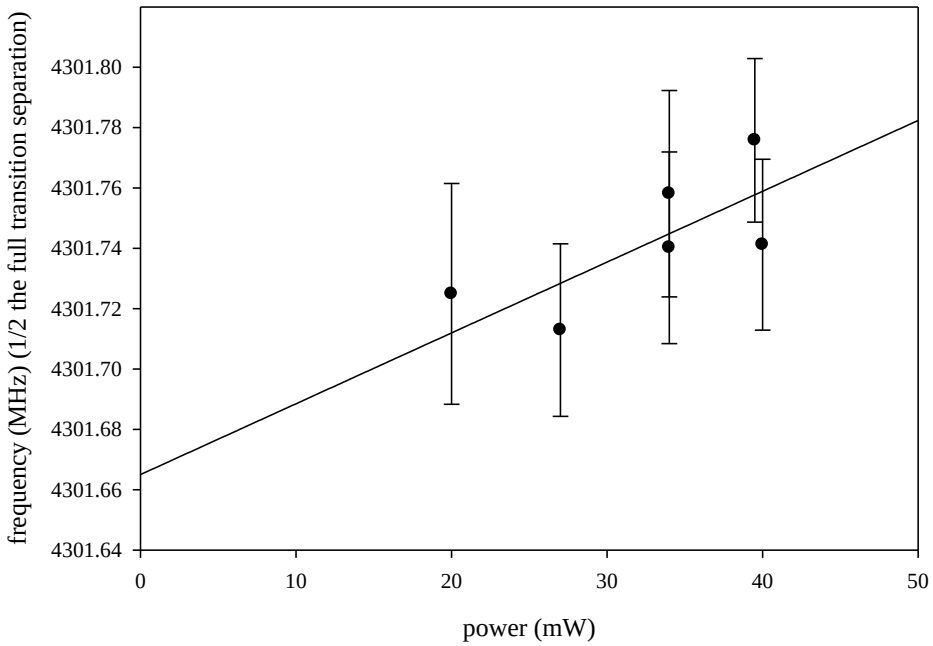

Figure 4.4: Ni $9I_{3.5}$ to $9L_{5.5}$ AC Stark shift plot showing the upward shift of the transition as the power increases. Note that the y-axis shows the measured frequency, thus the full transition separation is found by multiplying it by two.

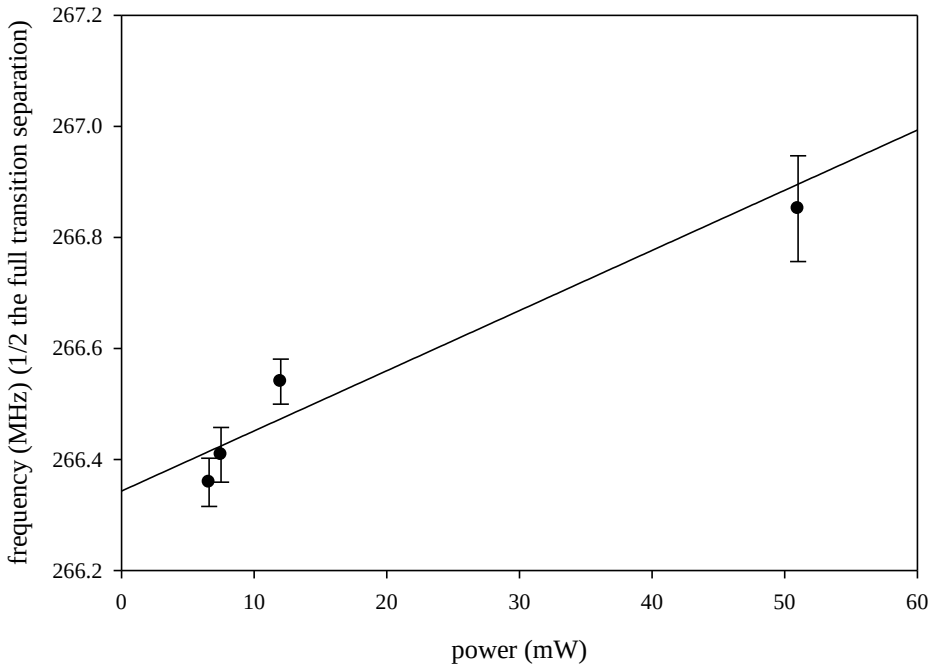

Figure 4.5: Ni $9I_{7.5}$ to $9L_{9.5}$ AC Stark shift plot showing the upward shift of the transition as the power increases. Note that the y-axis shows the measured frequency, thus the full transition separation is found by multiplying it by two.

Once the corrections were made to the measurements, each set of co- and counter-propagating measurements were averaged to find the unshifted center. These centers were then averaged to give the final result for each transition. The internal error of a transition's final value is due to the uncertainty of each day's measurements and is given by $\frac{1}{N}\sqrt{\sum_{i=1}^{N}\sigma_i^2}$, where N is number co- and counter-propagating pairs. The external error is due to the variation from measurement to measurement: $\sqrt{\frac{1}{N(N-1)}\sum_{i=1}^{N}(x_i-\bar{x})^2}$. The larger of the two was taken as the final error.

4.3 Energy Level Corrections and Structure Parameters

An arbitrary state is chosen to be the zero point in the energy level diagram; for nickel the $9I_{5.5}$ state was chosen. The positions of the other states are then calculated relative to it. Figure 4.6 shows such a level diagram. Each state is corrected for the relativistic and second-order effects discussed in Sections 2.2C and 2.2D. Note that these corrections, shown in Table 4.3, are small when compared to the scale of the energy pattern. The corrected energies are then related to the expectation value of the effective potential of Chapter 2.

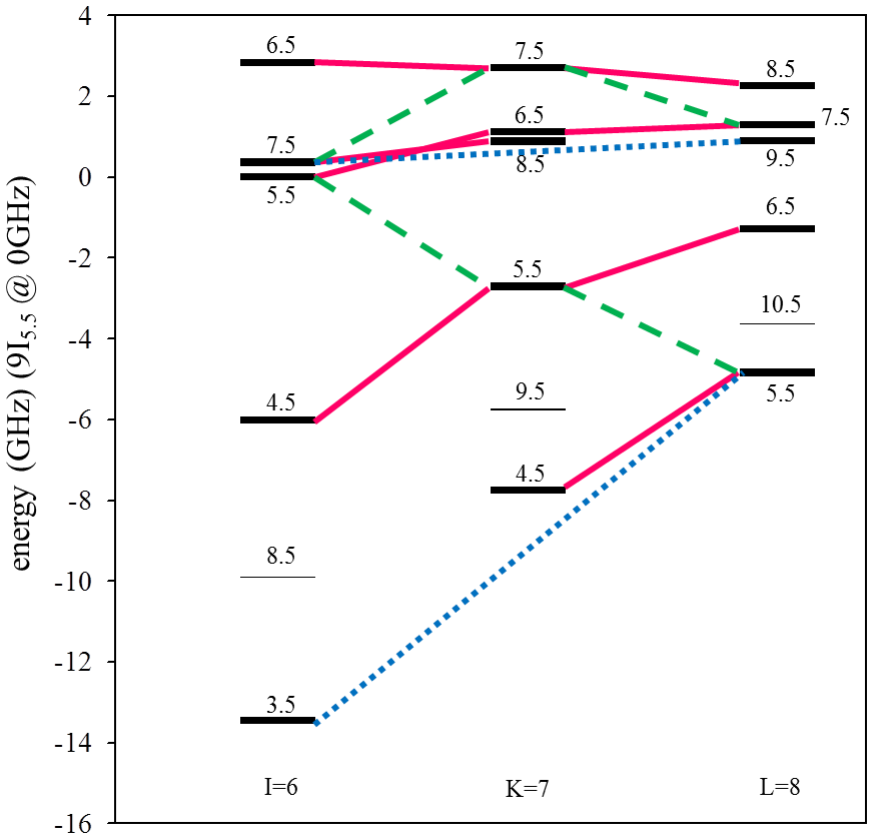

Figure 4.6: Energy level diagram with $9I_{5.5}$ at 0 GHz. Each state is labeled by its K (next to its position) and its L (at the bottom of the plot). The measured transitions connecting each state are also shown: solid pink lines for $\Delta K = 1$, dashed green lines for $\Delta K = 0$, and dotted blue lines for two-photon transitions. Note that 15 of the 18 energy levels were connected by the measured transitions; the positions of the other energy levels were calculated using core property measurements.

Table 4.3: Ni n = 9 Rydberg fine structure energy levels and corrections where the $9I_{5.5}$ energy level has been taken as the zero point. Column 1 gives the observed energy while column 2 gives the measurement uncertainty. Column 2 gives the calculated relativistic energy. The second-order energies in V_{eff} are given in column 4. Its uncertainties due to convergence and the core properties are in columns 5 and 6, respectively, with the total uncertainty in column 7. Column 8 gives the observed energies corrected for columns 2 and 4. The total uncertainty of the corrected energies, column 9, is the combination of columns 3 and 7. All energies are in MHz.

State	E_{obs}	σ_{meas}	E_{rel}	$E_{eff}^{[2]}$	σ_{conv}	σ_{prop}	$\sigma_{total}^{[2]}$	$E_{eff}^{[1]}$	$\sigma_{total}^{[1]}$
$9I_{3.5}$	-13443.779	(0.087)	-16.945	-5.287	(0.999)	(2.771)	(2.946)	-13421.546	(2.947)
$9I_{4.5}$	-6013.510	(0.059)	-16.945	9.097	(1.165)	(2.355)	(2.627)	-6005.662	(2.628)
$9I_{5.5}$	0	(0.075)	-16.945	11.308	(1.347)	(1.295)	(1.868)	5.637	(1.870)
$9I_{6.5}$	2824.721	(0.078)	-16.945	2.294	(1.475)	(0.076)	(1.477)	2839.372	(1.479)
$9I_{7.5}$	360.697	(0.077)	-16.945	-11.012	(1.455)	(1.001)	(1.766)	388.654	(1.768)
$9I_{8.5}$	—	—	-16.945	-16.789	(1.201)	(0.402)	(1.266)	—	—
$9K_{4.5}$	-7747.009	(0.070)	-12.016	6.862	(0.147)	(1.811)	(1.817)	-7741.855	(1.822)
$9K_{5.5}$	-2718.039	(0.050)	-12.016	12.650	(0.173)	(1.858)	(1.867)	-2718.673	(1.867)
$9K_{6.5}$	1109.996	(0.024)	-12.016	8.427	(0.217)	(0.941)	(0.966)	1113.584	(0.966)
$9K_{7.5}$	2706.165	(0.072)	-12.016	0.803	(0.249)	(0.018)	(0.250)	2717.378	(0.260)
$9K_{8.5}$	877.975	(0.083)	-12.016	-2.956	(0.243)	(0.162)	(0.292)	892.947	(0.303)
$9K_{9.5}$	—	—	-12.016	-4.780	(0.202)	(0.086)	(0.219)	—	—
$9L_{5.5}$	-4845.342	(0.064)	-8.246	-1.883	(0.038)	(0.082)	(0.090)	-4835.213	(0.111)
$9L_{6.5}$	-1293.510	(0.055)	-8.246	0.010	(0.044)	(0.105)	(0.113)	-1285.274	(0.126)
$9L_{7.5}$	1289.676	(0.032)	-8.246	0.873	(0.047)	(0.049)	(0.068)	1297.049	(0.075)
$9L_{8.5}$	2261.730	(0.074)	-8.246	0.559	(0.048)	(0.004)	(0.048)	2269.417	(0.088)
$9L_{9.5}$	893.037	(0.097)	-8.246	-0.589	(0.046)	(0.028)	(0.054)	901.872	(0.111)
$9L_{10.5}$	—	—	-8.246	-1.351	(0.039)	(0.018)	(0.043)	—	—

As discussed previously, the second-order energies depend on the dominant core parameters of the effective potential

$$E_{eff}^{[2]}\left(nL_K\right)=\sum_{J_c',n',L'}{}'\frac{\left\langle\left(gJ_c\right)nL_K\left|V_{eff}\right|\left(gJ_c'\right)n'L_K'\right\rangle\left\langle\left(gJ_c'\right)n'L_K'\left|V_{eff}\right|\left(gJ_c\right)nL_K\right\rangle}{\Delta E\left(gJ_c'\right)+E\left(n'\right)-E\left(n\right)},$$

where

$$V_{eff}\approx-\frac{1}{2}\frac{\alpha_{D,0}}{r^4}-\left(\frac{Q\left(J_c'\right)}{r^3}+\frac{1}{2}\frac{\alpha_{D,2}\left(J_c'\right)}{r^4}\right)\frac{X^{[2]}\left(J_c\right)\cdot C^{[2]}\left(\hat{r}\right)}{\begin{pmatrix}J_c & 2 & J_c\\ -J_c & 0 & J_c\end{pmatrix}}.$$

As such, an iterative approach must be taken when calculating these corrections until the core parameters found are consistent with those used. Using the effective potential above, there are six second-order energy terms: QQ, $Q\alpha_{D,0}$, $\alpha_{D,0}\alpha_{D,0}$, $Q\alpha_{D,2}$, $\alpha_{D,0}\alpha_{D,2}$, and $\alpha_{D,2}\alpha_{D,2}$. The $E_{eff}^{[2]}$ calculated for each level, broken down into these six types and the two possible intermediate core states, are shown in Table 4.4. The terms that involve the quadrupole moment tend to dominate, but the relative importance of each term varies with *L* and *K*.

Table 4.4: Second-order energies in V_{eff} for L = 6, 7 and 8. The initial state is given in column 1 and the intermediate state in column 2. Columns 3 through 8 give the six different terms. All energies are in MHz.

State	$L_c J_c'$	QQ	$Q\alpha_{D,0}$	$\alpha_{D,0}\alpha_{D,0}$	$Q\alpha_{D,2}$	$\alpha_{D,0}\alpha_{D,2}$	$\alpha_{D,2}\alpha_{D,2}$
$9I_{3.5}$	$D_{5/2}$	-5.093	-8.795	-2.641	0.525	0.442	-0.013
	$D_{3/2}$	7.516	0	0	2.559	0	0.212
$9I_{4.5}$	$D_{5/2}$	6.367	-2.010	-2.641	-0.556	0.101	0.016
	$D_{3/2}$	5.466	0	0	2.161	0	0.194
$9I_{5.5}$	$D_{5/2}$	6.824	3.518	-2.641	-0.612	-0.177	0.019
	$D_{3/2}$	3.082	0	0	1.189	0	0.105
$9I_{6.5}$	$D_{5/2}$	-0.555	6.132	-2.641	0.028	-0.308	0.003
	$D_{3/2}$	-0.289	0	0	-0.071	0	-0.005
$9I_{7.5}$	$D_{5/2}$	-7.878	3.870	-2.641	0.631	-0.195	-0.014
	$D_{3/2}$	-3.784	0	0	-0.940	0	-0.061
$9I_{8.5}$	$D_{5/2}$	-7.593	-5.528	-2.641	0.643	0.278	-0.014
	$D_{3/2}$	-1.531	0	0	-0.377	0	-0.025
$9K_{4.5}$	$D_{5/2}$	-1.542	-2.118	-0.445	0.111	0.072	-0.002
	$D_{3/2}$	8.975	0	0	1.729	0	0.082
$9K_{5.5}$	$D_{5/2}$	2.598	-0.371	-0.445	-0.150	0.013	0.003
	$D_{3/2}$	9.144	0	0	1.774	0	0.084
$9K_{6.5}$	$D_{5/2}$	2.501	0.965	-0.445	-0.141	-0.033	0.003
	$D_{3/2}$	4.636	0	0	0.898	0	0.043
$9K_{7.5}$	$D_{5/2}$	-0.123	1.526	-0.445	0.017	-0.052	0.000
	$D_{3/2}$	-0.101	0	0	-0.017	0	-0.001
$9K_{8.5}$	$D_{5/2}$	-2.451	0.891	-0.445	0.144	-0.030	-0.002
	$D_{3/2}$	-0.900	0	0	-0.155	0	-0.007
$9K_{9.5}$	$D_{5/2}$	-2.549	-1.417	-0.445	0.156	0.048	-0.002
	$D_{3/2}$	-0.484	0	0	-0.082	0	-0.004
$9L_{5.5}$	$D_{5/2}$	-0.555	-0.588	-0.086	0.029	0.014	0.000
	$D_{3/2}$	-0.615	0	0	-0.079	0	-0.003
$9L_{6.5}$	$D_{5/2}$	1.118	-0.078	-0.086	-0.042	0.002	0.000
	$D_{3/2}$	-0.799	0	0	-0.101	0	-0.003
$9L_{7.5}$	$D_{5/2}$	1.132	0.293	-0.086	-0.040	-0.007	0.000
	$D_{3/2}$	-0.370	0	0	-0.047	0	-0.002
$9L_{8.5}$	$D_{5/2}$	0.265	0.433	-0.086	-0.004	-0.010	0.000
	$D_{3/2}$	-0.034	0	0	-0.004	0	0.000
$9L_{9.5}$	$D_{5/2}$	-0.491	0.237	-0.086	0.022	-0.005	0.000
	$D_{3/2}$	-0.237	0	0	-0.028	0	-0.001
$9L_{10.5}$	$D_{5/2}$	-0.725	-0.412	-0.086	0.033	0.010	0.000
	$D_{3/2}$	-0.152	0	0	-0.017	0	-0.001

One difficulty in calculating the second-order energies is the off-diagonal tensor dipole polarizability $\alpha_{D,2}(J_c')$ (Eqn. 2.90). Unlike the off-diagonal quadrupole moment of Eqn. 2.93, which can be estimated by assuming pure *LS* coupling, $\alpha_{D,2}(J_c')$ depends on two different matrix elements for each intermediate state $\lambda'' J_c''$:

$$\alpha_{D,2}(J_c') = 2\sqrt{\frac{10}{3}} \begin{pmatrix} J_c & 2 & J_c \\ -J_c & 0 & J_c \end{pmatrix} (-1)^{J_c'-J_c} \sum_{\lambda'', J_c''} (-1)^{2J_c''} \begin{Bmatrix} J_c'' & 1 & J_c \\ 2 & J_c' & 1 \end{Bmatrix} \frac{\left\langle gJ_c \left\| M^{[1]} \right\| \lambda'' J_c'' \right\rangle \left\langle \lambda_c'' J_c'' \left\| M^{[1]} \right\| gJ_c' \right\rangle}{\Delta E(\lambda'' J_c'')}$$

and thus knowing their relative sign is necessary for determining the sign of an excited state's contribution to $\alpha_{D,2}(J_c')$. Reference [40] provides a list of calculated A-values connecting more than 200 core excited states of nickel to its $^2D_{5/2}$ ground state. Since A-values are proportional to the line strength and thus the square of a particular matrix element, the signs cannot be extracted from this information. For *LS* coupled excited states of the form $^2L_c''\ _{J_c''}$, one may calculate the contribution to $\alpha_{D,2}(J_c')$ in terms of the magnitude of the contribution to $\alpha_{D,2}$ by assuming that the states are pure *LS* coupled. The result is

$$\begin{array}{l} -2.625 * \left|\alpha_{D,2}\right| \text{ for } {}^2F_{5/2} \\ +0.188 * \left|\alpha_{D,2}\right| \text{ for } {}^2D_{5/2} \\ +4.500 * \left|\alpha_{D,2}\right| \text{ for } {}^2D_{3/2} \\ -0.500 * \left|\alpha_{D,2}\right| \text{ for } {}^2P_{3/2} \end{array} . \tag{4.5}$$

For excited states of other forms, determining the ratio between $\alpha_{D,2}(J_c')$ and $\left|\alpha_{D,2}\right|$ is much more difficult. One may take the information above, however, and make the rough approximation that the contribution to $\alpha_{D,2}(J_c')$ is

$$\begin{array}{l} -1.2 * \left|\alpha_{D,2}\right| \text{ for } J_c'' = 5/2 \\ +2.0 * \left|\alpha_{D,2}\right| \text{ for } J_c'' = 3/2 \end{array} . \tag{4.6}$$

Using this approximation and the A-values from Ref. [40], one calculates an initial value of -3.2 a.u. for $\alpha_{D,2}\left(J_c'\right)$. The accuracy of the information presented in Ref. [40] can be checked by calculating $\alpha_{D,0}$ (Eq. 2.42) and $\alpha_{D,2}$ (Eq. 2.57), using the energies of Ref. [41] and comparing against measurement. These calculations are presented in Table 4.5. One can see that the calculations overestimate both of the measured core properties, thus it is likely that the initial value of $\alpha_{D,2}\left(J_c'\right) = -3.2$ a.u. overestimates its magnitude. Motivated by this and the assumptions that went into the calculation, the magnitude was halved and assigned an uncertainty of 100%, resulting in the following

$$\alpha_{D,2}\left(J_c'\right) = -1.6(1.6). \tag{4.7}$$

This uncertainty is reflected in the core property uncertainty (σ_{prop}) of the second-order energies. Although the uncertainties of the other properties could contribute to σ_{prop}, their effect is generally much smaller.

Table 4.5: Compares measured core properties values to those calculated using Ref. [40] Column 1 labels where the core property value comes from (measurement or calculated). Column 2 gives the scalar dipole polarizability, column 3 gives the tensor dipole polarizability, and column 4 gives the initial calculated value of the off-diagonal tensor dipole polarizability. All values are in atomic units (a.u.).

	$\alpha_{D,0}$	$\alpha_{D,2}$	$\alpha_{D,2}\left(J_c'\right)$
microwave RESIS	7.925(10)	1.043(32)	—
Ref. [40]	12.97	2.35	-3.2

An additional source of uncertainty in the second-order energies is due to the issue of convergence. The effective potential above leads to terms in $E_{eff}^{[2]}\left(nL_K\right)$ proportional to r^{-6}, r^{-7}, and r^{-8}. The uncertainty due to omitting higher-order terms is estimated to be on the order of the last term included. The value for σ_{conv} presented in Table 4.3 is conservatively taken to be ½

the magnitude of the calculated r^{-8} terms. As mentioned in Section 2.2C, one of the difficulties in calculating the second-order energies is the sum of n' which includes both the discrete and continuum:

$$\sum_{n'} \frac{\left[nL\left|r^{-s}\right|n'L'\right]\left[n'L'\left|r^{-q}\right|nL\right]}{\Delta E\left(gJ_c'\right)+E\left(n'\right)-E\left(n\right)}.$$

The method used here is that of Dalgarno and Lewis [23] as laid out by Ref. [24]. Various tests indicate a numerical accuracy of approximately six decimal places, which is small enough that any uncertainty due to it can be ignored for the purposes of these calculations. The total uncertainty on the second-order energies is thus the quadrature sum of σ_{prop} and σ_{conv} and is labeled $\sigma_{total}^{[2]}$.

The corrected energy levels are given by

$$E_{eff}^{[1]}\left(nL_K\right)=E_{obs}\left(nL_K\right)-E_{eff}^{[2]}\left(nL_K\right)-E_{rel}\left(nL\right), \tag{4.8}$$

and the total uncertainty on each level, $\sigma_{total}^{[1]}$, is a combination of the uncertainties in the measurements and in the second-order energies. In most cases it is dominated by $\sigma_{total}^{[2]}$.

The corrected energies are fit to a function of the form

$$E_{eff}^{[1]}=\left\langle V_{eff}\right\rangle=$$
$$A_0+A_1\left(\vec{L}\cdot\vec{J}_c\right)+A_2\left(\frac{\left\langle X^{[2]}\left(J_c\right)\cdot C^{[2]}\left(\hat{r}_{Ryd}\right)\right\rangle}{\begin{pmatrix} J_c & 2 & J_c \\ -J_c & 0 & J_c \end{pmatrix}}\right)+A_3\left(\left\langle X^{[3]}\left(J_c\right)\cdot T^{[3]}\left(\hat{r}_{Ryd}\right)\right\rangle\right)+A_4\left(\frac{\left\langle X^{[4]}\left(J_c\right)\cdot C^{[4]}\left(\hat{r}_{Ryd}\right)\right\rangle}{\begin{pmatrix} J_c & 4 & J_c \\ -J_c & 0 & J_c \end{pmatrix}}\right) \tag{4.9}$$

in order to find the structure parameters A_0, A_1, etc. For clarity the coefficients for each A_b are shown in Table 4.6.

Table 4.6: *K*-dependence of the effective potential for each tensor order (b = 1 through 4). Note that the tensor and fourth-rank tensor terms include the 3J-symbol. The values shown represent the coefficients of A_b in Eq. 4.9.

State	b = 1	b = 2	b = 3	b = 4
$9I_{3.5}$	-17.5	-0.63636	0.55546	0.84848
$9I_{4.5}$	-13	-0.14545	-0.30154	-1.33333
$9I_{5.5}$	-7.5	0.25455	-0.47611	0
$9I_{6.5}$	-1	0.44364	-0.01190	1.18182
$9I_{7.5}$	6.5	0.28000	0.52372	-0.82353
$9I_{8.5}$	15	-0.40000	-0.21822	0.17647
$9K_{4.5}$	-20	-0.61538	0.60430	0.75524
$9K_{5.5}$	-14.5	-0.10769	-0.39279	-1.32168
$9K_{6.5}$	-8	0.28054	-0.53142	0.12217
$9K_{7.5}$	-0.5	0.44344	0.03436	1.14027
$9K_{8.5}$	8	0.25882	0.60844	-0.86378
$9K_{9.5}$	17.5	-0.41176	-0.26956	0.19505
$9L_{5.5}$	-22.5	-0.60000	0.65465	0.69231
$9L_{6.5}$	-16	-0.08000	-0.48008	-1.30769
$9L_{7.5}$	-8.5	0.29895	-0.58345	0.21053
$9L_{8.5}$	0	0.44211	0.08040	1.10526
$9L_{9.5}$	9.5	0.24211	0.69141	-0.89474
$9L_{10.5}$	20	-0.42105	-0.32158	0.21053

The structure parameters must be found for each L. Since there are five measured energy levels within each L and five structure parameters, a perfect fit results. As with the energy levels, there are uncertainties on the structure parameters due to both the measurements and the second-order energies. The uncertainties due to the measurements are found by first increasing each transition energy by its uncertainty from Table 4.2, recalculating the level positions, and refitting to Eq. 4.9, thus resulting in fourteen sets of structure parameters in addition to the original values. The uncertainty due to measurement error is the square root of the sum of differences squared,

$$\sigma_{meas}\left(A_b\right) = \sqrt{\sum_i \left(A_b\left(\text{original}\right) - A_b\left(i\right)\right)^2}\,.$$

Since the uncertainties on the second-order energies are correlated, one may increase each energy level simultaneously by $\sigma_{total}^{[2]}\left(nL_K\right)$ and refit to find new structure parameters. The difference between these values and the original structure parameters gives $\sigma_{E^{[2]}}\left(A_b\right)$. The results of these calculations are shown in Table 4.7. The final uncertainty on each $A_b\left(nL\right)$ is square root of the sum of these uncertainties squared.

Table 4.7: Fitted structure parameter values. Column 1 gives the *L* while column 2 gives the structure parameter. The uncertainty due to the measurement uncertainties is in column 3 and the uncertainty due to the second-order energy uncertainties is in column 4. Column 5 is the total uncertainty. All values are in MHz.

L	A_0	σ_{meas}	$\sigma_{E^{[2]}}$	σ_{total}
6	-3833.69	(0.26)	(1.64)	(1.66)
7	-1662.60	(0.17)	(0.44)	(0.47)
8	-747.28	(0.19)	(0.01)	(0.19)
L	A_1	σ_{meas}	$\sigma_{E^{[2]}}$	σ_{total}
6	-0.484	(0.034)	(0.068)	(0.076)
7	-0.291	(0.020)	(0.080)	(0.082)
8	-0.400	(0.019)	(0.007)	(0.020)
L	A_2	σ_{meas}	$\sigma_{E^{[2]}}$	σ_{total}
6	15065.94	(0.79)	(0.11)	(0.80)
7	9882.66	(0.51)	(0.23)	(0.56)
8	6826.13	(0.54)	(0.16)	(0.56)
L	A_3	σ_{meas}	$\sigma_{E^{[2]}}$	σ_{total}
6	-1.53	(0.42)	(0.66)	(0.78)
7	-3.02	(0.25)	(0.27)	(0.37)
8	-0.84	(0.23)	(0.07)	(0.24)
L	A_4	σ_{meas}	$\sigma_{E^{[2]}}$	σ_{total}
6	-9.509	(0.074)	(0.232)	(0.243)
7	-2.127	(0.054)	(0.303)	(0.308)
8	-0.996	(0.060)	(0.031)	(0.068)

4.4 Core Properties

The structure parameters are scaled and plotted in order to find the core properties. For the A_0, or scalar, plot, one must look at the difference in scalar structure parameters between adjacent Ls. This is because the scalar term represents the shift away from hydrogenic while the measurements only give information about energy level differences. ΔA_0 is then scaled by the difference in the expectation values of r^{-4} since $\langle r^{-4} \rangle_{nL}$ appears in the first term of the scalar energy (see Eq. 2.41). The A_0 plot, shown in Fig. 4.7, thus takes the form of

$$\frac{\Delta A_0(nL)}{\Delta \langle r^{-4} \rangle_{nL}} = B_0^4 + B_0^6 \frac{\Delta \langle r^{-6} \rangle_{nL}}{\Delta \langle r^{-4} \rangle_{nL}}, \tag{4.10}$$

where the subscript on a particular B represents the tensor order and the superscript represents the inverse power of r that B is coefficient of. Values used to create the plot are shown in Table 4.8. Since the microwave RESIS study focused on L = 6, 7, and 8, this information is represented by the two leftmost data points. To give more confidence to the data pattern, the L = 6-5 ΔA_0 from the optical RESIS study [38] is included in the plot. The optical $A_0(L=6)$ must be used with the optical $A_0(L=5)$ since the optical study used a difference reference point for the energy levels measured (n = 9 hydrogenic rather than $9I_{5.5}$ as was done here). Note that the uncertainties on the points are largely uncorrelated since the uncertainty on the L = 6-5 point is from the optical study, the L = 7-6 point is primarily from the uncertainty of the L = 6 second-order energies, and the L = 8-7 point is a combination of multiple sources. The data is then fit to a line to give

$$\begin{aligned} B_0^4 &= -3.9627(52) \\ B_0^6 &= -9.2(3.3) \end{aligned}. \tag{4.11}$$

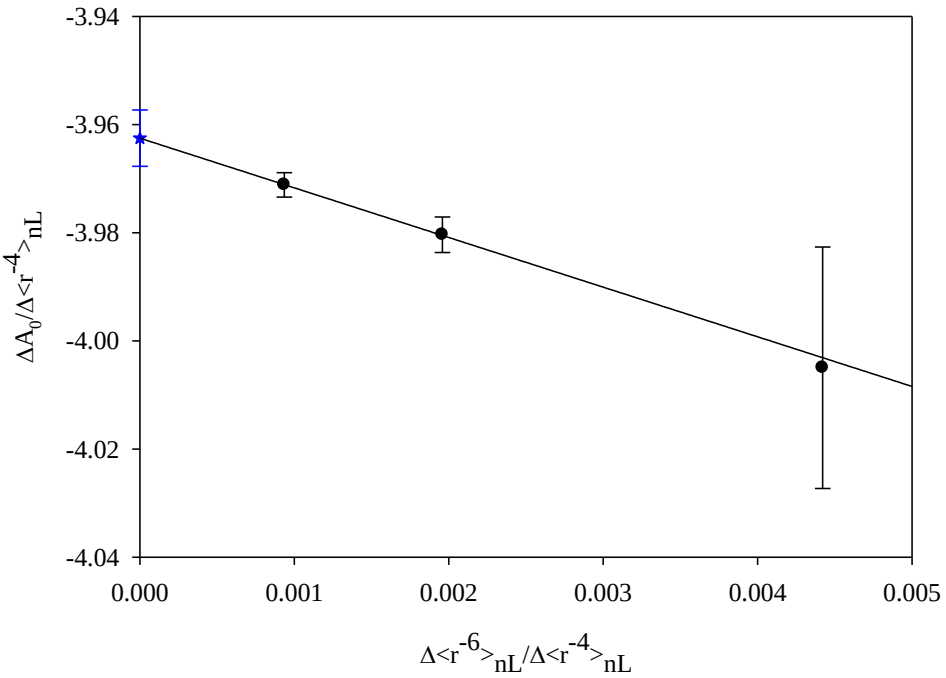

Figure 4.7: Scalar A_0 plot showing the difference in scalar structure parameters on the y-axis and the difference of the expectation values of the inverse sixth power of the Rydberg radial coordinate on the x-axis, both divided by the difference in the expectation value of the inverse fourth power. The data points are shown by the black circles. A linear fit results in the line shown, where the intercept is shown by the blue star. The intercept gives information about the scalar dipole polarizability while the slope gives information about the scalar quadrupole polarizability.

Table 4.8: A_0 plot values. Column 1 gives the upper and lower Ls. Column 2 gives the difference in the inverse sixth power of the Rydberg radial coordinate divided by the inverse fourth power. Column 3 gives the difference in the scalar structure parameter divided by the inverse fourth power of r. Column 4 gives the uncertainty on the difference in scalar structure parameters divided by the inverse fourth power of r. All values are in atomic units (a.u.).

ΔL	$\Delta\langle r^{-6}\rangle_{nL} / \Delta\langle r^{-4}\rangle_{nL}$	$\Delta A_0 / \Delta\langle r^{-4}\rangle_{nL}$	$\sigma / \Delta\langle r^{-4}\rangle_{nL}$
6-5	4.421004 x10^{-03}	-4.005	0.022
7-6	1.959594 x10^{-03}	-3.9805	0.0032
8-7	0.935261 x10^{-03}	-3.9713	0.0022

Relating these results to the effective potential gives a value for the scalar dipole polarizability

$$\alpha_{D,0} = -2B_0^4 = 7.925(10)\,\text{a.u.} \tag{4.12}$$

The slope B_0^6 is related to the adiabatic scalar quadrupole polarizability $\alpha_{Q,0}$ (Eq. 4.13) and the nonadiabatic scalar dipole polarizability $\beta_{D,0}$ (Eq. 2.45)

$$\alpha_{Q,0} = -2B_0^6 + 6\beta_{D,0} = 18(6) + 6\beta_{D,0}\,. \tag{4.13}$$

The value of $\beta_{D,0}$ is related to the same dipole matrix elements that give $\alpha_{D,0}$ (Eq. 2.42), but contains an *additional* power of the excitation energy in its denominator. Reference [42] calculates partial values of $\alpha_{D,0}$ or $\beta_{D,0}$ using the following excitations

$$\begin{aligned} &3d \to 4p + 5p \\ &3d \to 4f + 5f + 6f\,, \\ &3p \to 3d \end{aligned}$$

thus giving the partial values for these two core properties:

$$\begin{aligned} \alpha_{D,0}\,(\text{partial}) &= 4.829\ \text{a.u.} \\ \beta_{D,0}\,(\text{partial}) &= 7.714\ \text{a.u.} \end{aligned}\,. \tag{4.14}$$

The remainder of the calculated $\alpha_{D,0}$ is due primarily to higher f levels, including the continuum [42]:

$$\alpha_{D,0}\,(\text{remainder}) = 2.91\,\text{a.u.} \tag{4.15}$$

Equation 4.15 thus places a limit on the remaining portion of $\beta_{D,0}$ not calculated by Ref. [42],

$$\beta_{D,0}\,(\text{remainder}) \le \frac{2.91}{2 * \Delta E_{\text{lower}}}\,,$$

where ΔE_{lower} is the lowest energy of a state included in the calculation of $\alpha_{D,0}\,(\text{remainder})$. The lowest $3d \to 7f$ state has an energy of 137,519.23 cm^{-1} [41] (or 0.6266 a.u.), resulting in

$$\begin{aligned} \beta_{D,0}\left(\text{remainder}\right) &\le 2.32 \text{ a.u.} \\ \Rightarrow \beta_{D,0}\left(\text{remainder}\right) &\approx 1.2\left(1.2\right) \text{ a.u.} \end{aligned} . \tag{4.16}$$

Combining this estimate with Eq. 4.14 gives a total estimation of $\beta_{D,0}$,

$$\beta_{D,0} = 8.9\left(1.2\right) \text{ a.u.} \tag{4.17}$$

and leads to a determination of $\alpha_{Q,0}$,

$$\alpha_{Q,0} = 71\left(9\right) \text{ a.u.} \tag{4.18}$$

In addition to the scalar term, the tensor term also dominates the energy level pattern. The A_2 plot is shown in Fig. 4.8 and its values are shown in Table 4.9. The uncertainty in each $A_2\left(L\right)$ is uncorrelated since each one is due primarily to different transitions. The structure parameter plot, referring to Eqs. 2.13 and 2.56, is fit to

$$\frac{A_2\left(nL\right)}{\left\langle r^{-3}\right\rangle_{nL}} = B_2^3 + B_2^4 \frac{\left\langle r^{-4}\right\rangle_{nL}}{\left\langle r^{-3}\right\rangle_{nL}} + B_2^6 \frac{\left\langle r^{-6}\right\rangle_{nL}}{\left\langle r^{-3}\right\rangle_{nL}}, \tag{4.19}$$

where the $\left\langle r^{-6}\right\rangle_{nL} \Big/ \left\langle r^{-3}\right\rangle_{nL}$ term allows for a slight curvature to the data. The result of this fit is

$$\begin{aligned} B_2^3 &= 0.4705\left(2\right) \\ B_2^4 &= -0.522\left(16\right) \\ B_2^6 &= 22\left(6\right) \end{aligned} . \tag{4.20}$$

Relating this to V_{eff} gives the quadrupole moment (Eq. 2.14) and the adiabatic tensor dipole polarizability (Eq. 2.57):

$$\begin{aligned} Q &= -B_2^3 = -0.4705\left(2\right) \\ \alpha_{D,2} &= -2B_2^4 = 1.043\left(33\right) \end{aligned} . \tag{4.21}$$

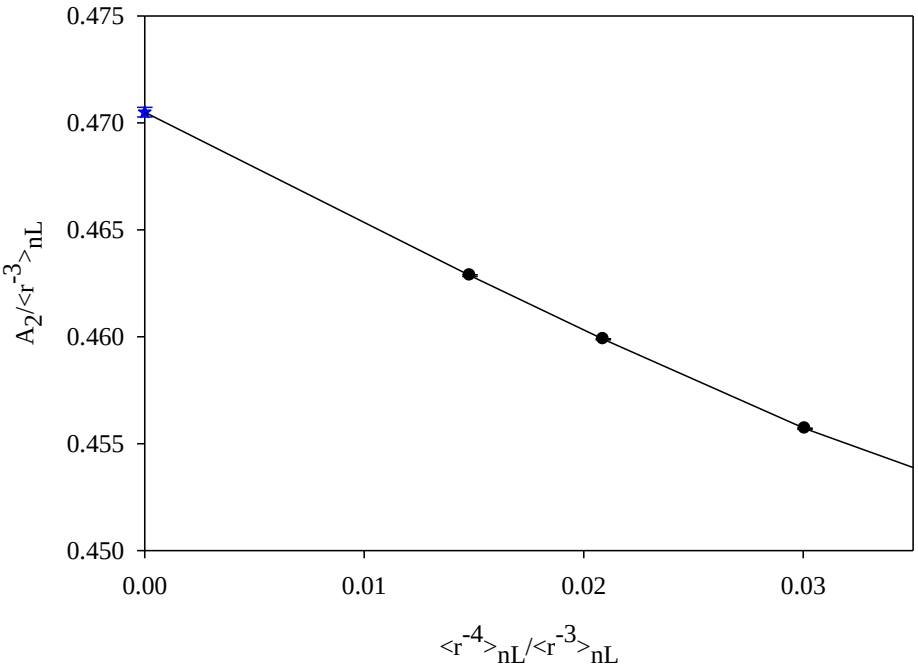

Figure 4.8: Tensor A_2 plot showing the tensor structure parameter on the y-axis and the inverse fourth power of the Rydberg radial coordinate on the x-axis, both divided by the inverse third power. The data points are shown by the black points. The line shows a fit allowing for an inverse sixth power term, where the intercept is shown by the blue star. The intercept gives information about the quadrupole moment while the initial slope gives information about the tensor dipole polarizability.

Table 4.9: A_2 plot values. Column 1 gives the L. Column 2 gives the inverse fourth power of the Rydberg radial coordinate divided by the inverse third power. Column 3 gives the inverse sixth power of r divided by in the inverse third power. Column 4 gives the tensor structure parameter divided by the inverse third power of r. Column 5 gives the uncertainty divided by the inverse third power of r. All values are in atomic units (a.u.).

L	$\langle r^{-4}\rangle_{nL} / \langle r^{-3}\rangle_{nL}$	$\langle r^{-6}\rangle_{nL} / \langle r^{-3}\rangle_{nL}$	$A_2 / \langle r^{-3}\rangle_{nL}$	$\sigma / \langle r^{-3}\rangle_{nL}$
6	30.0783 x10^{-03}	40.64306 x10^{-06}	455715 x10^{-06}	24 x10^{-06}
7	20.8925 x10^{-03}	12.78977 x10^{-06}	459894 x10^{-06}	26 x10^{-06}
8	14.8147 x10^{-03}	4.01964 x10^{-06}	462872 x10^{-06}	38 x10^{-06}

Although the other tensor orders (vector, third-rank, and fourth-rank) are small, they display the complexity of the nickel ion and the power of the improved precision of the microwave RESIS technique over the optical RESIS technique. The vector structure parameter, which depends on Eqs. 2.95 and 2.48, is scaled by $\left\langle r^{-3}\right\rangle_{nL}$,

$$\frac{A_1(nL)}{\left\langle r^{-3}\right\rangle_{nL}} = B_1^3 + B_1^6 \frac{\left\langle r^{-6}\right\rangle_{nL}}{\left\langle r^{-3}\right\rangle_{nL}} + B_1^8 \frac{\left\langle r^{-8}\right\rangle_{nL}}{\left\langle r^{-3}\right\rangle_{nL}}. \tag{4.22}$$

In the optical RESIS study, the vector term was assumed to be entirely due to the permanent magnetic vector term and calculated using the theoretical value of 6/5 for the core's *g*-value [38]. The derivation of the theory in Chapter 2, however, shows the possibility of electric vector terms due to the nonadiabatic response of the core to the electric field of the Rydberg electron. The A_1 plot, shown in Fig. 4.9 with values in Table 4.10, demonstrates the importance of these terms although no predictions exist. A fit of the data where the core's *g*-value has been fixed to the theoretical value gives

$$\begin{aligned} B_1^3 &\equiv \text{-}3.1950\times10^{-5} \\ B_1^6 &= 1.70(40) \\ B_1^8 &= -616(201) \end{aligned} \quad . \tag{4.23}$$

Once again these results may be compared to the effective potential to determine the core properties, in this case the "vector hyperpolarizability" (Eq. 2.51) using the slope:

$$\beta_{D,1} = B_1^6 = 1.70(40). \tag{4.24}$$

Here it is interesting to note that vector hyperpolarizability is not a small correction to the magnetic vector term, which was the case for neon [4] and argon [5].

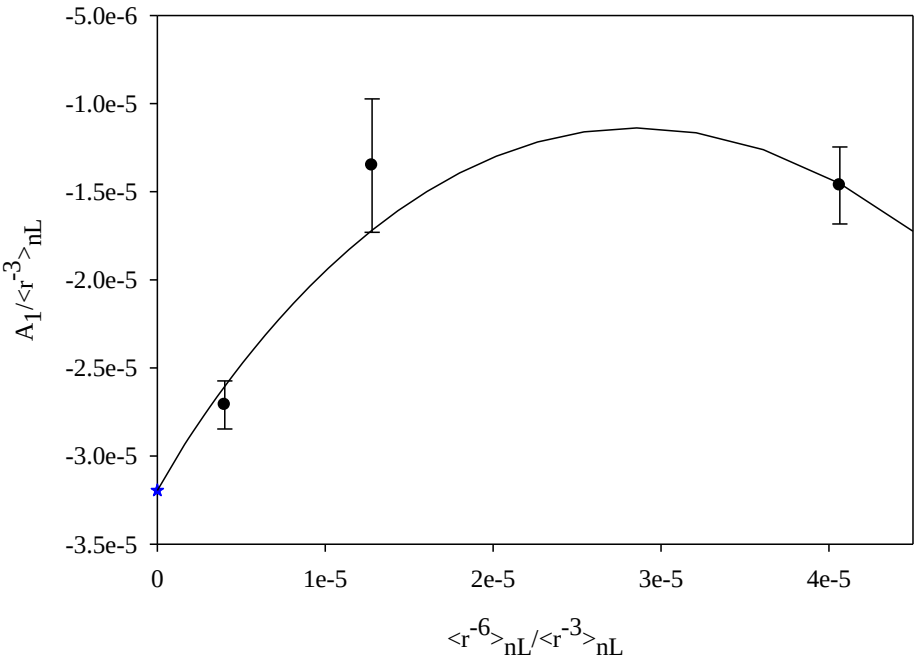

Figure 4.9: Vector A_1 plot showing the vector structure parameter on the y-axis and the inverse sixth power of the Rydberg radial coordinate on the x-axis, both divided by the inverse third power. The data points are shown by the black circles. The line shows a fit allowing for a term proportional to the inverse eighth power. Note that the intercept has been fixed to theoretical magnetic vector term with g_J = 6/5.

Table 4.10: A_1 plot values. Column 1 gives the L. Column 2 gives the inverse sixth power of the Rydberg radial coordinate divided by the inverse third power. Column 3 gives the inverse eighth power of r divided by in the inverse third power. Column 4 gives the vector structure parameter divided by the inverse third power of r. Column 5 gives the uncertainty divided by the inverse third power of r. All values are in atomic units (a.u.).

L	$\langle r^{-6}\rangle_{nL} / \langle r^{-3}\rangle_{nL}$	$\langle r^{-8}\rangle_{nL} / \langle r^{-3}\rangle_{nL}$	$A_1 / \langle r^{-3}\rangle_{nL}$	$\sigma / \langle r^{-3}\rangle_{nL}$
6	40.64306 x10^{-06}	83.62610 x10^{-09}	-14.6 x10^{-06}	2.3 x10^{-06}
7	12.78977 x10^{-06}	11.30609 x10^{-09}	-13.5 x10^{-06}	3.8 x10^{-06}
8	4.01964 x10^{-06}	1.50377 x10^{-09}	-27.1 x10^{-06}	1.4 x10^{-06}

The third-rank tensor, or octupole, term represents the possibility of a permanent magnetic octupole moment due to the nickel ion, along with terms due to the nonadiabatic response of the core to the Rydberg electron's electric field. The octupole structure parameter, which depends on Eqs. 2.96 and 2.69, is scaled by $\left\langle r^{-5}\right\rangle_{nL}$,

$$\frac{A_3(nL)}{\left\langle r^{-5}\right\rangle_{nL}} = B_3^5 + B_3^8 \frac{\left\langle r^{-8}\right\rangle_{nL}}{\left\langle r^{-5}\right\rangle_{nL}}, \tag{4.25}$$

and shown in Fig. 4.10 (values in Table 4.11). Each L shows significant nonzero octupole structure. A linear fit of the data gives

$$\begin{aligned} B_3^5 &= \text{-}0.346(57) \\ B_3^8 &= 3748(861) \end{aligned}. \tag{4.26}$$

The intercept apparently gives information about the magnetic octupole moment, although no predictions of its value or general form are known.

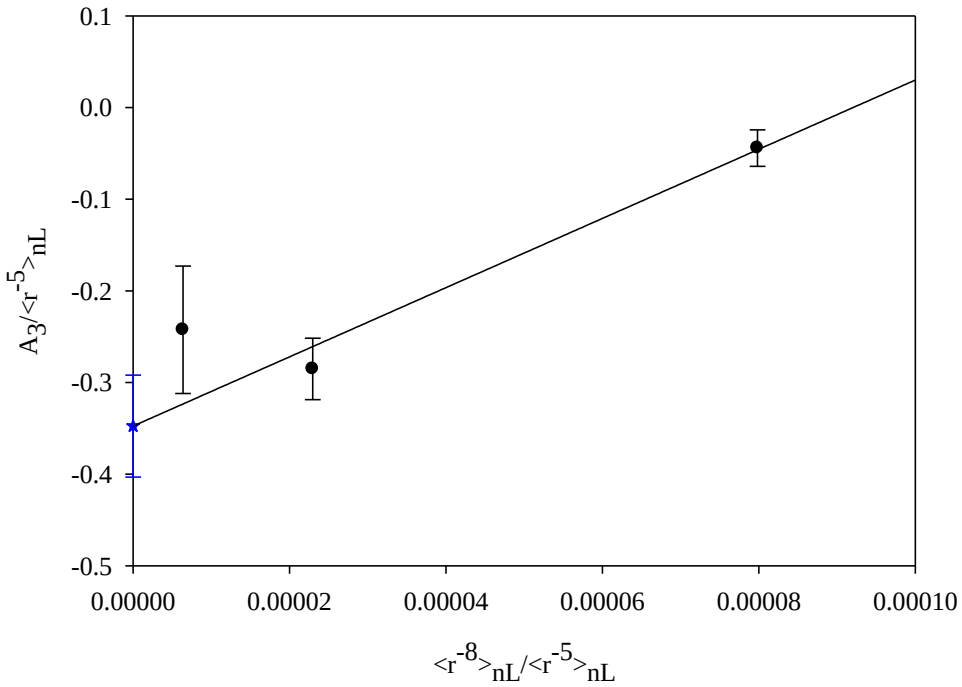

Figure 4.10: Third-rank tensor A_3 plot showing the octupole structure parameter on the y-axis and the inverse eighth power of the Rydberg radial coordinate on the x-axis, both divided by the inverse fifth power. A linear fit gives the line shown, where the intercept is shown by the blue star.

Table 4.11: A_3 plot values. Column 1 gives the L. Column 2 gives the inverse eighth power of the Rydberg radial coordinate divided by the inverse fifth power. Column 3 gives the third-rank tensor structure parameter divided by the inverse fifth power of r. Column 4 gives the uncertainty divided by the inverse fifth power of r. All values are in atomic units (a.u.).

L	$\langle r^{-8}\rangle_{nL} / \langle r^{-5}\rangle_{nL}$	$A_3 / \langle r^{-5}\rangle_{nL}$	$\sigma / \langle r^{-5}\rangle_{nL}$
6	79.83457 x10^{-06}	-0.044	0.023
7	22.96069 x10^{-06}	-0.285	0.035
8	6.39489 x10^{-06}	-0.243	0.069

The fourth-rank tensor term features the possibility of a permanent hexadecapole moment of the ion core. Referring to Eqs. 2.13 and 2.74, the structure parameter is scaled by $\left\langle r^{-5}\right\rangle_{nL}$ (Table 4.12),

$$\frac{A_4(nL)}{\left\langle r^{-5}\right\rangle_{nL}} = B_4^5 + B_4^6 \frac{\left\langle r^{-8}\right\rangle_{nL}}{\left\langle r^{-5}\right\rangle_{nL}}. \tag{4.27}$$

The result, shown in Fig. 4.11, is

$$\begin{aligned} B_4^5 &= \text{-}0.266(85) \\ B_4^6 &= \text{-}0.2(2.3) \end{aligned}, \tag{4.28}$$

where the error bars on the fit parameters have been expanded to reflect the poor quality of the fit. The intercept can be related to the effective potential to give the hexadecapole momentum (Eq. 2.15):

$$\Pi = -B_4^5 = 0.27(9). \tag{4.29}$$

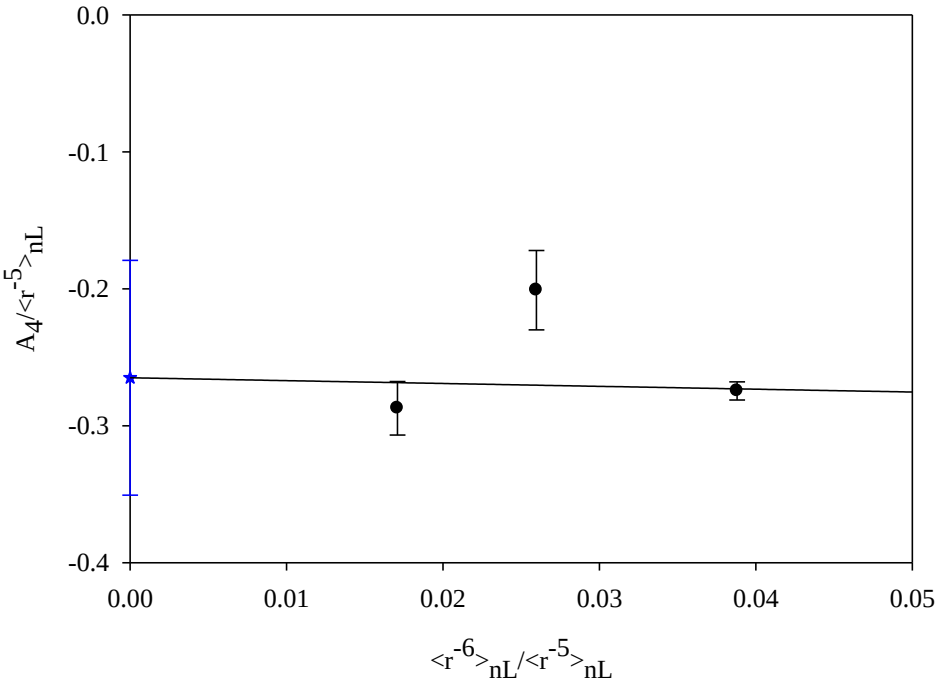

Figure 4.11: Fourth-rank A_4 plot showing the fourth-rank tensor structure parameter on the y-axis and the inverse sixth power of the Rydberg radial coordinate on the x-axis, both divided by the inverse fifth power. The data points are shown by the black circles. The line is the result of a linear fit whose intercept is shown by the blue star.

Table 4.12: A_4 plot values. Column 1 gives the L. Column 2 gives the inverse sixth power of the Rydberg radial coordinate divided by the inverse fifth power. Column 3 gives the fourth-rank tensor structure parameter divided by the inverse fifth power of r. Column 4 gives the uncertainty divided by the inverse fifth power of r. All values are in atomic units (a.u.).

L	$\langle r^{-6}\rangle_{nL} / \langle r^{-5}\rangle_{nL}$	$A_4 / \langle r^{-5}\rangle_{nL}$	$\sigma / \langle r^{-5}\rangle_{nL}$
6	38.8003 x10^{-03}	-0.2746	0.0070
7	25.9738 x10^{-03}	-0.201	0.029
8	17.0939 x10^{-03}	-0.287	0.020

4.5 Conclusions and Future Work

In summary, the $n = 9$ Rydberg fine structure of nickel has been measured and applying the effective potential model of Chapter 2 resulted in the extraction of core properties. Table 4.13 shows the improved precision of the results of the microwave RESIS study as compared to the optical RESIS study. Theoretical estimates of some of the measured properties are available. The hexadecapole moment is within experimental uncertainty while the quadrupole moment and scalar dipole polarizability agree within a couple of percent and the tensor dipole polarizability within roughly ten percent.

Table 4.13: Current results compared to previous measurements and theory. Column 1 gives the property. Column 2 gives the results of this work while column 3 gives the results of Ref. [38]. The theoretical numbers are from Ref. [42] (denoted with [a]) and Ref. [43] ([b] and [c] indicate different methods of calculation). Note that the result for the hexadecapole moment of Ref. [38] had a different sign because V_{eff} was defined differently. All values are in atomic units (a.u.).

Property	microwave RESIS	optical RESIS	theory	
Q	-0.4705(2)	-0.474(2)	-0.476[a]	
Π	0.27(9)	0.33(21)	0.285[a]	
$\alpha_{D,0}$	7.925(10)	7.92(6)	7.9473[b]	7.7782[c]
$\alpha_{D,2}$	1.043(33)	1.15(14)	0.728[b]	0.962[c]
$\alpha_{Q,0}$	71(9)	—	—	
C_{M3}	-0.346(57)	—	—	

As Ref. [1] explains, there have been many measurements of scalar dipole polarizabilities $(\alpha_{D,0})$, but very few measurements of quadrupole moments (Q) or tensor dipole polarizabilities $(\alpha_{D,2})$. The results for the hexadecapole moment (Π) and magnetic octupole term (C_{M3}), on the other hand, represent the first known instance of these properties being measured.

Both the experimental measurements and their analysis are open to improvements. Due to limitations of the RF region, the relative positions of only five out of six energy levels for three different *L*s could be measured. Building a new RF region with a higher frequency range would allow one to measure transitions to the 6^{th} energy level for each *L* and complete the pattern. On the other hand, measuring the $n = 10$ Rydberg fine structure could give information about the energy levels of four different *L*s which would add an additional point of data to each A_b plot. A better estimate or measurement of the off-diagonal tensor dipole polarizability presents perhaps the largest opportunity for improvement over the current analysis. The current estimate for $\alpha_{D,2}\left(J_c'\right)$ results in uncertainties on the second-order energies that are generally greater than the measurement uncertainties and in some cases more than an order of magnitude larger.

Chapter 5: Summary

The work reported here advances both the theory of high-L Rydberg structure and the experimental measurements of such structure. The explicit derivation of the effective potential model in Chapter 2 clarifies the origins and limitations of that picture of high-L Rydberg structure. It should provide a convenient framework for interpreting future measurements in a wide variety of Rydberg atoms and ions. Its primary limitation is for core ions with very low-lying excited levels, where the adiabatic expansion is not convergent. Even in that case, the explicit derivation provides guidance towards exceptional methods that can account for strong nonadiabatic effects.

The experimental measurements of the $n = 9$ fine structure in nickel reveal the most complex Rydberg fine structure studied to date. In addition to providing measurements of the leading core properties such as quadrupole and hexadecapole electric moments and dipole and quadrupole polarizabilities, the measurements provide evidence for significant odd-order tensor structure. The nonadiabatic vector structure is much larger than was observed in previous studies, and shows clear evidence of both r^{-6} and r^{-8} contributions. The leading third-order structure is consistent with effects of a permanent magnetic octupole moment of the Ni^{+} ion, a property that is well known in nuclear studies but has not been previously considered in atoms and ions. Additional nonadiabatic third-order electric structure is also evident. Only a very limited number of theoretical predictions are presently available for these core properties, but future calculations can now be clearly tested against these benchmarks.

References

[1] Stephen R. Lundeen, in *Advances in Atomic, Molecular, and Optical Physics*, edited by P.R. Berman and C.C. Lin (Academic Press, New York, 2005), Vol. 52, pp. 161-208.

[2] K. Bockasten, Phys. Rev. A **9**, 1087 (1974).

[3] T.F. Gallagher, Rydberg Atoms, (Cambridge University Press, Cambridge, 1994).

[4] R.F. Ward, Jr.,W.G. Sturrus, and S.R. Lundeen, Phys. Rev. A **53**, 113 (1996).

[5] M.E. Hanni, J.A. Keele, S.R. Lundeen, and W.G. Sturrus, Phys. Rev. A **78**, 062510 (2008).

[6] Robert D. Cowan, *The Theory of Atomic Structure and Spectra* (University of California Press, Berkeley, CA, 1981).

[7] J.E. Mayer and M.G. Mayer, Phys. Rev. **43**, 605 (1933).

[8] E.A. Hessels, W.G. Sturrus, S.R. Lundeen, D.R. Cok, Phys. Rev. A **35**, 4489 (1987).

[9] H. Eissa and U. Opik, Proc. Phys. Soc. Lon. **92**, 556 (1967).

[10] T.F. Gallagher, R. Kachru, and N.H. Tran, Phys. Rev. A **26**, 2611 (1982).

[11] C.J. Kleinman, Y. Hahn, and L. Spruch, Phys. Rev. **165**, 53 (1968).

[12] R.J. Drachman, Phys. Rev. A **26**, 1228, (1982).

[13] R.J. Drachman, Phys. Rev. A **31**, 1253 (1985).

[14] R.J. Drachman, Phys. Rev. A **47**, 694 (1993).

[15] G.W.F. Drake, Phys. Rev. Lett. **65**, 2769 (1990).

[16] E.A. Hessels, P.W. Arcuni, F.J. Deck, and S.R. Lundeen, Phys. Rev. A **46**, 2622 (1992).

[17] G.D. Stevens and S.R. Lundeen, Phys. Rev. A **60**, 4379 (1999).

[18] W. Clark, C.H. Greene, and G. Miecznik, Phys. Rev. A **53**, 2248 (1996).

[19] A.R. Edmonds, *Angular Momentum in Quantum Mechanics*, Princeton Univ. Press (1957).

[20] M. Sato, Progr. Theor. Phys. **13**, 380 (1955).

[21] B. Zygelman, Phys. Rev. Lett. **64**, 256 (1990).

[22] J.R.P. Angel and P.G.H. Sandars, Proc. Roy. Soc. A. **305**, 125 (1968).

[23] A. Dalgarno and J.T. Lewis, Proc. R. Soc. A 233, **70** (1955).

[24] R.A. Komara, W.G. Sturrus, D.H. Pollack, and W.R. Cochran, Phys. Rev. A **59**, 251 (1999).

[25] G.W.F. Drake and R.A. Swainson, Phys. Rev. A **44**, 5448 (1991).

[26] E.L. Snow and S.R. Lundeen, Phys. Rev. A **76**, 052505 (2007).

[27] E.L. Snow and S.R. Lundeen, Phys. Rev. A **75**, 062512 (2007).

[28] J.A. Keele, S.R. Lundeen, and C.W. Fehrenbach, Phys. Rev. A **83**, 062509 (2011).

[29] E.L Snow, R.A. Komara, M.A. Gearba, and S.R. Lundeen, Phys. Rev. A **68**, 022510 (2003).

[30] E.S. Shuman and T.F. Gallagher, Phys. Rev. A **74**, 022502 (2006).

[31] S.L. Woods, S.R. Lundeen, and E.L. Snow, Phys. Rev. A **80**, 042516 (2009).

[32] S.L. Woods, M.E. Hanni, S.R. Lundeen, and E.L. Snow, Phys. Rev. A **8**2, 012506 (2010).

[33] M.E. Hanni, J.A. Keele, S.R. Lundeen, C.W. Fehrenbach, and W.G. Sturrus, Phys. Rev. A **81**, 042512 (2010).

[34] M.S. Safronova, M.G. Kozlov, and U.I. Safronova, Phys. Rev. A **85**, 012507 (2012).

[35] Beam Imaging Solutions, *Model RFIS-100 RF Ion Source User's Manual*, Rev. 4 (July 2011).

[36] C.W. Fehrenbach, S.R. Lundeen, and O.L. Weaver, Phys, Rev. A **51**, R910 (1995).

[37] D.S. Fisher, Ph.D. Dissertation, Colorado State University (2000).

[38] J.A. Keele, S.L. Woods, M.E. Hanni, S.R. Lundeen, and W.G. Sturrus, Phys. Rev. A **81**, 022506 (2010).

[39] *Reference Data for Engineers: Radio, Electronics, Computer and Communications*, 8th ed., edited by M. E. Van Valkenburg (SAMS, Indianapolis, 1995).

[40] R.L. Kurucz and B. Bell, Atomic Line List from KURUCZ CD-ROM NO. 23 (1995). Available: http://www.pmp.uni-hannover.de/cgi-bin/ssi/test/kurucz/sekur.html. [2012].

[41] Yu. Ralchenko, A.E. Kramida, J. Reader, and NIST ASD Team (2011). NIST Atomic Spectra Database (ver. 4.1.0), [Online]. Available: http://physics.nist.gov/asd. [2012]. National Institute of Standards and Technology, Gaithersburg, MD.

[42] D.R. Beck (private communication).

[43] D.R. Beck and L. Pan, J Phys B **43**, 074009 (2010).

[44] Albert Messiah, *Quantum Mechanics* (Dover Publications, 1999), p.484.

Appendix A: Derivation of First and Second Nonadiabatic Terms

The derivation of the 1st and 2nd nonadiabatic terms both begin with the radial wave equation satisfied by the Rydberg radial wave function,

$$\left(\frac{1}{Q}\right)^2\left[\frac{d^2}{dr^2}+\frac{2Q}{r}-\frac{L(L+1)}{r^2}\right]P_{nL}=\frac{1}{n^2}P_{nL}, \tag{A.1}$$

and the following term

$$-\left(\frac{1}{n'^2}-\frac{1}{n^2}\right)\left\langle nL\,|\,r^{-s}\,|\,n'L'\right\rangle. \tag{A.2}$$

Substitution of the radial wave equation into it gives

$$\begin{aligned}&-\left(\frac{1}{n'^2}-\frac{1}{n^2}\right)\left\langle nL\,|\,r^{-s}\,|\,n'L'\right\rangle\\&=-\left(\frac{1}{Q}\right)^2\int_0^\infty P_{nL}r^{-s}\frac{d^2P_{n'L'}}{dr^2}dr+\left(\frac{1}{Q}\right)^2\int_0^\infty\frac{d^2P_{nL}}{dr^2}r^{-s}P_{n'L'}dr-\left(\frac{1}{Q}\right)^2\left[-L'\left(L'+1\right)+L\left(L+1\right)\right]\int_0^\infty P_{nL}r^{-(s+2)}P_{n'L'}dr\end{aligned}. \tag{A.3}$$

Integration by parts is performed on the first term:

$$\boxed{\begin{aligned}&\frac{dv}{dr}=\frac{d^2P_{nL}}{dr^2}\quad\text{and}\quad u=r^{-s}P_{n'L'}\\&\Rightarrow v=\frac{dP_{nL}}{dr}\quad\text{and}\quad\frac{du}{dr}=-s\cdot r^{-(s+1)}P_{n'L'}+r^{-s}\frac{dP_{n'L'}}{dr}\end{aligned}}$$

$$\int\frac{d^2P_{nL}}{dr^2}r^{-s}P_{n'L'}dr=0-\int\frac{dP_{nL}}{dr}\left(-s\cdot r^{-(s+1)}P_{n'L'}+r^{-s}\frac{dP_{n'L'}}{dr}\right)dr$$

$$\boxed{\begin{aligned}&\frac{dv}{dr}=\frac{dP_{nL}}{dr}\quad\text{and}\quad u=-s\cdot r^{-(s+1)}P_{n'L'}+r^{-s}\frac{dP_{n'L'}}{dr}\\&\Rightarrow v=P_{nL}\quad\text{and}\quad\frac{du}{dr}=s(s+1)\cdot r^{-(s+2)}P_{n'L'}-2s\cdot r^{-(s+1)}\frac{dP_{n'L'}}{dr}+r^{-s}\frac{d^2P_{n'L'}}{dr^2}\end{aligned}}\qquad\text{. (A.4)}$$

$$\begin{aligned}\int\frac{d^2P_{nL}}{dr^2}r^{-s}P_{n'L'}dr&=0-\left(0-\int P_{nL}\left(s(s+1)\cdot r^{-(s+2)}P_{n'L'}-2s\cdot r^{-(s+1)}\frac{dP_{n'L'}}{dr}+r^{-s}\frac{d^2P_{n'L'}}{dr^2}\right)dr\right)\\&=\int P_{nL}\left(s(s+1)\cdot r^{-(s+2)}P_{n'L'}-2s\cdot r^{-(s+1)}\frac{dP_{n'L'}}{dr}+r^{-s}\frac{d^2P_{n'L'}}{dr^2}\right)dr\end{aligned}$$

It is substituted back in to give

$$\begin{aligned}&-\left(\frac{1}{n'^2}-\frac{1}{n^2}\right)\langle nL\,|\,r^{-s}\,|\,n'L'\rangle\\&=2s\left(\frac{1}{Q}\right)^2\int\frac{dP_{nL}}{dr}r^{-(s+1)}P_{n'L'}dr+\left(\frac{1}{Q}\right)^2\left[-s(s+1)-L(L+1)+L'(L'+1)\right]\int P_{nL}r^{-(s+2)}P_{n'L'}dr\end{aligned}\qquad\text{.(A.5)}$$

It is assumed that the Rydberg radial wave function goes to zero at $r = 0$ and $r = \infty$, thus placing a constraint on the possible values of L.

A.1 First Nonadiabatic Term

The 1st nonadiabatic term is found by multiplying Eq. A.5 by $\langle n'L'\,|\,r^{-q}\,|\,nL\rangle$ and summing over n':

$$\sum_{n'} -\left(\frac{1}{n'^2}-\frac{1}{n^2}\right)\left\langle nL\,|\,r_1^{-s}\,|\,n'L'\right\rangle\left\langle n'L'\,|\,r_2^{-q}\,|\,nL\right\rangle$$
$$=\sum_{n'} 2s\left(\frac{1}{Q}\right)^2\int\frac{dP_{nL}}{dr_1}r_1^{-(s+1)}P_{n'L'}dr_1\cdot\int P_{n'L'}r_2^{-q}P_{nL}dr_2 \qquad . \qquad \text{(A.6)}$$
$$+\sum_{n'}\left[-s(s+1)-L(L+1)+L'(L'+1)\right]\left(\frac{1}{Q}\right)^2\int P_{nL}r_1^{-(s+2)}P_{n'L'}dr_1\cdot\int P_{n'L'}r_2^{-q}P_{nL}dr_2$$

The completeness relation,

$$\sum_{n'} P_{n'L'}(r_1)\cdot P_{n'L'}(r_2)=\delta(r_1-r_2), \qquad \text{(A.7)}$$

can be used to give the following

$$\sum_{n'} -\left(\frac{1}{n'^2}-\frac{1}{n^2}\right)\left\langle nL\,|\,r^{-s}\,|\,n'L'\right\rangle\left\langle n'L'\,|\,r^{-q}\,|\,nL\right\rangle$$
$$=2s\left(\frac{1}{Q}\right)^2\int\frac{dP_{nL}}{dr}r^{-(s+q+1)}P_{nL}dr+\left[-s(s+1)-L(L+1)+L'(L'+1)\right]\left(\frac{1}{Q}\right)^2\int P_{nL}r^{-(s+q+2)}P_{nL}dr \qquad .$$
$$\text{(A.8)}$$

Once again integration by parts can be performed on the first term:

$$\boxed{\begin{aligned}&\frac{dv}{dr}=\frac{dP_{nL}}{dr}\quad\text{and}\quad u=r^{-(s+q+1)}P_{nL}\\&\Rightarrow v=P_{nL}\quad\text{and}\quad\frac{du}{dr}=-(s+q+1)r^{-(s+q+2)}P_{nL}+r^{-(s+q+1)}\frac{dP_{nL}}{dr}\end{aligned}}$$
$$\int\frac{dP_{nL}}{dr}r^{-(s+q+1)}P_{nL}dr=0-\int P_{nL}\left(-(s+q+1)r^{-(s+q+2)}P_{nL}+r^{-(s+q+1)}\frac{dP_{nL}}{dr}\right)dr\,. \qquad \text{(A.9)}$$
$$=\frac{1}{2}(s+q+1)\int P_{nL}r^{-(s+q+2)}P_{nL}dr$$

Substituting this and combing terms gives

$$\sum_{n'} -\left(\frac{1}{n'^2}-\frac{1}{n^2}\right)\left\langle nL\,|\,r^{-s}\,|\,n'L'\right\rangle\left\langle n'L'\,|\,r^{-q}\,|\,nL\right\rangle$$
$$=\left[s(s+q+1)-s(s+1)-L(L+1)+L'(L'+1)\right]\left(\frac{1}{Q}\right)^2\int P_{nL}r^{-(s+q+2)}P_{nL}dr \qquad \text{(A.10)}$$

which leads to the final form of the 1st nonadiabatic term:

$$\begin{aligned}&\sum_{n'}\left(E(n')-E(n)\right)\left\langle nL\,|\,r^{-s}\,|\,n'L'\right\rangle\left\langle n'L'\,|\,r^{-q}\,|\,nL\right\rangle \\ &=\frac{1}{2}\left[sq-L(L+1)+L'(L'+1)\right]\left\langle r^{-(s+q+2)}\right\rangle_{nL}\end{aligned}\quad . \tag{A.11}$$

A.2 Second Nonadiabatic Term

The 2nd nonadiabatic term begins by writing Eq. A.5 with -*s* as the power of *r* and again with -*q* as the power of *r*,

$$\begin{aligned}&-\left(\frac{1}{n'^2}-\frac{1}{n^2}\right)\left\langle nL\,|\,r^{-s}\,|\,n'L'\right\rangle \\ &=2s\left(\frac{1}{Q}\right)^2\int\frac{dP_{nL}}{dr}r^{-(s+1)}P_{n'L'}dr+\left(\frac{1}{Q}\right)^2\left[-s(s+1)-L(L+1)+L'(L'+1)\right]\int P_{nL}r^{-(s+2)}P_{n'L'}dr\end{aligned}$$

and

$$\begin{aligned}&-\left(\frac{1}{n'^2}-\frac{1}{n^2}\right)\left\langle n'L'\,|\,r^{-q}\,|\,nL\right\rangle \\ &=2q\left(\frac{1}{Q}\right)^2\int P_{n'L'}r^{-(q+1)}\frac{dP_{nL}}{dr}dr+\left(\frac{1}{Q}\right)^2\left[-q(q+1)-L(L+1)+L'(L'+1)\right]\int P_{n'L'}r^{-(q+2)}P_{nL}dr\end{aligned}$$

,

(A.12)

and then multiplying them together and summing over n' to give

$$\sum_{n'}\left(\frac{1}{n^2}-\frac{1}{n'^2}\right)^2\left\langle nL\,|\,r_1^{-s}\,|\,n'L'\right\rangle\left\langle n'L'\,|\,r_2^{-q}\,|\,nL\right\rangle$$

$$=\left(\frac{1}{Q}\right)^4\sum_{n'}\left\{\begin{array}{l}\left(2s\int\frac{dP_{nL}}{dr_1}r_1^{-(s+1)}P_{n'L'}dr_1\right)\cdot\left(2q\int P_{n'L'}r_2^{-(q+1)}\frac{dP_{nL}}{dr_2}dr_2\right)\\+\left(2s\int\frac{dP_{nL}}{dr_1}r_1^{-(s+1)}P_{n'L'}dr_1\right)\cdot\left(\left[-q(q+1)-L(L+1)+L'(L'+1)\right]\int P_{n'L'}r_2^{-(q+2)}P_{nL}dr_2\right)\\+\left(\left[-s(s+1)-L(L+1)+L'(L'+1)\right]\int P_{nL}r_1^{-(s+2)}P_{n'L'}dr_1\right)\cdot\left(2q\int P_{n'L'}r_1^{-(q+1)}\frac{dP_{nL}}{dr_2}dr_2\right)\\+\left(\left[-s(s+1)-L(L+1)+L'(L'+1)\right]\int P_{nL}r_1^{-(s+2)}P_{n'L'}dr_1\right)\\\qquad\qquad*\left(\left[-q(q+1)-L(L+1)+L'(L'+1)\right]\int P_{n'L'}r_2^{-(q+2)}P_{nL}dr_2\right)\end{array}\right\}.$$

(A.13)

The completeness relation is used to give

$$\sum_{n'}\left(\frac{1}{n^2}-\frac{1}{n'^2}\right)^2\left\langle nL\,|\,r^{-s}\,|\,n'L'\right\rangle\left\langle n'L'\,|\,r^{-q}\,|\,nL\right\rangle$$

$$=4sq\left(\frac{1}{Q}\right)^4\int r^{-(s+q+2)}\left(\frac{dP_{nL}}{dr}\right)^2dr$$

$$+\left[-4sq+2(s+q)\left(-sq-L(L+1)+L'(L'+1)\right)\right]\left(\frac{1}{Q}\right)^4\int r^{-(s+q+3)}P_{nL}\frac{dP_{nL}}{dr}dr$$

$$+\left[-s(s+1)-L(L+1)+L'(L'+1)\right]\left[-q(q+1)-L(L+1)+L'(L'+1)\right]\left(\frac{1}{Q}\right)^4\int r^{-(s+q+4)}P_{nL}P_{nL}dr$$

(A.14)

Integration by parts is performed on the second integral,

$$\boxed{\begin{aligned}&\frac{dv}{dr}=\frac{dP_{nL}}{dr}\ \text{ and }\ u=r^{-(s+q+3)}P_{nL}\\&\Rightarrow v=P_{nL}\ \text{ and }\ \frac{du}{dr}=-(s+q+3)r^{-(s+q+4)}P_{nL}+r^{-(s+q+3)}\frac{dP_{nL}}{dr}\end{aligned}}$$

$$\int r^{-(s+q+3)}P_{nL}\frac{dP_{nL}}{dr}dr=0-\int P_{nL}\left(-(s+q+3)r^{-(s+q+4)}P_{nL}+r^{-(s+q+3)}\frac{dP_{nL}}{dr}\right)dr, \qquad \text{(A.15)}$$

$$=\frac{1}{2}(s+q+3)\int r^{-(s+q+4)}P_{nL}P_{nL}dr$$

and on the first integral,

$$\boxed{\begin{aligned}&\frac{dv}{dr}=\frac{dP_{nL}}{dr}\ \text{ and }\ u=r^{-(s+q+2)}\frac{dP_{nL}}{dr}\\&\Rightarrow v=P_{nL}\ \text{ and }\ \frac{du}{dr}=-(s+q+2)r^{-(s+q+3)}\frac{dP_{nL}}{dr}+r^{-(s+q+2)}\frac{d^2P_{nL}}{dr^2}\end{aligned}}$$

$$\int r^{-(s+q+2)}\left(\frac{dP_{nL}}{dr}\right)^2dr=0-\int P_{nL}\left(-(s+q+2)r^{-(s+q+3)}\frac{dP_{nL}}{dr}+r^{-(s+q+2)}\frac{d^2P_{nL}}{dr^2}\right)dr$$

$$=(s+q+2)\int P_{nL}r^{-(s+q+3)}\frac{dP_{nL}}{dr}dr-\int P_{nL}r^{-(s+q+2)}\frac{d^2P_{nL}}{dr^2}dr$$

$$\boxed{\begin{aligned}&\frac{dv}{dr}=\frac{dP_{nL}}{dr}\ \text{ and }\ u=r^{-(s+q+3)}P_{nL}\\&\Rightarrow v=P_{nL}\ \text{ and }\ \frac{du}{dr}=-(s+q+3)r^{-(s+q+4)}P_{nL}+r^{-(s+q+3)}\frac{dP_{nL}}{dr}\end{aligned}} \qquad \text{, (A.16)}$$

$$\int P_{nL}r^{-(s+q+3)}\frac{dP_{nL}}{dr}dr=\frac{1}{2}(s+q+3)\int r^{-(s+q+4)}P_{nL}^2dr$$

$$\Rightarrow$$

$$\int r^{-(s+q+2)}\left(\frac{dP_{nL}}{dr}\right)^2dr=\frac{1}{2}(s+q+2)(s+q+3)\int r^{-(s+q+4)}P_{nL}P_{nL}dr-\int r^{-(s+q+2)}\frac{d^2P_{nL}}{dr^2}dr$$

Both are substituted back in to give

$$\begin{aligned}
&\sum_{n'}\left(\frac{1}{n^2}-\frac{1}{n'^2}\right)^2\left\langle nL\,|\,r^{-s}\,|\,n'L'\right\rangle^2 \\
&=-4sq\left(\frac{1}{Q}\right)^4\int r^{-(s+q+2)}\frac{d^2P_{nL}}{dr^2}\,dr \\
&+\left[(s+q+2)sq+(s+q)\left(-L(L+1)+L'(L'+1)\right)\right](s+q+3)\left(\frac{1}{Q}\right)^4\left\langle r^{-(s+q+4)}\right\rangle \\
&+\left[-s(s+1)-L(L+1)+L'(L'+1)\right]\left[-q(q+1)-L(L+1)+L'(L'+1)\right]\left(\frac{1}{Q}\right)^4\left\langle r^{-(s+q+4)}\right\rangle
\end{aligned} \tag{A.17}$$

Focusing on the first term, the second derivative can be replaced using the wave equation,

$$\begin{aligned}
\int r^{-(s+q+2)}\frac{d^2P_{nL}}{dr^2}\,dr &= \int r^{-(s+q+2)}P_{nL}\left[\frac{1}{n^2}-\frac{2}{r}+\frac{L(L+1)}{r^2}\right]P_{nL}\,dr \\
&= \frac{Q^2}{n^2}\left\langle r^{-(s+q+2)}\right\rangle-2Q\left\langle r^{-(s+q+3)}\right\rangle+L(L+1)\left\langle r^{-(s+q+4)}\right\rangle
\end{aligned}, \tag{A.18}$$

to give

$$\begin{aligned}
&\sum_{n'}\left(\frac{1}{n^2}-\frac{1}{n'^2}\right)^2\left\langle nL\,|\,r^{-s}\,|\,n'L'\right\rangle^2 \\
&=4sq\left(\frac{1}{Q}\right)^4\left(-\frac{Q^2}{n^2}\left\langle r^{-(s+q+2)}\right\rangle+2Q\left\langle r^{-(s+q+3)}\right\rangle-L(L+1)\left\langle r^{-(s+q+4)}\right\rangle\right) \\
&+\left[(s+q+2)sq+(s+q)\left(-L(L+1)+L'(L'+1)\right)\right](s+q+3)\left(\frac{1}{Q}\right)^4\left\langle r^{-(s+q+4)}\right\rangle \\
&+\left[-s(s+1)-L(L+1)+L'(L'+1)\right]\left[-q(q+1)-L(L+1)+L'(L'+1)\right]\left(\frac{1}{Q}\right)^4\left\langle r^{-(s+q+4)}\right\rangle
\end{aligned} \tag{A.19}$$

Reference [44] gives the following relation:

$$\frac{t+1}{n^2}\left\langle r^t\right\rangle-(2t+1)\left\langle r^{t-1}\right\rangle+\frac{t}{4}\left((2L+1)^2-t^2\right)\left\langle r^{t-2}\right\rangle=0 \text{ with t} > -(2L+1) \tag{A.20}$$

Substituting –(*s* + *q* + 2) for *t* gives the following

$$-\frac{Q^2}{n^2}\left\langle r^{-(s+q+2)}\right\rangle=\frac{1}{4}\frac{s+q+2}{s+q+1}\left(\left(2L+1\right)^2-\left(s+q+2\right)^2\right)\left\langle r^{-(s+q+4)}\right\rangle-\frac{2s+2q+3}{s+q+1}Q\left\langle r^{-(s+q+3)}\right\rangle \tag{A.21}$$

which can be substituted back into the main formula

$$\begin{aligned}
&\sum_{n'}\left(\frac{1}{n^2}-\frac{1}{n'^2}\right)^2\left\langle nL\left|r^{-s}\right|n'L'\right\rangle^2\\
&=4sq\left(\frac{1}{Q}\right)^4\left(\frac{1}{4}\frac{s+q+2}{s+q+1}\left(\left(2L+1\right)^2-\left(s+q+2\right)^2\right)\left\langle r^{-(s+q+4)}\right\rangle-\frac{2s+2q+3}{s+q+1}Q\left\langle r^{-(s+q+3)}\right\rangle\right)\\
&+4sq\left(\frac{1}{Q}\right)^4\left(2Q\left\langle r^{-(s+q+3)}\right\rangle-L\left(L+1\right)\left\langle r^{-(s+q+4)}\right\rangle\right)\\
&+\left[\left(s+q+2\right)sq+\left(s+q\right)\left(-L(L+1)+L'\left(L'+1\right)\right)\right]\left(s+q+3\right)\left(\frac{1}{Q}\right)^4\left\langle r^{-(s+q+4)}\right\rangle\\
&+\left[-s\left(s+1\right)-L\left(L+1\right)+L'\left(L'+1\right)\right]\left[-q\left(q+1\right)-L\left(L+1\right)+L'\left(L'+1\right)\right]\left(\frac{1}{Q}\right)^4\left\langle r^{-(s+q+4)}\right\rangle
\end{aligned} \tag{A.22}$$

Combining terms gives the final equation for the 2nd nonadiabatic term

$$\begin{aligned}
&\sum_{n'}\left(E\left(n'\right)-E\left(n\right)\right)^2\left\langle nL\left|r^{-s}\right|n'L'\right\rangle^2\\
&=-\frac{sq}{s+q+1}\left(Q\left\langle r^{-(s+q+3)}\right\rangle-L\left(L+1\right)\left\langle r^{-(s+q+4)}\right\rangle\right)\\
&+\frac{1}{4}\left(s+q\right)\left(s+q+3\right)\left(-L(L+1)+L'\left(L'+1\right)\right)\left\langle r^{-(s+q+4)}\right\rangle\\
&+\frac{1}{4}\left[-s\left(s+1\right)-L\left(L+1\right)+L'\left(L'+1\right)\right]\left[-q\left(q+1\right)-L\left(L+1\right)+L'\left(L'+1\right)\right]\left\langle r^{-(s+q+4)}\right\rangle
\end{aligned} \tag{A.23}$$

Appendix B: Calculation of "f functions" for Theoretical Model

Calculation of the functions $f1_b(\kappa_1,\kappa_2)$ (Eq. 2.33), $f2_b(\kappa_1,\kappa_2)$ (Eq. 2.35), $f3_b(\kappa_1,\kappa_2)$ (Eq. 2.37), and $f4_b(\kappa_1,\kappa_2)$ (Eq. 2.38):

SCALAR

$$f1_0(1,1) = -\sqrt{\frac{2L+1}{3}}$$

$$f1_0(2,2) = \sqrt{\frac{2L+1}{5}}$$

$$f1_0(3,3) = -\sqrt{\frac{2L+1}{7}}$$

$$f2_0(1,1) = 3\sqrt{\frac{2L+1}{3}}$$

$$f2_0(2,2) = -\frac{15}{2}\sqrt{\frac{2L+1}{5}}$$

$$f3_0(1,1) = \frac{4}{5}Q\sqrt{\frac{2L+1}{3}}$$

$$f4_0(1,1) = -\frac{9}{5}\left(L(L+1)+10\right)\sqrt{\frac{2L+1}{3}}$$

VECTOR

$$f1_1(1,1) = 0$$

$$f1_1(2,2) = 0$$

$$f2_1(1,1) = \frac{1}{12}\sqrt{6}\sqrt{2L(2L+1)(2L+2)}$$

$$f2_1(2,2) = -\frac{1}{4}\sqrt{\frac{6}{5}}\sqrt{2L(2L+1)(2L+2)}$$

$$f3_1(1,1) = 0$$

$$f4_1(1,1) = -\frac{3}{4}\sqrt{6}\sqrt{2L(2L+1)(2L+2)}$$

TENSOR

$$f1_2(1,1) = -\frac{1}{10}\sqrt{\frac{10}{3}}\sqrt{\frac{2L(2L+1)(2L+2)}{(2L-1)(2L+3)}}$$

$$f1_2(2,2) = \frac{1}{10}\sqrt{\frac{10}{7}}\sqrt{\frac{2L(2L+1)(2L+2)}{(2L-1)(2L+3)}} \qquad f2_2(1,1) = \frac{3}{20}\sqrt{\frac{10}{3}}\sqrt{\frac{2L(2L+1)(2L+2)}{(2L-1)(2L+3)}}$$

$$f1_2(3,3) = -\frac{1}{15}\sqrt{\frac{15}{7}}\sqrt{\frac{2L(2L+1)(2L+2)}{(2L-1)(2L+3)}} \qquad f2_2(2,2) = -\frac{6}{10}\sqrt{\frac{10}{7}}\sqrt{\frac{2L(2L+1)(2L+2)}{(2L-1)(2L+3)}}$$

$$f1_2(1,3) = \frac{1}{10}\sqrt{\frac{15}{7}}\sqrt{\frac{2L(2L+1)(2L+2)}{(2L-1)(2L+3)}} \qquad f2_2(1,3) = -\frac{6}{10}\sqrt{\frac{15}{7}}\sqrt{\frac{2L(2L+1)(2L+2)}{(2L-1)(2L+3)}}$$

$$f1_2(2,4) = -\frac{1}{10}\sqrt{\frac{10}{7}}\sqrt{\frac{2L(2L+1)(2L+2)}{(2L-1)(2L+3)}}$$

$$f3_2(1,1) = \frac{4}{50}\sqrt{\frac{10}{3}}Q\sqrt{\frac{2L(2L+1)(2L+2)}{(2L-1)(2L+3)}}$$

$$f4_2(1,1) = -\frac{9}{50}\sqrt{\frac{10}{3}}\left(L(L+1)+\tfrac{5}{2}\right)\sqrt{\frac{2L(2L+1)(2L+2)}{(2L-1)(2L+3)}}$$

3rd-RANK TENSOR

$$f1_3(2,2) = 0 \qquad f2_3(2,2) = -\frac{3}{4}\frac{1}{\sqrt{70}}\sqrt{\frac{(2L-2)2L(2L+1)(2L+2)(2L+4)}{(2L-1)(2L+3)}}$$

$$f1_3(1,3) = 0 \qquad f2_3(1,3) = -\frac{1}{8}\sqrt{\frac{3}{7}}\sqrt{\frac{(2L-2)2L(2L+1)(2L+2)(2L+4)}{(2L-1)(2L+3)}}$$

4^{th}-RANK TENSOR

$$f1_4(2,2) = \frac{3}{40}\sqrt{\frac{10}{7}}\sqrt{\frac{(2L-2)2L(2L+1)(2L+2)(2L+4)}{(2L-3)(2L-1)(2L+3)(2L+5)}}$$

$$f1_4(2,2) = \frac{3}{40}\sqrt{\frac{10}{7}}\sqrt{\frac{(2L-2)2L(2L+1)(2L+2)(2L+4)}{(2L-3)(2L-1)(2L+3)(2L+5)}}$$

$$f1_4(1,3) = \frac{1}{4}\sqrt{\frac{1}{7}}\sqrt{\frac{(2L-2)2L(2L+1)(2L+2)(2L+4)}{(2L-3)(2L-1)(2L+3)(2L+5)}}$$

$$f1_4(2,4) = -\frac{1}{4}\sqrt{\frac{5}{77}}\sqrt{\frac{(2L-2)2L(2L+1)(2L+2)(2L+4)}{(2L-3)(2L-1)(2L+3)(2L+5)}}$$

$$f2_4(2,2) = -\frac{3}{16}\sqrt{\frac{10}{7}}\sqrt{\frac{(2L-2)2L(2L+1)(2L+2)(2L+4)}{(2L-3)(2L-1)(2L+3)(2L+5)}}$$

$$f2_4(1,3) = -\frac{5}{8}\sqrt{\frac{1}{7}}\sqrt{\frac{(2L-2)2L(2L+1)(2L+2)(2L+4)}{(2L-3)(2L-1)(2L+3)(2L+5)}}$$

Appendix C: Observed Microwave RESIS Transitions

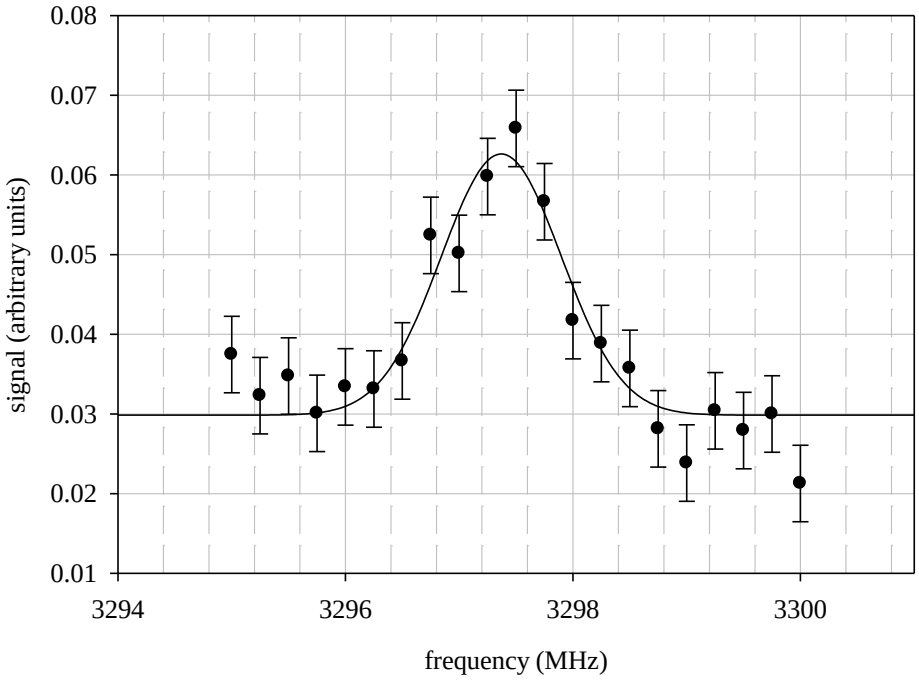

Figure C.1: Ni $9I_{4.5}$ to $9K_{5.5}$ co-propagating. SW06_048

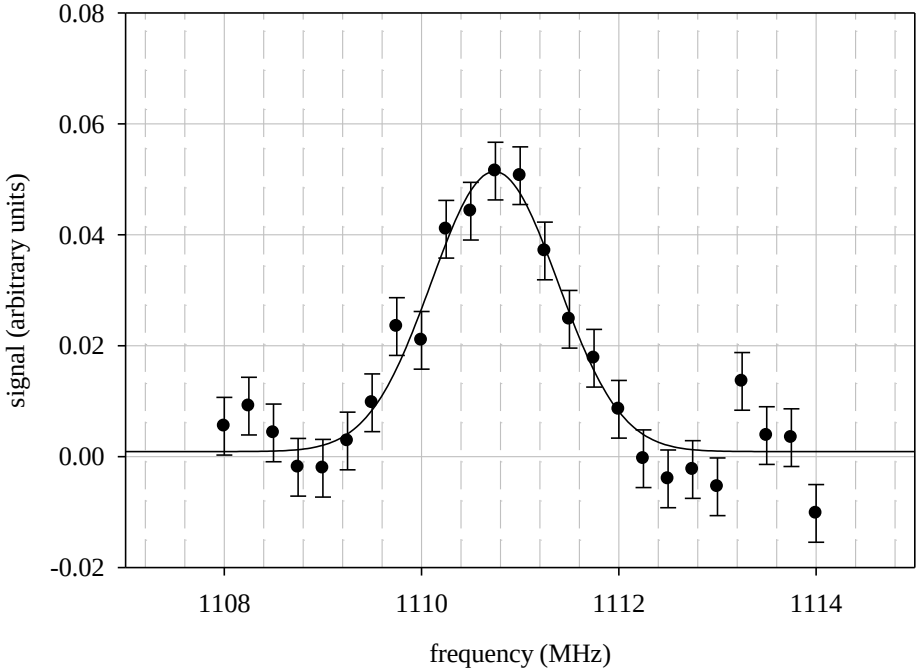

Figure C.2: Ni $9I_{5.5}$ to $9K_{6.5}$ co-propagating. SW06_034

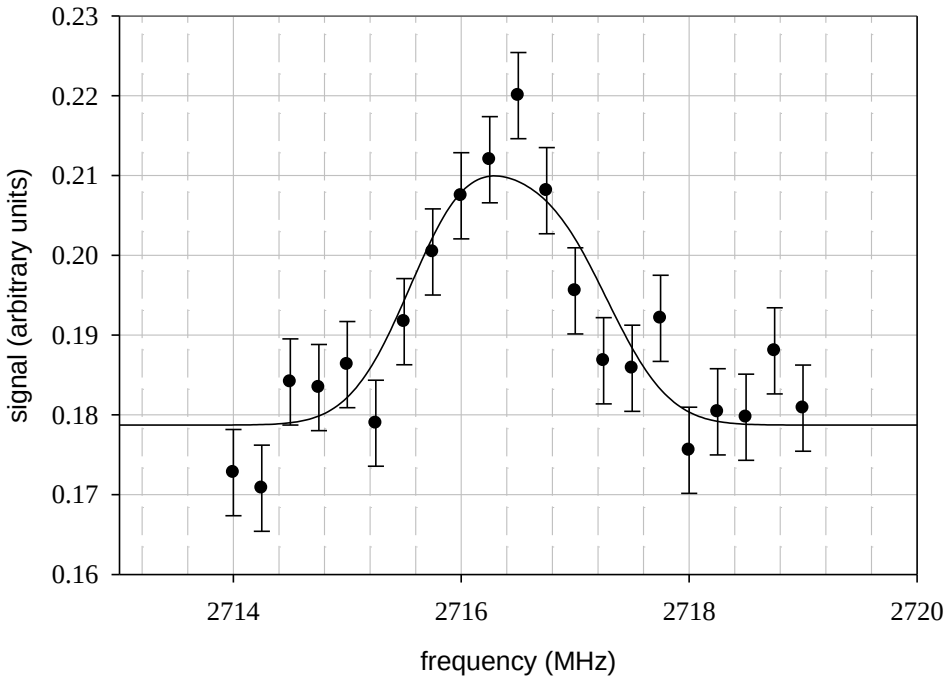

Figure C.3: Ni $9I_{5.5}$ to $9K_{5.5}$ counter-propagating. SW04_046

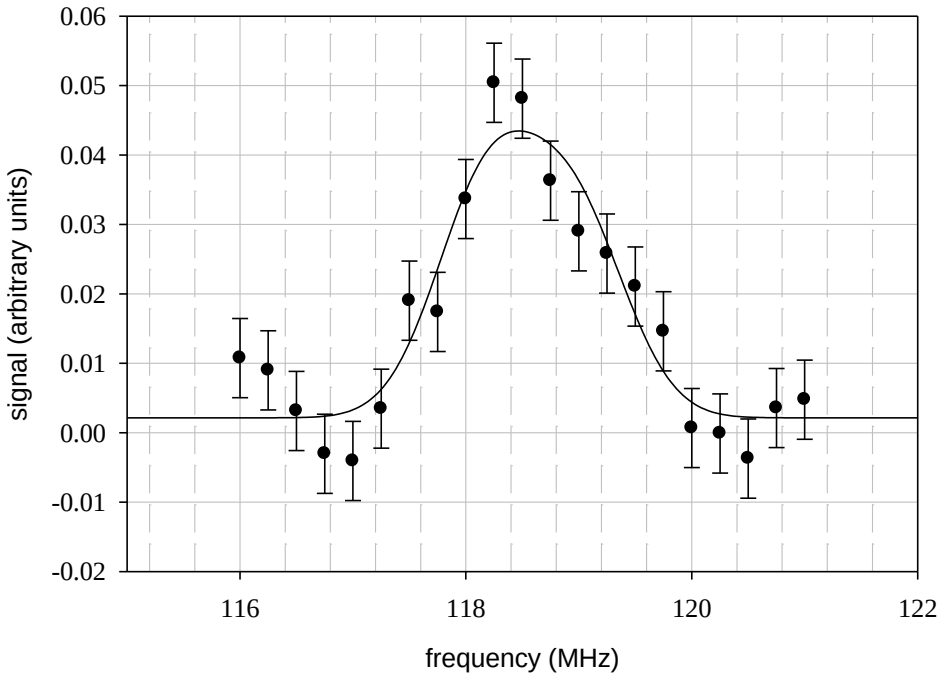

Figure C.4: Ni $9I_{6.5}$ to $9K_{7.5}$ co-propagating. SW06_015

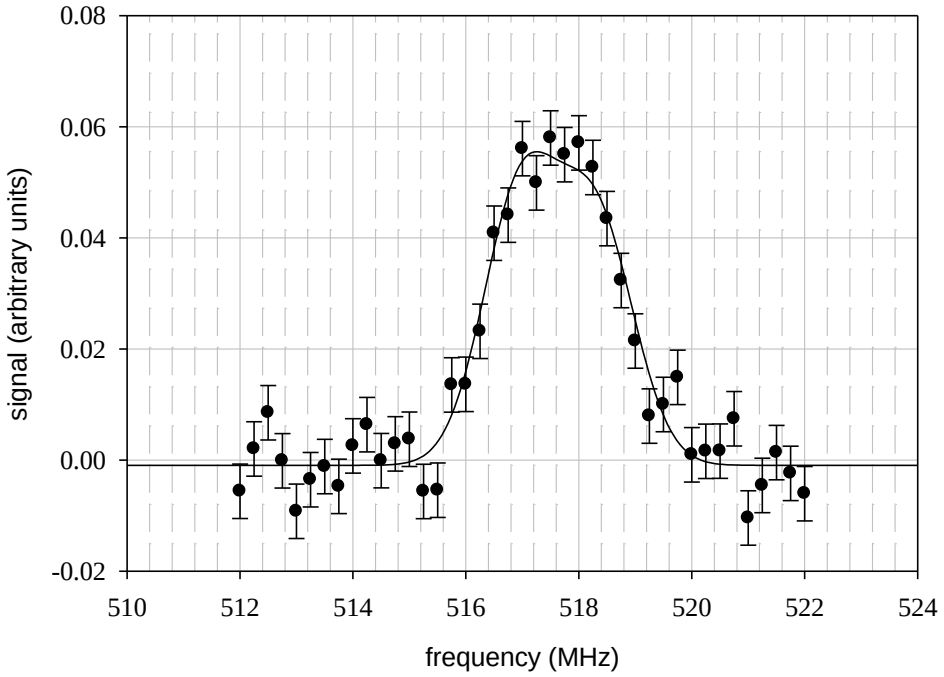

Figure C.5: Ni $9I_{7.5}$ to $9K_{8.5}$ co-propagating. SW06_097

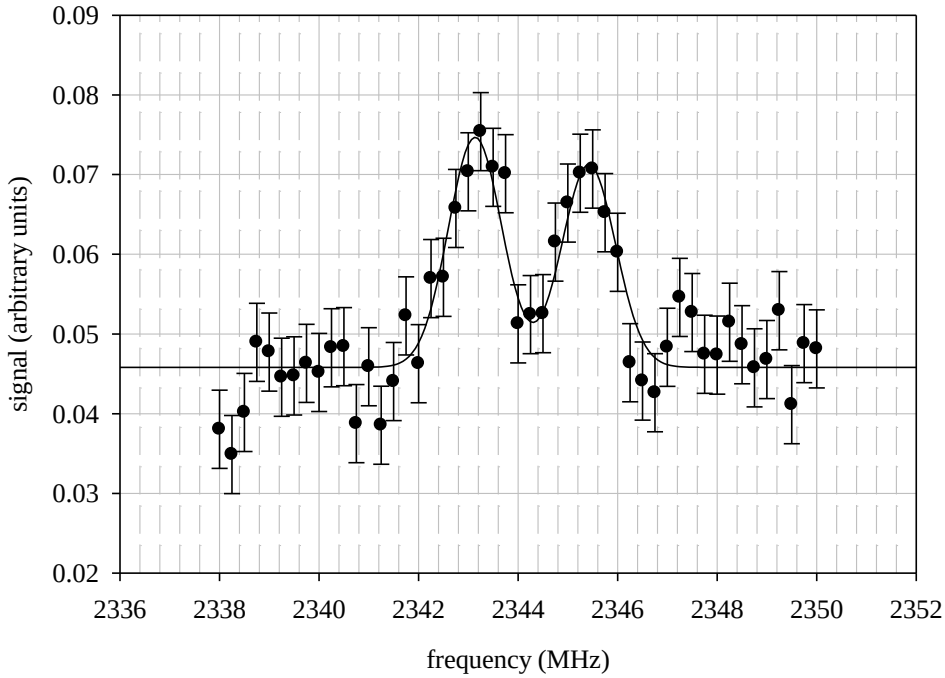

Figure C.6: Ni $9I_{7.5}$ to $9K_{7.5}$ counter-propagating. SW06_095

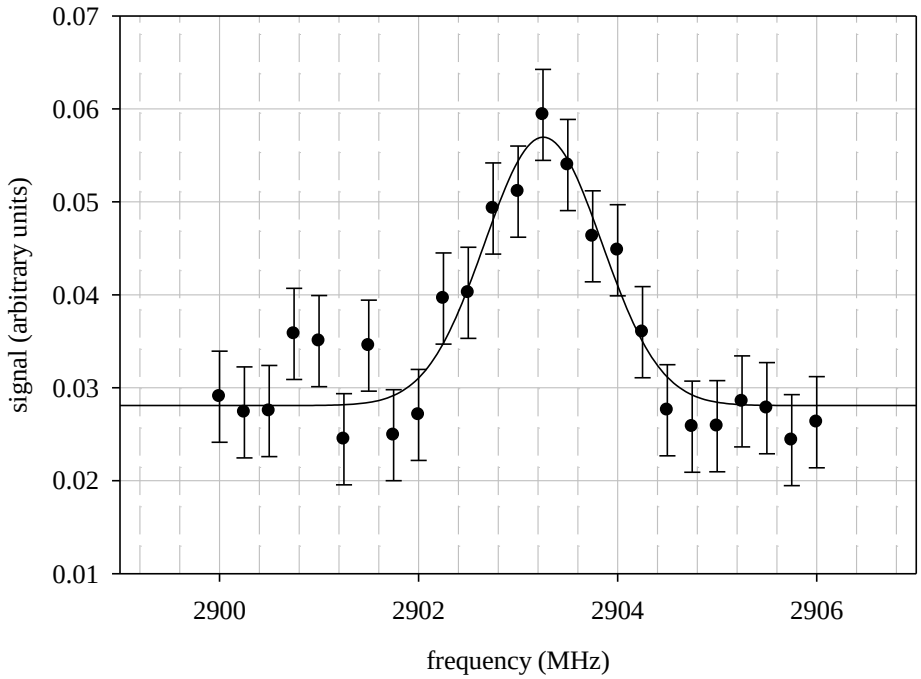

Figure C.7: Ni $9K_{4.5}$ to $9L_{5.5}$ co-propagating. SW06_044

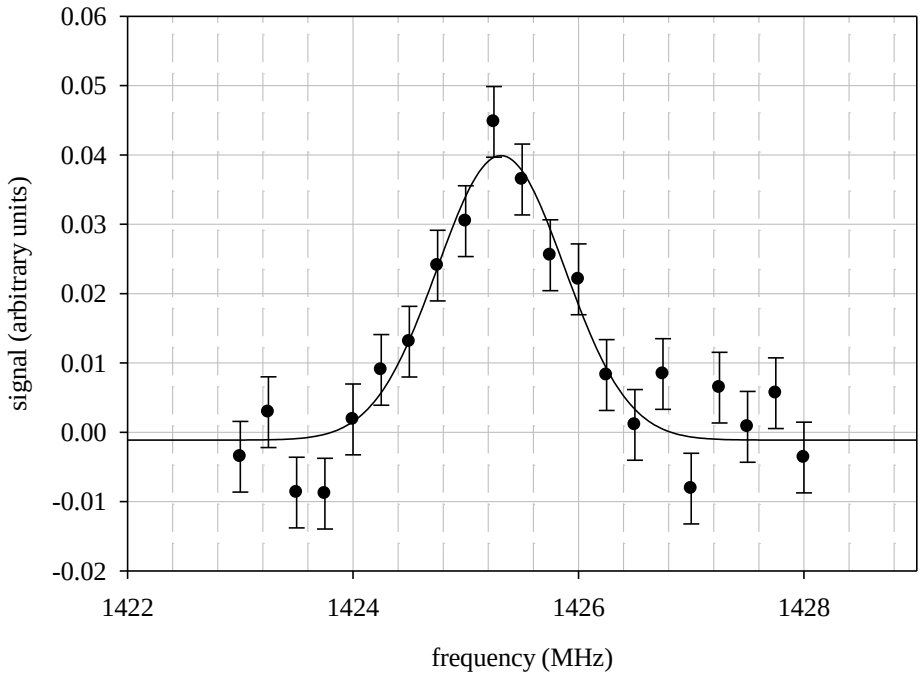

Figure C.8: Ni $9K_{5.5}$ to $9L_{6.5}$ co-propagating. SW06_042

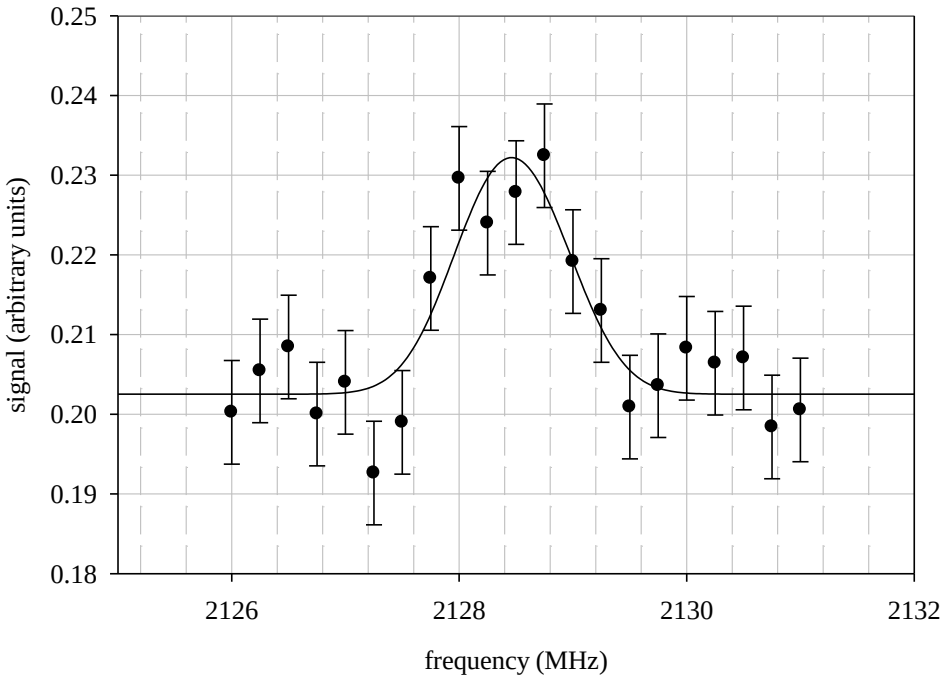

Figure C.9: Ni $9K_{5.5}$ to $9L_{5.5}$ co-propagating. SW04_066

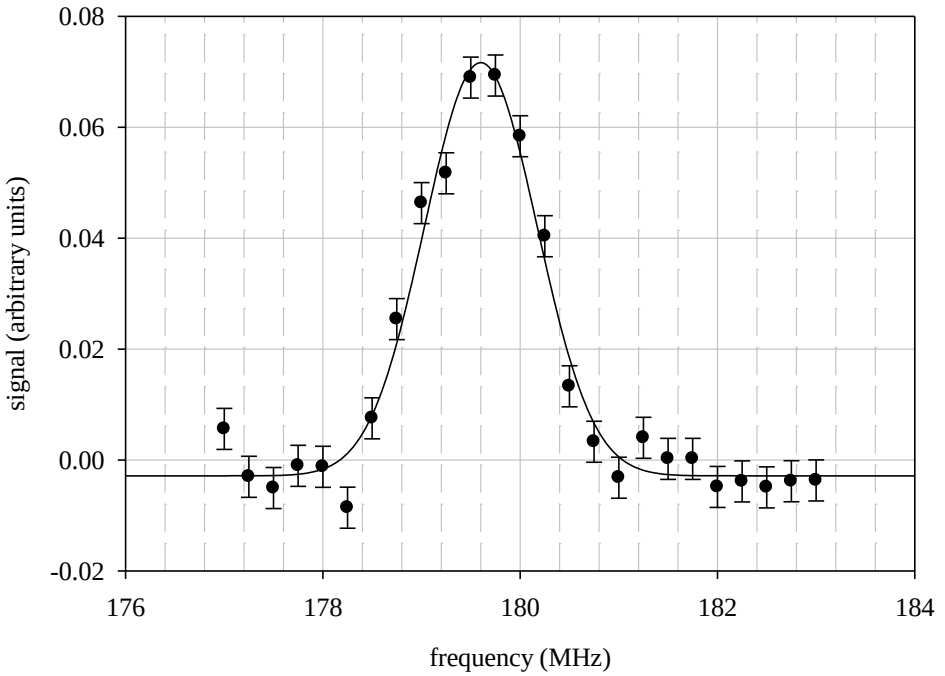

Figure C.10: Ni $9K_{6.5}$ to $9L_{7.5}$ counter-propagating. SW06_022

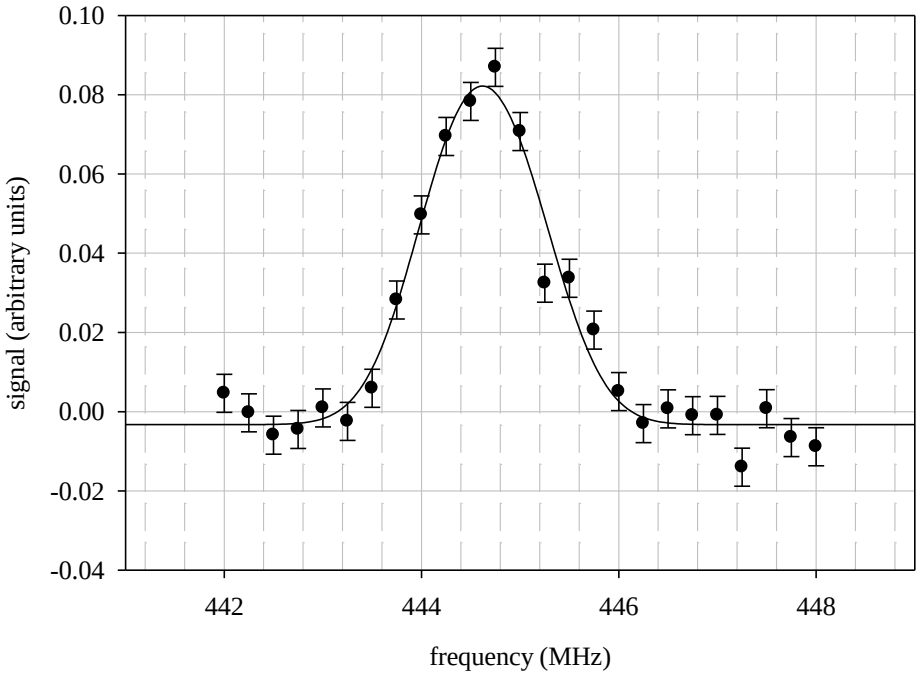

Figure C.11: Ni $9K_{7.5}$ to $9L_{8.5}$ co-propagating. SW06_016

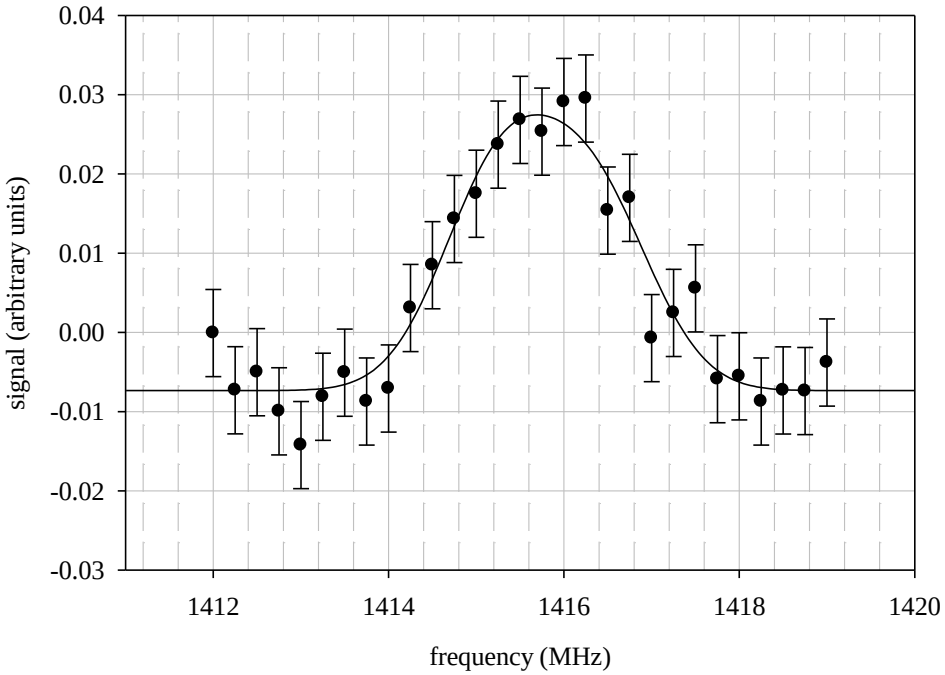

Figure C.12: Ni $9K_{7.5}$ to $9L_{7.5}$ counter-propagating. SW06_018

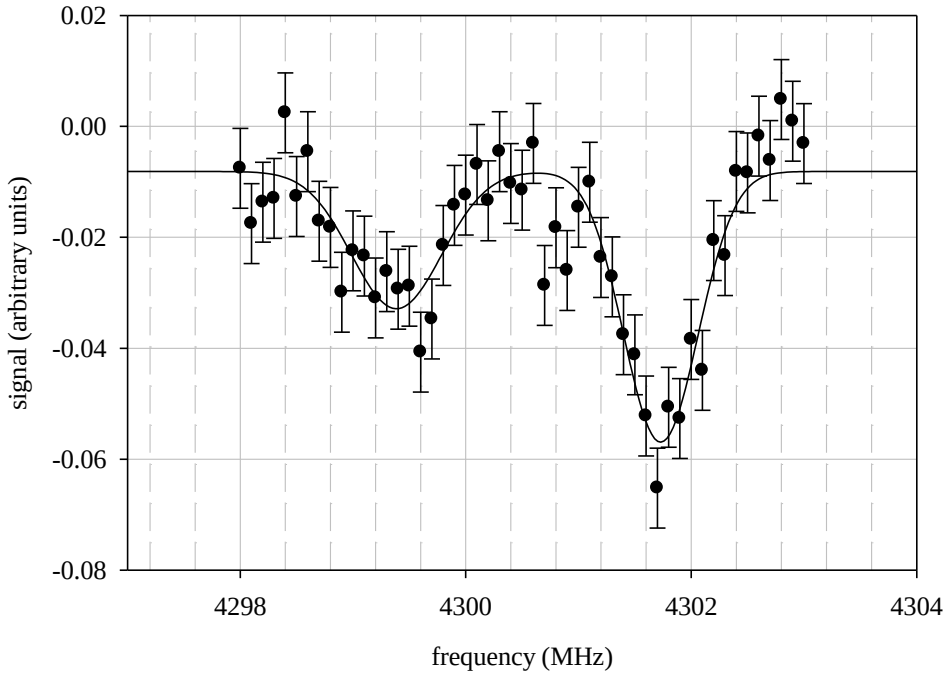

Figure C.13: Ni $9I_{3.5}$ to $9L_{5.5}$ co-propagating. SW06_108

Note that the signals are negative because LIR I and LIR II were set to excite different transitions ($9I_{3.5}$-$20K_{4.5}$ and $9L_{5.5}$-$20M_{6.5}$, respectively). When the RF region is on resonance, this results in less population in the $9L_{5.5}$ state and thus less population for LIR II to excite up to $n' = 20$. The peak on the left appears to be consistent with a resonance that is not Doppler-shifted, which may be due to high reflection coefficients and indicate an upper operating frequency limit for this RF region.

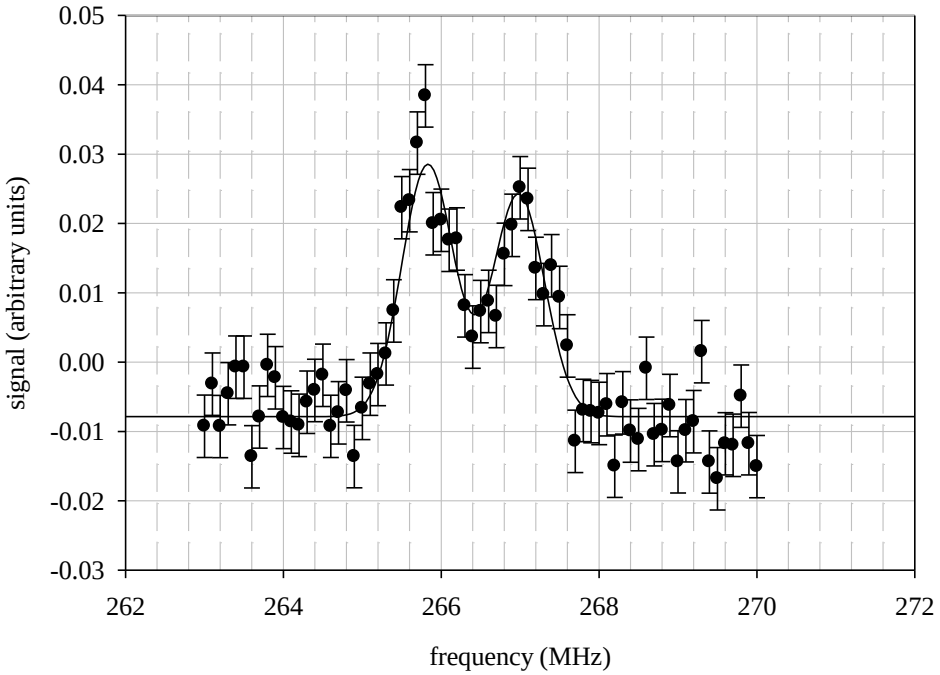

Figure C.14: Ni $9I_{7.5}$ to $9L_{9.5}$ co-propagating. SW06_093